Nanowires

4. Nanowires

This chapter provides an overview of recent research on inorganic nanowires, particularly metallic and semiconducting nanowires. Nanowires are one-dimensional, anisotropic structures, small in diameter, and large in surface-to-volume ratio. Thus, their physical properties are different than those of structures of different scale and dimensionality. While the study of nanowires is particularly challenging, scientists have made immense progress in both developing synthetic methodologies for the fabrication of nanowires, and developing instrumentation for their characterization. The chapter is divided into three main sections: Sect. 4.1 the synthesis, Sect. 4.2 the characterization and physical properties, and Sect. 4.3 the applications of nanowires. Yet, the reader will discover many links that make these aspects of nano-science intimately inter-depent.

Part A | 4

Nanowires are attracting much interest from those seeking to apply nanotechnology and (especially) those investigating nanoscience. Nanowires, unlike other low-dimensional systems, have two quantum-confined directions but one unconfined direction available for electrical conduction. This allows nanowires to be used in applications where electrical conduction, rather than tunneling transport, is required. Because of their unique density of electronic states, in the limit of small diameters nanowires are expected to exhibit significantly different optical, electrical and magnetic properties to their bulk 3-D crystalline counterparts. Increased surface area, very high density of electronic states and joint density of states near the energies of their van Hove singularities, enhanced exciton binding energy, diameter-dependent bandgap, and increased surface scattering for electrons and phonons are just some of the ways in which nanowires differ from their corresponding bulk materials. Yet the sizes of nanowires are typically large enough (> 1 nm in the quantum-confined direction) to result in local crystal structures that are closely related to their parent materials, allowing theoretical predictions about their properties to be made based on knowledge of their bulk properties.

Not only do nanowires exhibit many properties that are similar to, and others that are distinctly different from, those of their bulk counterparts, nanowires also have the advantage from an applications standpoint in that some of the materials parameters critical for certain properties can be independently controlled in nanowires but not in their bulk counterparts. Certain properties can also be enhanced nonlinearly in small-diameter nanowires, by exploiting the singular aspects of the 1-D electronic density of states.

Furthermore, nanowires have been shown to provide a promising framework for applying the "bottom-up" approach [4.1] to the design of nanostructures for nanoscience investigations and for potential nanotechnology applications.

Table 4.1 Selected syntheses of nanowires by material

Material	Growth Technique	Reference	Material	Growth Technique	Reference
ABO_4-type	template$^\alpha$	[4.2]	Ge	high-T, high-P liquid-phase, redox	[4.33]
Ag	DNA-template, redox	[4.3]		VLS$^\delta$	[4.34]
	template, pulsed ECD$^\beta$	[4.4]		oxide-assisted	[4.35]
Au	template, ECD$^\beta$	[4.5, 6]	InAs	VLS$^\delta$	[4.36]
Bi	stress-induced	[4.7]	MgO	VLS$^\delta$	[4.37]
	template, vapor-phase	[4.8]	Mo	step decoration, ECD$^\beta$+ redox	[4.38]
	template, ECD$^\beta$	[4.9–11]	Ni	template, ECD$^\beta$	[4.11, 39, 40]
	template, pressure-injection	[4.12–14]	Pb	liquid-phase$^\mu$	[4.41]
BiSb	pulsed ECD$^\beta$	[4.15]	PbSe	liquid phase	[4.42]
Bi_2Te_3	template, dc ECD$^\beta$	[4.16]		self assembly of nanocrystals$^\nu$	[4.43]
CdS	liquid-phase (surfactant), recrystallization	[4.17]	Pd	step decoration, ECD$^\beta$	[4.44]
	template, ac ECD$^\beta$	[4.18, 19]	Se	liquid-phase, recrystallization	[4.45]
CdSe	liquid-phase (surfactant), redox	[4.20]		template, pressure injection	[4.46]
	template, ac ECD$^\beta$	[4.21, 22]	Si	VLS$^\delta$	[4.47]
Cu	vapor deposition	[4.23]		laser-ablation VLS$^\delta$	[4.48]
	template, ECD$^\beta$	[4.24]		oxide-assisted	[4.49]
Fe	template, ECD$^\gamma$	[4.25, 26]		low-T VLS$^\delta$	[4.50]
	shadow deposition	[4.27]	W	vapor transport	[4.51]
GaN	template, CVD$^\gamma$	[4.28, 29]	Zn	template, vapor-phase	[4.52]
	VLS$^\delta$	[4.30, 31]		template, ECD$^\beta$	[4.53]
GaAs	template, liquid/vapor OMCVD$^\epsilon$	[4.32]	ZnO	VLS$^\delta$	[4.54]
				template, ECD$^\beta$	[4.53, 55]

$^\alpha$ Template synthesis
$^\beta$ Electrochemical deposition (ECD)
$^\gamma$ Chemical vapor deposition (CVD)
$^\delta$ Vapor-liquid-solid (VLS) growth
$^\epsilon$ Organometallic chemical vapor deposition (OMCVD)
$^\mu$ Liquid phase synthesis
$^\nu$ Self assembly of nanocrystals (in liquid phase)

Driven by (1) these new research and development opportunities, (2) the smaller and smaller length scales now being used in the semiconductor, optoelectronics and magnetics industries, and (3) the dramatic development of the biotechnology industry where the action is also at the nanoscale, the nanowire research field has developed with exceptional speed in the last few years. Therefore, a review of the current status of nanowire research is of significant broad interest at the present time. It is the aim of this review to focus on nanowire properties that differ from those of their parent crys-

talline bulk materials, with an eye toward possible applications that might emerge from the unique properties of nanowires and from future discoveries in this field.

For quick reference, examples of typical nanowires that have been synthesized and studied are listed in Table 4.1. Also of use to the reader are review articles that focus on a comparison between nanowire and nanotube properties [4.56] and the many reviews that have been written about carbon nanotubes [4.57–59], which can be considered as a model one-dimensional system.

4.1 Synthesis

In this section we survey the most common synthetic approaches that have successfully afforded high-quality nanowires of a large variety of materials (see Table 4.1). In Sect. 4.1.1, we discuss methods which make use of various templates with nanochannels to confine the nanowire growth in two dimensions. In Sect. 4.1.2, we present the synthesis of nanowires by the vapor-liquid-solid mechanism and its many variations. In Sect. 4.1.3, examples of other synthetic methods of general applicability are presented. The last part of this section (Sect. 4.1.4) features several approaches that have been developed to organize nanowires into simple architectures.

4.1.1 Template–Assisted Synthesis

The template-assisted synthesis of nanowires is a conceptually simple and intuitive way to fabricate nanostructures [4.62–64]. These templates contain very small cylindrical pores or voids within the host material, and the empty spaces are filled with the chosen material, which adopts the pore morphology, to form nanowires. In this section, we describe the templates first, and then describe strategies for filling the templates to make nanowires.

Template Synthesis

In template-assisted synthesis of nanostructures, the chemical stability and mechanical properties of the template, as well as the diameter, uniformity and density of the pores are important characteristics to consider. Templates frequently used for nanowire synthesis include anodic alumina (Al_2O_3), nanochannel glass, ion track-etched polymers and mica films.

Porous anodic alumina templates are produced by anodizing pure Al films in selected acids [4.65–67]. Under carefully chosen anodization conditions, the resulting oxide film possesses a regular hexagonal array of parallel and nearly cylindrical channels, as shown in Fig. 4.1a. The self-organization of the pore structure in an anodic alumina template involves two coupled processes: pore formation with uniform diameters and pore ordering. The pores form with uniform diameters because of a delicate balance between electric field-enhanced diffusion which determines the growth rate of the alumina, and dissolution of the alumina into the acidic electrolyte [4.68]. The pores are believed to self-order because of mechanical stress at the aluminium-alumina interface due to expansion during the anodization. This stress produces a repulsive force between the pores, causing them to arrange in a hexagonal lattice [4.69]. Depending on the anodization conditions, the pore diameter can be systematically varied from ≤ 10 nm up to 200 nm with a pore density in the range of $10^9 – 10^{11}$ pores/cm^2 [4.13, 25, 65, 66]. It has been shown by many groups that the pore size distribution and the pore ordering of the anodic alumina templates can be significantly improved by a two-step anodization technique [4.60, 70, 71], where the aluminium oxide layer is dissolved after the first anodization in an acidic solution followed by a second anodization under the same conditions.

Another type of porous template commonly used for nanowire synthesis is the template type fabricated by chemically etching particle tracks originating from ion bombardment [4.72], such as track-etched polycarbonate membranes (Fig. 4.1b) [4.73, 74], and also mica films [4.39].

Other porous materials can be used as host templates for nanowire growth, as discussed by *Ozin* [4.62]. Nanochannel glass (NCG), for example, contains a regular hexagonal array of capillaries similar to the pore structure in anodic alumina with a packing density as high as 3×10^{10} pores/cm^2 [4.63]. Porous Vycor glass that contains an interconnected network of pores less than 10 nm was also employed for the early
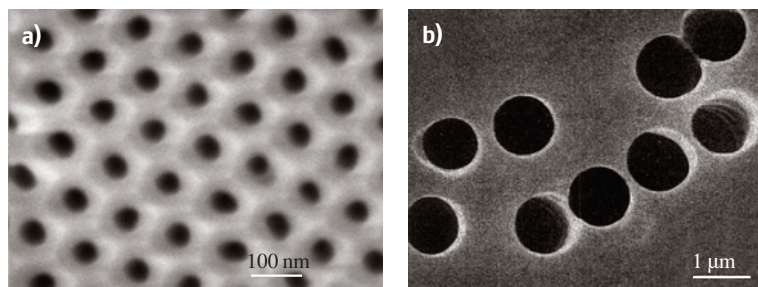
Fig. 4.1 (a) SEM images of the top surfaces of porous anodic alumina templates anodized with an average pore diameter of 44 nm [4.60]. **(b)** SEM image of the particle track-etched polycarbonate membrane, with a pore diameter of 1 μm [4.61]

study of nanostructures [4.75]. Mesoporous molecular sieves [4.76], termed MCM-41, possess hexagonally-packed pores with very small channel diameters which can be varied between 2 nm and 10 nm. Conducting organic filaments have been fabricated in the nanochannels of MCM-41 [4.77]. Recently, the DNA molecule has also been used as a template for growing nanometer-sized wires [4.3].

Diblock copolymers, polymers that consist of two chain segments different properties, have also been utilized as templates for nanowire growth. When two components are immiscible in each other, phase segregation occurs, and depending on their volume ratio, spheres, cylinders and lamellae may self-assemble. To form self-assembled arrays of nanopores, copolymers composed of polystyrene and polymethylmethacrylate $[P(S-b-MMA)]$ [4.79] were used. By applying an electric field while the copolymer was heated above the glass transition temperature of the two constituent polymers, the self-assembled cylinders of PMMA could be

Fig. 4.2a–c XRD patterns of bismuth/anodic alumina nanocomposites with average bismuth wire diameters of **(a)** 40 nm, **(b)** 52 nm, and **(c)** 95 nm [4.78]. The Miller indices corresponding to the lattice planes of bulk Bi are indicated above the individual peaks. The majority of the Bi nanowires are oriented along the [10$\bar{1}$1] and [01$\bar{1}$2] directions for $d_W \geq 60$ nm and $d_W \leq 50$ nm, respectively [4.13, 78]. The existence of more than one dominant orientation in the 52 nm Bi nanowires is attributed to the transitional behavior of *intermediate*-diameter nanowires as the preferential growth orientation is shifted from [10$\bar{1}$1] to [01$\bar{1}$2] with decreasing d_W

aligned with their main axis perpendicular to the film. Selective removal of the PMMA component afforded the preparation of 14 nm-diameter ordered pore arrays with a packing density of 1.9×10^{11} cm^{-3}.

Nanowire Template–Assisted Growth by Pressure Injection

The pressure injection technique is often employed for fabricating highly crystalline nanowires from a low-melting point material and when using porous templates with robust mechanical strength. In the high-pressure injection method, the nanowires are formed by pressure-injecting the desired material in liquid form into the evacuated pores of the template. Due to the heating and pressurization processes, the templates used for the pressure injection method must be chemically stable and be able to maintain their structural integrity at high temperatures and at high pressures. Anodic aluminium oxide films and nanochannel glass are two typical materials used as templates in conjunction with the pressure injection filling technique. Metal nanowires (Bi, In, Sn, and Al) and semiconductor nanowires (Se, Te, GaSb, and Bi$_2$Te$_3$) have been fabricated in anodic aluminium oxide templates using this method [4.12, 46, 78].

The pressure P required to overcome the surface tension for the liquid material to fill the pores with a diameter d_W is determined by the Washburn equation [4.80]:

$$d_W = -4\gamma \cos\theta / P \tag{4.1}$$

where γ is the surface tension of the liquid, and θ is the contact angle between the liquid and the template. To reduce the required pressure and to maximize the filling factor, some surfactants are used to decrease the surface tension and the contact angle. For example, the introduction of Cu into the Bi melt can facilitate filling the pores in the anodic alumina template with liquid Bi and can increase the number of nanowires that are formed [4.13]. However, some of the surfactants might cause contamination problems and should therefore be avoided. Nanowires produced by the pressure injection technique usually possess high crystallinity and a preferred crystal orientation along the wire axis. For example, Fig. 4.2 shows the X-ray diffraction (XRD) patterns of Bi nanowire arrays of three different wire diameters with an injection pressure of ≈ 5000 psi [4.78], showing that the major (> 80%) crystal orientation of the wire axes in the 95 nm and 40 nm diameter Bi nanowire arrays are, respectively, normal to the (202) and (012) lattice planes, which are
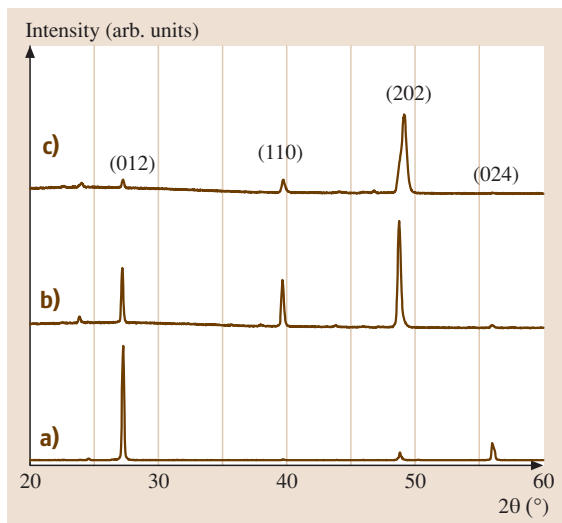
denoted by $[10\bar{1}1]$ and $[01\bar{1}2]$ when using a hexagonal unit cell, suggesting a wire diameter-dependent crystal growth direction. On the other hand, 30 nm Bi nanowires produced using a much higher pressure of $> 20\,000$ psi show a different crystal orientation of (001) along the wire axis [4.14], indicating that the preferred crystal orientation may also depend on the applied pressure, with the most dense packing direction along the wire axis for the highest applied pressure.

Electrochemical Deposition

The electrochemical deposition technique has attracted increasing attention as a versatile method for fabricating nanowires in templates. Traditionally, electrochemistry has been used to grow thin films on conducting surfaces. Since electrochemical growth is usually controllable in the direction normal to the substrate surface, this method can be readily extended to fabricate 1-D or 0-D nanostructures, if the deposition is confined within the pores of an appropriate template. In the electrochemical methods, a thin conducting metal film is first coated on one side of the porous membrane to serve as the cathode for electroplating. The length of the deposited nanowires can be controlled by varying the duration of the electroplating process. This method has been used to synthesize a wide variety of nanowires, such as metals (Bi [4.9, 74]; Co [4.81, 82]; Fe [4.25, 83]; Cu [4.73, 84]; Ni [4.39, 81]; Ag [4.85]; Au [4.5]); conducting polymers [4.9, 61]; superconductors (Pb [4.86]); semiconductors (CdS [4.19]); and even superlattice nanowires with A/B constituents (such as Cu/Co [4.73, 84]) have been synthesized electrochemically (see Table 4.1).

In the electrochemical deposition process, the chosen template has to be chemically stable in the electrolyte during the electrolysis process. Cracks and defects in the templates are detrimental to the nanowire growth, since the deposition processes primarily occur in the more accessible cracks, leaving most of the nanopores unfilled. Particle track-etched mica films or polymer membranes are typical templates used in simple dc electrolysis. To use anodic aluminium oxide films in the dc electrochemical deposition, the insulating barrier layer which separates the pores from the bottom aluminium substrate has to be removed, and a metal film is then evaporated onto the back of the template membrane [4.87]. Compound nanowire arrays, such as Bi_2Te_3, have been fabricated in alumina templates with a high filling factor using the dc electrochemical deposition [4.16]. Figures 4.3a and b, respectively, show the top view and the axial cross-sectional SEM images of a Bi_2Te_3 nanowire array [4.16]. The light areas are associated with Bi_2Te_3 nanowires, the dark regions denote empty pores, and the surrounding gray matrix is alumina.

Surfactants are also used with electrochemical deposition when necessary. For example, when using templates derived from PMMA/PS diblock copolymers, a methanol surfactant is used to facilitate pore filling [4.79], thereby achieving a $\approx 100\%$ filling factor.

It is also possible to employ an ac electrodeposition method in anodic alumina templates without the removal of the barrier layer, by utilizing the rectifying properties of the oxide barrier. In ac electrochemical deposition, although the applied voltage is sinusoidal and symmetric, the current is greater during the cathodic half-cycles, making deposition dominant over the stripping, which occurs in the subsequent anodic half-cycles. Since no rectification occurs at defect sites, the deposition and stripping rates are equal, and no material is deposited. Hence, the difficulties associated with cracks are avoided. In this fashion, metals, such as Co [4.82] and Fe [4.25, 83], and semiconductors, such as CdS [4.19], have been deposited into the pores of anodic aluminium oxide templates without removing the barrier layer.
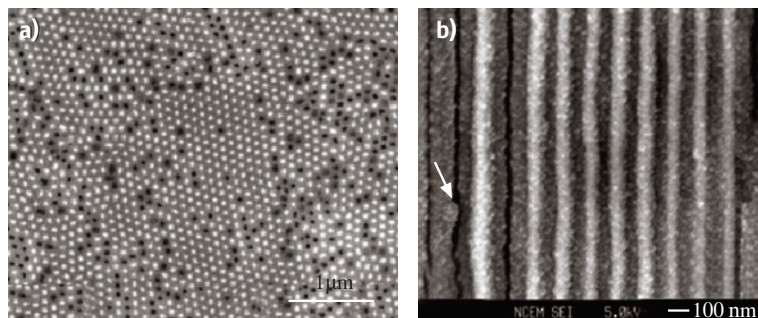

NCEM SEI   5.0kV   —— 100 nm

Fig. 4.3 (a) SEM image of a Bi_2Te_3 nanowire array in cross-section showing a relatively high pore filling factor. **(b)** SEM image of a Bi_2Te_3 nanowire array composite along the wire axis [4.16]
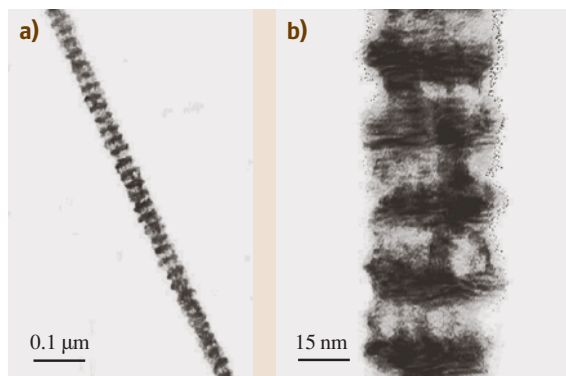
Fig. 4.4 (a) TEM image of a single Co(10 nm)/Cu(10 nm) multilayered nanowire. **(b)** A selected region of the sample at high magnification [4.84]

In contrast to nanowires synthesized by the pressure injection method, nanowires fabricated by the electrochemical process are usually polycrystalline, with no preferred crystal orientations, as observed by XRD studies. However, some exceptions exist. For example, polycrystalline CdS nanowires, fabricated by an ac electrodeposition method in anodic alumina templates [4.19], possibly have a preferred wire growth orientation along the c-axis. In addition, *Xu* et al. have prepared a number of single-crystal II–VI semiconductor nanowires, including CdS, CdSe and CdTe, by dc electrochemical deposition in anodic alumina templates with a nonaqueous electrolyte [4.18, 22]. Furthermore, single-crystal Pb nanowires were formed by pulse electrodeposition under overpotential conditions, but no specific crystal orientation along the wire axis was observed [4.86]. The use of pulse currents is believed to be advantageous for the growth of crystalline wires because the metal ions in the solution can be regenerated between the electrical pulses and therefore uniform deposition conditions can be produced for each deposition pulse. Similarly, single-crystal Ag nanowires were fabricated by pulsed electrodeposition [4.4].

One advantage of the electrochemical deposition technique is the possibility of fabricating multilayered structures within nanowires. By varying the cathodic potentials in the electrolyte, which contains two different kinds of ions, different metal layers can be controllably deposited. Co/Cu multilayered nanowires have been synthesized in this way [4.73, 84]. Figure 4.4 shows TEM images of a single Co/Cu nanowire which is about 40 nm in diameter [4.84]. The light bands represent Co-rich regions and the dark bands represent Cu-rich layers. This electrodeposition method provides a low-cost approach to preparing multilayered 1-D nanostructures.

Vapor Deposition

Vapor deposition of nanowires includes physical vapor deposition (PVD) [4.8], chemical vapor deposition (CVD) [4.29], and metallo-organic chemical vapor deposition (MOCVD) [4.32]. Like electrochemical deposition, vapor deposition is usually capable of preparing smaller-diameter (≤ 20 nm) nanowires than pressure injection methods, since it does not rely on the high pressure and the surface tension involved to insert the material into the pores.

In the physical vapor deposition technique, the material to be filled is first heated to produce a vapor, which is then introduced through the pores of the template and cooled to solidify. Using a specially designed experimental set-up [4.8], nearly single-crystal Bi nanowires in anodic aluminium templates with pore diameters as small as 7 nm have been synthesized, and these Bi nanowires were found to possess a preferred crystal growth orientation along the wire axis, similar to the Bi nanowires prepared by pressure injection [4.8, 13].

Compound materials that result from two reacting gases have also be prepared by the chemical vapor deposition (CVD) technique. For example, single-crystal GaN nanowires have been synthesized in anodic alumina templates through a gas reaction of Ga_2O vapor with a flowing ammonia atmosphere [4.28, 29]. A different liquid/gas phase approach has been used to prepare polycrystalline GaAs and InAs nanowires in a nanochannel glass array [4.32]. In this method, the nanochannels are filled with one liquid precursor (such as Me_3Ga or Et_3In) via a capillary effect and the nanowires are formed within the template by reactions between the liquid precursor and the other gas reactant (such as AsH_3).

4.1.2 VLS Method for Nanowire Synthesis

Some of the recent successful syntheses of semiconductor nanowires are based on the so-called vapor-liquid-solid (VLS) mechanism of anisotropic crystal growth. This mechanism was first proposed for the growth of single crystal silicon whiskers 100 nm to hundreds of microns in diameter [4.88]. The proposed growth mechanism (see Fig. 4.5) involves the absorption of source material from the gas phase into a liquid droplet of catalyst (a molten particle of gold on a silicon substrate in the original work [4.88]). Upon supersaturation of the liquid alloy, a nucleation event generates a solid precipitate of the source material. This seed serves as

a preferred site for further deposition of material at the interface of the liquid droplet, promoting the elongation of the seed into a nanowire or a whisker, and suppressing further nucleation events on the same catalyst. Since the liquid droplet catalyzes the incorporation of material from the gas source to the growing crystal, the deposit grows anisotropically as a whisker whose diameter is dictated by the diameter of the liquid alloy droplet. The nanowires thus obtained are of high purity, except for the end containing the solidified catalyst as an alloy particle (see Figs. 4.5 and 4.6a). Real-time observations of the alloying, nucleation, and elongation steps in the growth of germanium nanowires from gold nanoclusters by the VLS method were recorded by in situ TEM [4.89].

Reduction of the average wire diameter to the nanometer scale requires the generation of nanosized catalyst droplets. However, due to the balance between the liquid-vapor surface free energy and the free energy of condensation, the size of a liquid droplet, in equilibrium with its vapor, is usually limited to the micrometer range. This obstacle has been overcome in recent years by several new methodologies. (1) Advances in the synthesis of metal nanoclusters have made monodispersed nanoparticles commercially available. These can be dispersed on a solid substrate in high dilution so that when the temperature is raised above the melting point, the liquid clusters do not aggregate [4.47]. (2) Alternatively, metal islands of nanoscale sizes can self-form when a strained thin layer is grown or heat-treated on a non-epitaxial substrate [4.34]. (3) Laser-assisted catalytic VLS growth is a method used to generate nanowires under non-equilibrium conditions. Using laser ablation of a target containing both the catalyst and the source materials, a plasma is generated from which catalyst nanoclusters nucleate as the plasma cools down. Single
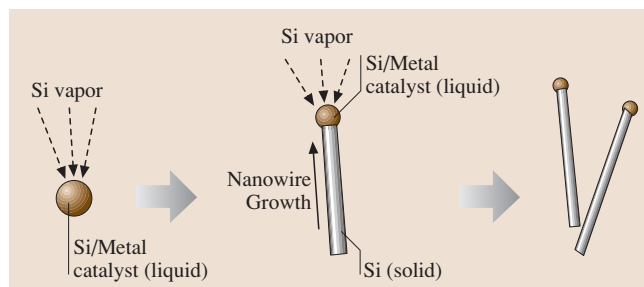

Fig. 4.5 Schematic diagram illustrating the growth of silicon nanowires by the VLS mechanism

crystal nanowires grow as long as the particle remains liquid [4.48]. (4) Interestingly, by optimizing the material properties of the catalyst-nanowire system, conditions can be achieved for which nanocrystals nucleate in a liquid catalyst pool supersaturated with the nanowire material, migrate to the surface due to a large surface tension, and continue growing as nanowires perpendicular to the liquid surface [4.50]. In this case, supersaturated nanodroplets are sustained on the outer end of the nanowire due to the low solubility of the nanowire material in the liquid [4.91].

A wide variety of elemental, binary and compound semiconductor nanowires has been synthesized via the VLS method, and relatively good control over the nanowire diameter and diameter distribution has been achieved. Researchers are currently focusing their attention on the controlled variation of the materials properties along the nanowire axis. In this context, researchers have modified the VLS synthesis apparatus to generate compositionally-modulated nanowires. GaAs/GaP-modulated nanowires have been synthesized by alternately ablating targets of the corresponding ma-
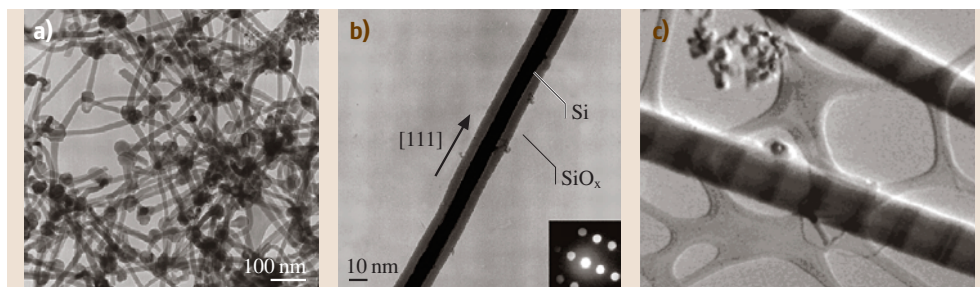

Fig. 4.6 (**a**) TEM images of Si nanowires produced after laser-ablating a $Si_{0.9}Fe_{0.1}$ target. The dark spheres with a slightly larger diameter than the wires are solidified catalyst clusters [4.48]. (**b**) Diffraction contrast TEM image of a Si nanowire. The crystalline Si core appears darker than the amorphous oxide surface layer. The *inset* shows the convergent beam electron diffraction pattern recorded perpendicular to the wire axis, confirming the nanowire crystallinity [4.48]. (**c**) STEM image of $Si/Si_{1-x}Ge_x$ superlattice nanowires in the bright field mode. The scale bar is 500 nm [4.90]

terials in the presence of gold nanoparticles [4.92]. p-Si/n-Si nanowires were grown by chemical vapor deposition from alternating gaseous mixtures containing the appropriate dopant [4.92]. $Si/Si_{1-x}Ge_x$ nanowires were grown by combining silicon from a gaseous source with germanium from a periodically ablated target (see Fig. 4.6c) [4.90]. $NiSi - Si$ nanowires have been successfully synthesized which directly incorporate a nanowire metal contact into active nanowire devices [4.93]. Finally, using an ultrahigh vacuum chamber and molecular beams, InAs/InP nanowires with atomically sharp interfaces were obtained [4.94]. These compositionally-modulated nanowires are expected to exhibit exciting electronic, photonic, and thermoelectric properties.

Interestingly, silicon and germanium nanowires grown by the VLS method consist of a crystalline core coated with a relatively thick amorphous oxide layer $(2-3 nm)$ (see Fig. 4.6b). These layers are too thick to be the result of ambient oxidation, and it has been shown that these oxides play an important role in the nanowire growth process [4.49, 95]. Silicon oxides were found to serve as a special and highly selective catalyst that significantly enhances the yield of Si nanowires without the need for metal catalyst particles [4.49, 95, 96]. A similar yield enhancement was also found in the synthesis of Ge nanowires from the laser ablation of Ge powder mixed with GeO_2 [4.35]. The Si and Ge nanowires produced from these metal-free targets generally grow along the [112] crystal direction [4.97], and have the benefit that no catalyst clusters are found on either ends of the nanowires. Based on these observations and other TEM studies [4.35, 95, 97], an oxide-enhanced nanowire growth mechanism different from the classical VLS mechanism was proposed, where no metal catalyst is required during the laser ablation-assisted synthesis [4.95]. It is postulated that the nanowire growth is dependent on the presence of SiO (or GeO) vapor, which decomposes in the nanowire tip region into both Si (or Ge), which is incorporated into the crystalline phase, and SiO_2 (or GeO_2), which contributes to the outer coating. The initial nucleation events generate oxide-coated spherical nanocrystals. The [112] crystal faces have the fastest growth rate, and therefore the nanocrystals soon begin elongating along this direction to form one-dimensional structures. The Si_mO or Ge_mO (m > 1) layer on the nanowire tips may be in or at temperatures near their molten states, catalyzing the incorporation of gas molecules in a directional fashion [4.97]. Besides nanowires with smooth walls, a second morphology of chains of unoriented
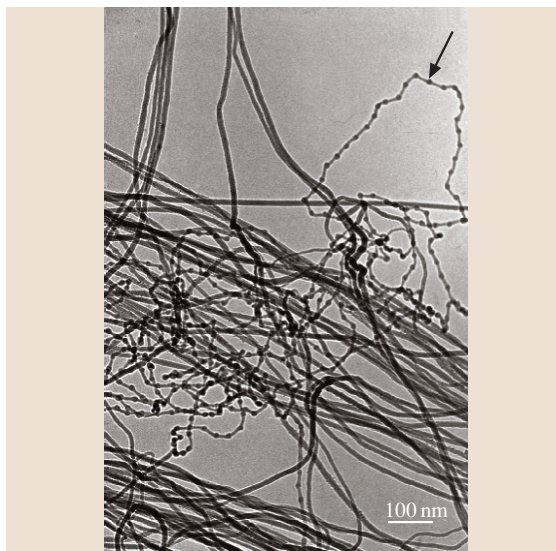

Fig. 4.7 TEM image showing the two major morphologies of Si nanowires prepared by the oxide-assisted growth method [4.95]. Notice the absence of metal particles when compared to Fig. 4.6a. The *arrow* points at an oxide-linked chain of Si nanoparticles

nanocrystals linked by oxide necks is frequently observed (indicated by an arrow in Fig. 4.7). In addition, it was found by STM studies that about 1% of the wires consist of a regular array of two alternating segments, 10 nm and 5 nm in length, respectively [4.98]. The segments, whose junctions form an angle of $30°$, are probably a result of alternating growth along different crystallographic orientations [4.98]. Branched and hyperbranched Si nanowire structures have also been synthesized by *Whang* et al. [4.99].

4.1.3 Other Synthesis Methods

In this section we review several other general procedures available for the synthesis of a variety of nanowires. We focus on "bottom-up" approaches, which afford many kinds of nanowires in large numbers, and do not require highly sophisticated equipment (such as scanning microscopy or lithography-based methods), and exclude cases for which the nanowires are not self-sustained (such as in the case of atomic rows on the surface of crystals).

A solution-phase synthesis of nanowires with controllable diameters has been demonstrated [4.45, 100], without the use of templates, catalysts, or surfactants. Instead, *Gates* et al. make use of the anisotropy of

the crystal structure of trigonal selenium and tellurium, which can be viewed as rows of 1-D helical atomic chains. Their approach is based on the mass transfer of atoms during an aging step from a high free-energy solid phase (e.g., amorphous selenium) to a seed (e.g., trigonal selenium nanocrystal) which grows preferentially along one crystallographic axis. The lateral dimension of the seed, which dictates the diameter of the nanowire, can be controlled by the temperature of the nucleation step. Furthermore, Se/Te alloy nanowires were synthesized by this method, and Ag_2Se compound nanowires were obtained by treating selenium nanowires with $AgNO_3$ [4.101–103]. In a separate work, tellurium nanowires were transformed into Bi_2Te_3 nanowires by their reaction with $BiPh_3$ [4.104].

More often, however, the use of surfactants is necessary to promote the anisotropic 1-D growth of nanocrystals. Solution phase synthetic routes have been optimized to produce monodispersed quantum dots, (zero-dimensional isotropic nanocrystals) [4.106]. Surfactants are necessary in this case to stabilize the interfaces of the nanoparticles and to retard oxidation and aggregation processes. Detailed studies on the effect of growth conditions revealed that they can be manipulated to induce a directional growth of the nanocrystals, usually generating nanorods (aspect ratio of ≈ 10), and in favorable cases, nanowires with high aspect ratios. Heath and LeGoues synthesized germanium nanowires by reducing a mixture of $GeCl_4$ and phenyl-$GeCl_3$ at high temperature and high pressure. The phenyl ligand was essential for the formation of high aspect ratio nanowires [4.33]. In growing CdSe nanorods [4.20], Alivisatos et al. used a mixture of two surfactants, whose concentration ratio influenced the structure of the nanocrystal. It is believed that different surfactants have different affinities, and different absorption rates, for the different crystal faces of CdSe, thereby regulating the growth rates of these faces. In the liquid phase synthesis of Bi nanowires, the additive $NaN(SiMe_3)_2$ induces the growth of nanowires oriented along the [110] crystal direction from small bismuth seed clusters, while water solely retarded the growth along the [001] direction, inducing the growth of hexagonal-plate particles [4.104]. A coordinating alkyl-diamine solvent was used to grow polycrystalline PbSe nanowires at low temperatures [4.42]. Here, the surfactant-induced directional growth is believed to occur through to the formation of organometallic complexes in which the bidentate ligand assumes the equatorial positions, thus hindering the ions from approaching each other in this plane. Additionally, the alkyl-diamine molecules coat the external

surface of the wire, preventing lateral growth. The aspect ratio of the wires increased as the temperature was lowered in the range $10\,°C < T < 117\,°C$. Ethylenediamine was used to grow CdS nanowires and tetrapods by a solvo-thermal recrystallization process starting with CdS nanocrystals or amorphous particles [4.17]. While the coordinating solvent was crucial for the nanowire growth, its role in the shape and phase control was not clarified.

Stress-induced crystalline bismuth nanowires have been grown from sputtered films of layers of Bi and CrN. The nanowires presumably grow from defects and cleavage fractures in the film, and are up to several millimeters in length with diameters ranging from 30 to 200 nm [4.7]. While the exploration of this technique has only begun, stress-induced unidirectional growth should be applicable to a variety of composite films.

Selective electrodeposition along the step edges in highly oriented pyrolytic graphite (HOPG) was used
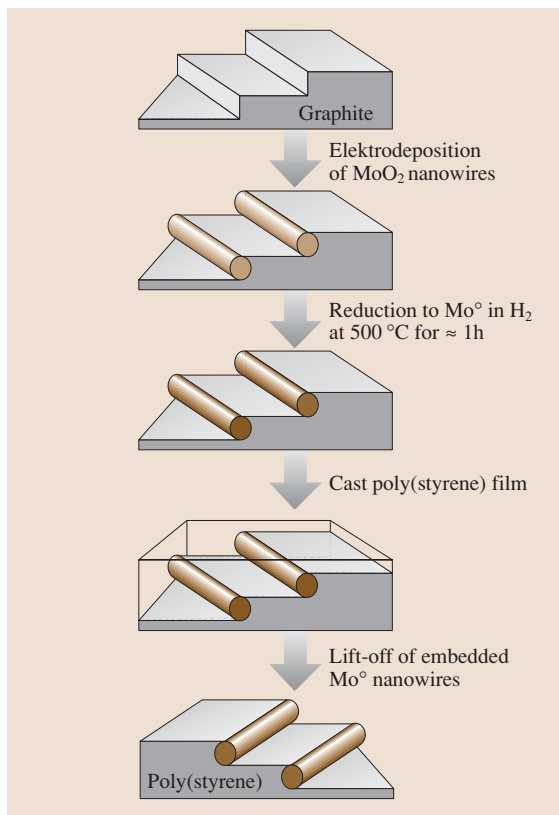

Fig. 4.8 Schematic of the electrodeposition step edge decoration of HOPG (highly oriented pyrolytic graphite) for the synthesis of molybdenum nanowires [4.38, 105]

to obtain MoO_2 nanowires as shown in Fig. 4.8. The site-selectivity was achieved by applying a low overpotential to the electrochemical cell in which the HOPG served as cathode, thus minimizing the nucleation events on less favorable sites (plateaux). While these nanowires cannot be removed from the substrate, they can be reduced to metallic molybdenum nanowires, which can then be released as free-standing nanowires. Other metallic nanowires were also obtained by this method [4.38, 105]. In contrast to the template synthesis approaches described above, in this method the substrate only defines the position and orientation of the nanowire, not its diameter. In this context, other surface morphologies, such as self-assembled grooves in etched crystal planes, have been used to generate nanowire arrays via gas-phase shadow deposition (for example: Fe nanowires on (110)NaCl [4.27]). The cross-section of artificially prepared superlattice structures has also been used for site-selective deposition of parallel and closely spaced nanowires [4.107]. Nanowires prepared on the above-mentioned substrates would have semicircular, rectangular, or other unconventional cross-sectional shapes.

4.1.4 Hierarchical Arrangement and Superstructures of Nanowires

Ordering nanowires into useful structures is another challenge that needs to be addressed in order to harness the full potential of nanowires for applications. We will first review examples of nanowires with nontrivial structures, and then proceed to describe methods used to create assemblies of nanowires of a predetermined structure.

We mentioned in Sect. 4.1.2 that the preparation of nanowires with a graded composition or with a superlattice structure along their main axis was demonstrated by controlling the gas phase chemistry as a function of time during the growth of the nanowires by the VLS method. Control of the composition along the axial dimension was also demonstrated by a template-assisted method, for example by the consecutive electrochemical deposition of different metals in the pores of an alumina template [4.110]. Alternatively, the composition can be varied along the radial dimension of the nanowire, for example by first growing a nanowire by the VLS method and then switching the synthesis conditions to grow a different material on the surface of the nanowire by CVD. This technique was demonstrated for the synthesis of Si/Ge and Ge/Si coaxial (or core-shell) nanowires [4.111], and it was shown that the outer shell can be formed epitaxially on the inner core by a thermal annealing process. *Han* et al. demonstrated the versatility of MgO nanowire arrays grown by the VLS method as templates for the PLD deposition of oxide coatings to yield MgO/YBCO, MgO/LCMO, MgO/PZT and MgO/Fe_3O_4 core/shell nanowires, all exhibiting epitaxial growth of the shell on the MgO core [4.37]. A different approach was adopted by *Wang* et al. who generated a mixture of coaxial and biaxial $SiC - SiO_x$ nanowires by the catalyst-free high-temperature reaction of amorphous silica and a carbon/graphite mixture [4.112].

A different category of nontrivial nanowires is that of nanowires with a nonlinear structure, resulting from multiple one-dimensional growth steps. Members of this category are tetrapods, which were mentioned in the context of the liquid phase synthesis (Sect. 4.1.3). In this process, a tetrahedral quantum dot core is first grown, and then the conditions are modified to induce one-dimensional growth of a nanowire from each one of the facets of the tetrahedron. A similar process produced high-symmetry In_2O_3/ZnO hierarchical nanostructures. From a mixture of heat-treated In_2O_3, ZnO, and graphite powders, faceted In_2O_3 nanowires were first obtained, on which oriented shorter ZnO nanowires were crystallized [4.108]. Brush-like structures were obtained as a mixture of 11 structures of different symmetries. For example, two, four, or six rows of ZnO nanorods could be found on different core nanowires, depending on the
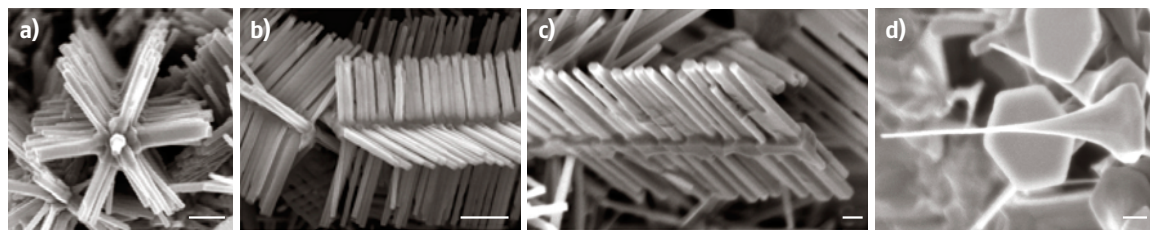

Fig. 4.9a–d SEM images of **(a)** sixfold- **(b)** fourfold- and **(c)** twofold-symmetry nanobrushes made of an In_2O_3 core and ZnO nanowire brushes [4.108], and of **(d)** ZnO nanonails [4.109]
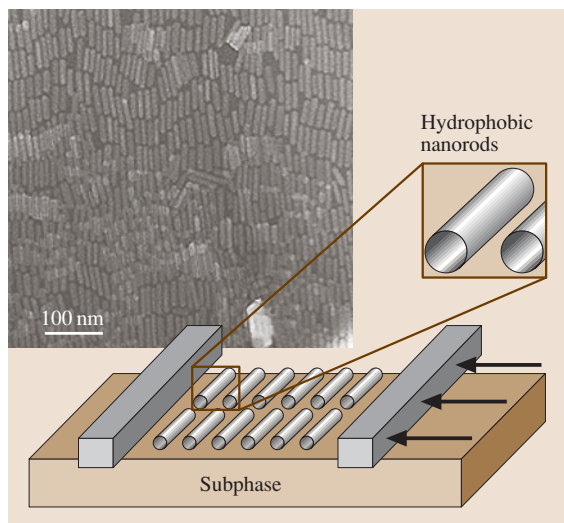
Fig. 4.10 A TEM image of a smectic phase of a BaCrO$_4$ nanorod film (*left inset*) achieved by the Langmuir–Blodgett technique, as depicted by the illustration [4.113]

crystallographic orientation of the main axis of the core nanowire, as shown in Fig. 4.9. Comb-like structures made entirely of ZnO were also reported [4.54].

Controlling the position of a nanowire in the growth process is important for preparing devices or test structures containing nanowires, especially when it involves a large array of nanowires. Post-synthesis methods to align and position nanowires include microfluidic channels [4.114], Langmuir–Blodgett assemblies [4.113], and electric field-assisted assembly [4.115]. The first method involves the orientation of the nanowires by the liquid flow direction when a nanowire solution is injected into a microfluidic channel assembly and by the interaction of the nanowires with the side walls of the channel. The second method involves the alignment of nanowires at a liquid–gas or liquid–liquid interface by the application of compressive forces on the interface (see Fig. 4.10). The aligned nanowire films can then be transferred onto a substrate and lithography methods can be used to define interconnects. This allows the nanowires to be organized with a controlled alignment and spacing over large areas. Using this method, centimeter-scale arrays containing thousands of single silicon nanowire field-effect transistors with high performance could be assembled to make large-scale nanowire circuits and devices [4.99, 116].

The third technique is based on dielectrophoretic forces that pull polarizable nanowires toward regions of high field strength. The nanowires align between two isolated electrodes which are capacitatively coupled to a pair of buried electrodes biased with an AC voltage. Once a nanowire shorts the electrodes, the electric field is eliminated, preventing more nanowires from depositing. The above techniques have been successfully used to prepare electronic circuitry and optical devices out of nanowires (see Sects. 4.3.1 and 4.3.3). Alternatively, alignment and positioning of the nanowires can be specified and controlled during their growth by the proper design of the synthesis method. For example, ZnO nanowires prepared by the VLS method were grown into an array in which both their position on the substrate and their growth direction and orientation were controlled [4.54]. The nanowire growth region was defined by patterning the gold film, which serves as a catalyst for the ZnO nanowire growth, employing soft-lithography, e-beam lithography, or photolithography. The orientation of the nanowires was achieved by selecting a substrate with a lattice structure matching that of the nanowire material to facilitate the epitaxial growth. These conditions result in an array of nanowire posts at predetermined positions, all vertically aligned with the same crystal growth orientation (see Fig. 4.11). Similar rational GaN nanowire arrays have been synthesized epitaxially on $(100) - LiAlO_2$ and (111) MgO single-crystal substrates. In addition, control over the crystallographic growth directions of nanowires was achieved by lattice-matching to different substrates. For example, GaN nanowires on (100) $LiAlO_2$ substrates grow oriented along the [110] direction, whereas (111) MgO substrates result in the growth of GaN nanowires with an [001] orientation, due to the different lattice-matching constraints [4.117]. A similar structure could be obtained by the template-mediated electrochemical synthesis of nanowires (see Sect. 4.1.1), particularly if anodic alumina with its parallel and ordered channels is used. The control over the location of the nucleation of nanowires in the electrochemical deposition is determined by the pore positions and the back-electrode geometry. The pore positions can be precisely controlled by imprint lithography [4.118]. By growing the template on a patterned conductive substrate that serves as a back-electrode [4.119–121] different materials can be deposited in the pores at different regions of the template.

4.2 Characterization and Physical Properties of Nanowires

In this section we review the structure and properties of nanowires and their interrelationship. The discovery and investigation of nanostructures were spurred on by advances in various characterization and microscopy techniques that enabled material characterization to take place at smaller and smaller length scales, reaching length scales down to individual atoms. For applications, characterizing the structural properties of nanowires is especially important, so that a reproducible relationship between their desired functionality and their geometrical and structural characteristics can be established. Due to the enhanced surface-to-volume ratio in nanowires, their properties may depend sensitively on their surface conditions and geometrical configurations. Even nanowires made of the same material may possess dissimilar properties due to differences in their crystal phase, crystalline size, surface conditions, and aspect ratios, which depend on the synthesis methods and conditions used in their preparation.

4.2.1 Structural Characterization

Structural and geometric factors play an important role in determining the various attributes of nanowires, such as their electrical, optical and magnetic properties. Therefore, various novel tools have been developed and employed to obtain this important structural information at the nanoscale. At the micron scale, optical techniques are extensively used for imaging structural features. Since the sizes of nanowires are usually comparable to or, in most cases, much smaller than the wavelength of visible light, traditional optical microscopy techniques are usually limited when characterizing the morphology

and surface features of nanowires. Therefore, electron microscopy techniques play a more dominant role at the nanoscale. Since electrons interact more strongly than photons, electron microscopy is particularly sensitive relative to X-rays for the analysis of tiny samples.

In this section we review and give examples of how scanning electron microscopy, transmission electron microscopy, scanning probe spectroscopies, and diffraction techniques are used to characterize the structures of nanowires. To provide the necessary basis for developing reliable structure–property relations, multiple characterization tools are applied to the same samples.

Scanning Electron Microscopy

SEM usually produces images down to length scales of ≈ 10 nm and provides valuable information regarding the structural arrangement, spatial distribution, wire density, and geometrical features of the nanowires. The examples of SEM micrographs shown in Figs. 4.1 and 4.3 indicate that structural features at the 10 nm to 10 μm length scales can be probed, providing information on the size, size distribution, shapes, spatial distributions, density, nanowire alignment, filling factors, granularity, etc.. As another example, Fig. 4.11a shows an SEM image of ZnO nanowire arrays grown on a sapphire substrate [4.122], which provides evidence for the nonuniform spatial distribution of the nanowires on the substrate, which was attained by patterning the catalyst film to define high-density growth regions and nanowire-free regions. Figure 4.11b, showing a higher magnification of the same system, indicates that these ZnO nanowires grow perpendicular to the substrate, are well-aligned with approximately equal
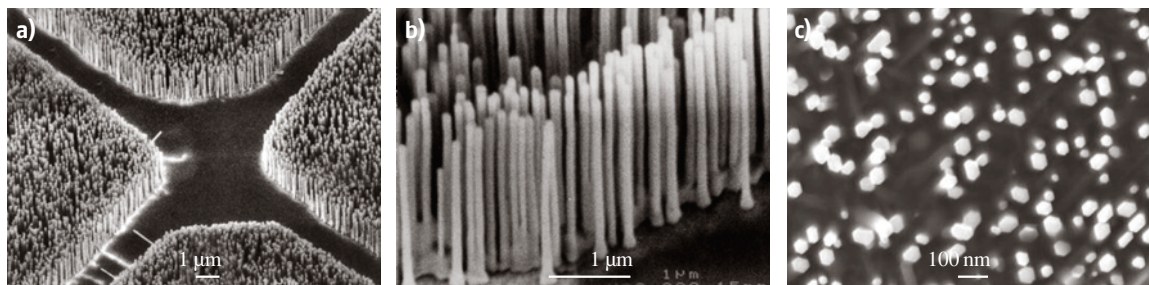

Fig. 4.11a–c SEM images of ZnO nanowire arrays grown on a sapphire substrate, where **(a)** shows patterned growth, **(b)** shows a higher resolution image of the parallel alignment of the nanowires, and **(c)** shows the faceted side-walls and the hexagonal cross-section of the nanowires. For nanowire growth, the sapphire substrates were coated with a 1.0 to 3.5 nm-thick patterned layer of Au as the catalyst, using a TEM grid as the shadow mask. These nanowires have been used for nanowire laser applications [4.122]
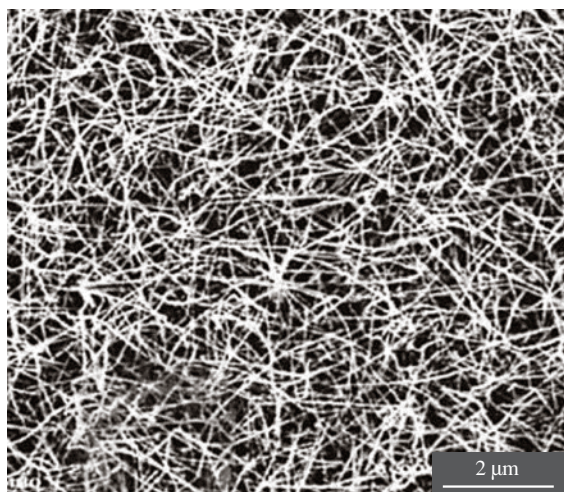
Fig. 4.12 SEM image of GaN nanowires in a mat arrangement synthesized by laser-assisted catalytic growth. The nanowires have diameters and lengths on the order of 10 nm and 10 μm, respectively [4.30]

provides further information about the surface of the nanowires, showing it to be well-faceted, forming a hexagonal cross-section, indicative of nanowire growth along the ⟨0001⟩ direction. Both the uniformity of the nanowire size, their alignment perpendicular to the substrate, and their uniform growth direction, as suggested by the SEM data, are linked to the good epitaxial interface between the (0001) plane of the ZnO nanowire and the (110) plane of the sapphire substrate. (The crystal structures of ZnO and sapphire are essentially incommensurate, with the exception that the *a*-axis of ZnO and the *c*-axis of sapphire are related almost exactly by a factor of 4, with a mismatch of less than 0.08% at room temperature [4.122].) The well-faceted nature of these nanowires has important implications for their lasing action (see Sect. 4.3.2). Figure 4.12 shows an SEM image of GaN nanowires synthesized by a laser-assisted catalytic growth method [4.30], indicating a random spatial orientation of the nanowire axes and a wide diameter distribution for these nanowires, in contrast to the ZnO wires in Fig. 4.11 and to arrays of well-aligned nanowires prepared by template-assisted growth (see Fig. 4.3).
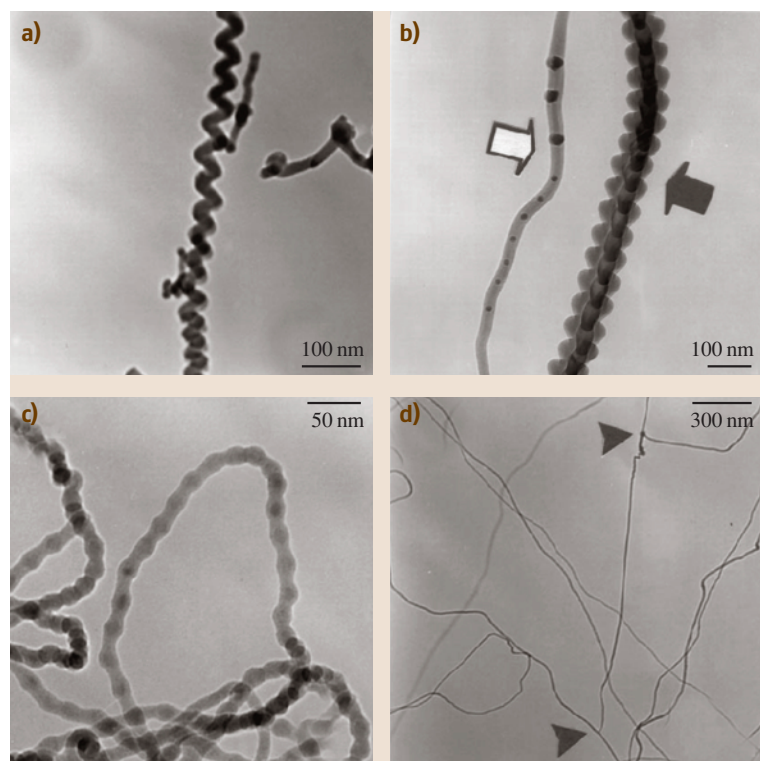
wire lengths, and have wire diameters in the range $20 \leq d_W \leq 150$ nm. The SEM micrograph in Fig. 4.11c

Fig. 4.13a–d TEM morphologies of four special forms of Si nanowires synthesized by the laser ablation of a Si powder target. **(a)** A spring-shaped Si nanowire; **(b)** fishbone-shaped (indicated by a *solid arrow*) and frogs egg-shaped (indicated by a *hollow arrow*) Si nanowires; and **(c)** pearl-shaped nanowires, while **(d)** shows poly-sites for the nucleation of silicon nanowires (indicated by *arrows*) [4.123]

Part A | 4.2

Transmission Electron Microscopy

TEM and high-resolution transmission electron microscopy (HRTEM) are powerful imaging tools for studying nanowires at the atomic scale, and they usually provide more detailed geometrical features than are seen in SEM images. TEM studies also yield information regarding the crystal structure, crystal quality, grain size, and crystal orientation of the nanowire axis. When operating in the diffraction mode, selected area electron diffraction (SAED) patterns can be made to determine the crystal structures of nanowires. As an example, the TEM images in Fig. 4.13 show four different morphologies for Si nanowires prepared by the laser ablation of a Si target [4.123]: (a) spring-shaped; (b) fishbone-shaped (indicated by solid arrow) and frogs egg-shaped (indicated by the hollow arrow), (c) pearl-shaped, while (d) shows the poly-sites of nanowire nucleation. The crystal quality of nanowires is revealed from high-resolution TEM images with atomic resolution, along with selected area electron diffraction (SAED) patterns. For example, Fig. 4.14 shows a TEM image of one of the GaN nanowires from Fig. 4.12, indicating single crystallinity and showing (100) lattice planes, thus indicating
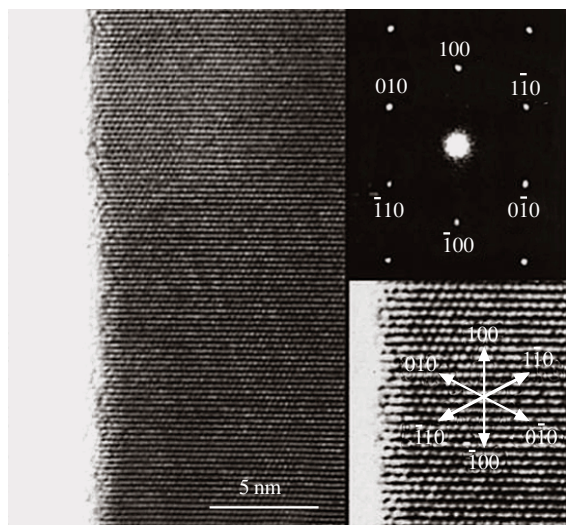
the growth direction of the nanowire. This information is supplemented by the corresponding electron diffraction pattern in the upper right. A more comprehensive review of the application of TEM for growth orientation indexing and crystal defect characterization in nanowires is available elsewhere [4.124].

The high resolution of the TEM also permits the surface structures of the nanowires to be studied. In many cases, the nanowires are sheathed with a native oxide layer, or an amorphous oxide layer that forms during the growth process. This can be seen in Fig. 4.6b for silicon nanowires and in Fig. 4.15 for germanium nanowires [4.35], showing a mass-thickness contrast TEM image and a selected-area electron diffraction pattern of a Ge nanowire. The main TEM image shows that these Ge nanowires possess an amorphous GeO_2 sheath with a crystalline Ge core that is oriented in the [211] direction.

Dynamical processes of the surface layer of nanowires can be studied in-situ using an environmental TEM chamber, which allows TEM observations to be made while different gases are introduced or as the sample is heat-treated at various temperatures, as illustrated in Fig. 4.16. The figure shows high-resolution TEM images of a Bi nanowire with an oxide coating and the effect of a dynamic oxide removal process
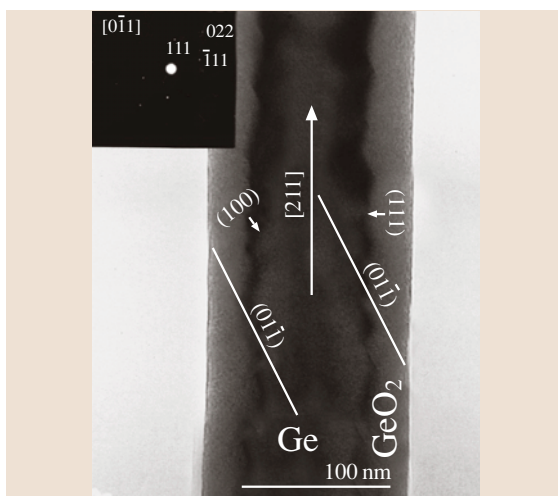

Fig. 4.14 Lattice-resolved high-resolution TEM image of one GaN nanowire (*left*) showing that (100) lattice planes are visible perpendicular to the wire axis. The electron diffraction pattern (*top right*) was recorded along the [001] zone axis. A lattice-resolved TEM image (*lower right*) highlights the continuity of the lattice up to the nanowire edge, where a thin native oxide layer is found. The directions of various crystallographic planes are indicated in the *lower right figure* [4.30]

Fig. 4.15 A mass-thickness contrast TEM image of a Ge nanowire taken along the [0$\bar{1}$1] zone axis and a selected-area electron diffraction pattern (*upper left inset*) [4.35]. The Ge nanowires were synthesized by laser ablation of a mixture of Ge and GeO_2 powder. The core of the Ge nanowire is crystalline, while the surface GeO_2 is amorphous

carried out within the environmental chamber of the TEM [4.125]. The amorphous bismuth-oxide layer coating the nanowire (Fig. 4.16a) is removed by exposure to hydrogen gas within the environmental chamber of the TEM, as indicated in Fig. 4.16b.

By coupling the powerful imaging capabilities of TEM with other characterization tools, such as an electron energy loss spectrometer (EELS) or an energy dispersive X-ray spectrometer (EDS) within the TEM instrument, additional properties of the nanowires can be probed with high spatial resolution. With the EELS technique, the energy and momentum of the incident and scattered electrons are measured in an inelastic electron scattering process to provide information on the energy and momentum of the excitations in the nanowire sample. Figure 4.17 shows the dependence on nanowire diameter of the electron energy loss spectra of Bi nanowires. The spectra were taken from the center of the nanowire, and the shift in the energy of the peak position (Fig. 4.17) indicates the effect of the nanowire diameter on the plasmon frequency in the nanowires. The results show that there are changes in the electronic structure of the Bi nanowires as the wire diameter decreases [4.126]. Such changes in electronic structure as a function of nanowire diameter are also observed in their transport (Sect. 4.2.2) and optical (Sect. 4.2.3) properties, and are related to quantum confinement effects.

EDS measures the energy and intensity distribution of X-rays generated by the impact of the electron beam on the surface of the sample. The elemental composition within the probed area can be determined to a high degree of precision. The technique was particularly useful for the compositional characterization of superlattice nanowires [4.90] and core-shell nanowires [4.111] (see Sect. 4.1.2).

Scanning Tunneling Probes

Several scanning probe techniques, such as scanning tunneling microscopy (STM) [4.127], electric field gradient microscopy (EFM) [4.13], magnetic field microscopy (MFM) [4.40], and scanning thermal microscopy (SThM) [4.128], combined with atomic force microscopy (AFM), have been employed to study the structural, electronic, magnetic, and thermal properties of nanowires. A scanning tunneling microscope can be employed to reveal both topographical structural information, such as that illustrated in Fig. 4.18, as well as information on the local electronic density of states of a nanowire, when used in the STS (scanning tunneling spectroscopy) mode. Figure 4.18 shows STM height im-
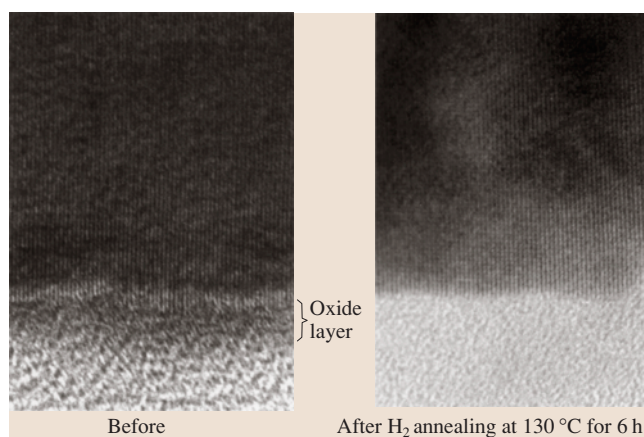

Before · After H_2 annealing at 130 °C for 6 h

Fig. 4.16 High-resolution transmission electron microscope (HRTEM) image of a Bi nanowire (*left*) before and (*right*) after annealing in hydrogen gas at 130 °C for six hours within the environmental chamber of the HRTEM instrument to remove the oxide surface layer [4.125]

ages (taken in the constant current STM mode) of MoSe molecular wires deposited from a methanol or acetonitrile solution of $Li_2Mo_6Se_6$ onto Au substrates. The STM image of a single MoSe wire (Fig. 4.18a) exhibits a 0.45 nm lattice repeat distance in a MoSe molecular wire. When both STM and STS measurements are made on the same sample, the electronic and structural
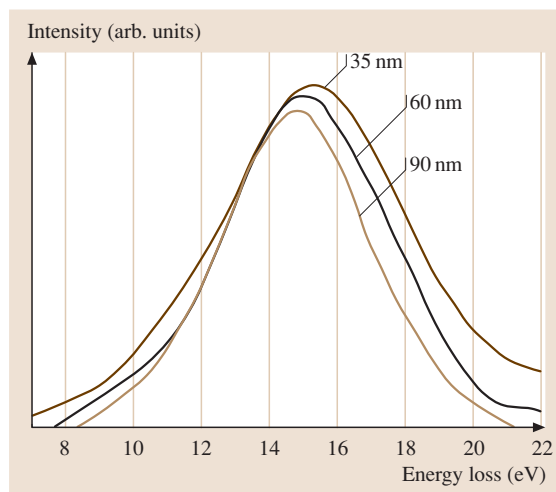

Fig. 4.17 Electron energy loss spectra (EELS) taken from the centers of bismuth nanowires with diameters of 35, 60 and 90 nm. The shift in the volume plasmon peaks is due to the effect of wire diameter on the electronic structure [4.126]

properties can be correlated, as for example in the joint STM/STS studies on Si nanowires [4.98], showing alternating segments of a single nanowire identified with growth along the [110] and [112] directions, and different I–V characteristics measured for the [110] segments as compared with the [112] segments.

Magnetic field microscopy (MFM) has been employed to study magnetic polarization of magnetic nanowires embedded in an insulating template, such as an anodic alumina template. For example, Fig. 4.19a shows the topographic image of an anodic alumina template filled with Ni nanowires, and Fig. 4.19b demonstrates the corresponding magnetic polarization of each nanowire in the template. This micrograph shows that a magnetic field microscopy probe can distinguish between spin-up and spin-down nanowires in the nanowire array, thereby providing a method for measuring interwire magnetic dipolar interactions [4.40].
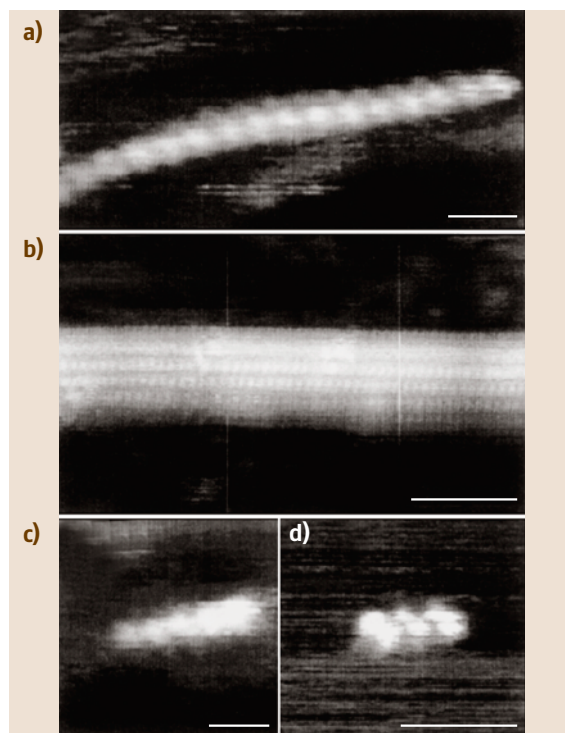

Fig. 4.18a–d STM height images, obtained in the constant current mode, of MoSe chains deposited on an Au(111) substrate. (**a**) A single chain image, and (**b**) a MoSe wire bundle. (**c**) and (**d**) are images of MoSe wire fragments containing five and three unit cells, respectively [4.127]. The scale bars are all 1 nm

X-Ray Analysis

Other characterization techniques that are commonly used to study the crystal structures and chemical compositions of nanowires include X-ray diffraction and X-ray energy dispersion analysis (EDAX). The peak positions in the X-ray diffraction pattern can be used to determined the chemical composition and the crystal phase structure of the nanowires. For example, Fig. 4.2 shows that Bi nanowires have the same crystal structure and lattice constants as bulk bismuth. Both the X-ray diffraction pattern (XRD) for an array of aligned Bi nanowires (Fig. 4.2) and the SAED pattern for individual Bi nanowires [4.13] suggest that the nanowires have a common axis of nanowire alignment.

As another example of an XRD pattern for an array of aligned nanowires, Fig. 4.20 shows the X-ray diffraction pattern of the ZnO nanowires that are displayed in Fig. 4.11. Only (00ℓ) diffraction peaks are observed for these aligned ZnO nanowires, indicating that their preferred growth direction is (001) along the wire axis. Similarly, XRD was used to confirm the different growth directions of GaN nanowire array grown epitaxially on (100) $LiAlO_2$ and (111) MgO substartes [4.117]

EDAX has been used to determine the chemical compositions and stoichiometries of compound nanowires or impurity contents in nanowires. However, the results from EDAX analysis should be interpreted carefully to avoid systematic errors.

4.2.2 Mechanical Properties

Thermal Stability

Due to the large surface area-to-volume ratio in nanowires and other nanoparticles, the thermal stability of nanowires is anticipated to differ significantly from that of the bulk material. Theoretical studies of materials in confined geometries show that the melting point of the material is reduced in nanostructures, as is the latent heat of fusion, and that large hysteresis can be observed in melting–freezing cycles. These phenomena have been studied experimentally in three types of nanowire systems: porous matrices impregnated with a plurality of nanowires, individual nanowires sheathed by a thin coating, and individual nanowires.

The melting freezing of matrix-supported nanowires can be studied by differential scanning calorimetry (DSC), since large volumes of samples can thus be produced. *Huber* et al. investigated the melting of indium in porous silica glasses with mean pore diameters ranging from 6 to 141 nm [4.129]. The melting point of the pore-confined indium shows a linear dependence on inverse
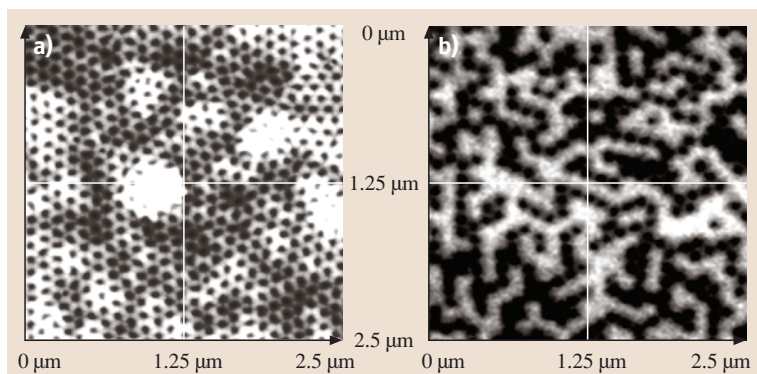
Fig. 4.19 (a) Topographic image of a highly-ordered porous alumina template with a period of 100 nm filled with 35 nm diameter nickel nanowires. **(b)** The corresponding MFM (magnetic force microscope) image of the nanomagnet array, showing that the pillars are magnetized alternately "up" (*white*) and "down" (*black*) [4.40]
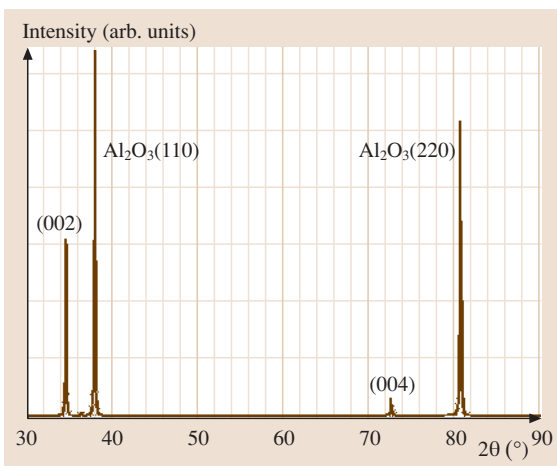
Fig. 4.20 X-ray diffraction pattern of aligned ZnO nanowires (see Fig. 4.11) grown on a sapphire substrate. Only [00ℓ] diffraction peaks are observed for the nanowires, owing to their well-oriented growth orientation. Strong diffraction peaks for the sapphire substrate are found [4.122]

analyzing the phase transition thermodynamics and kinetics. *Yang* et al. produced germanium nanowires coated with a thin (1–5 nm) graphite sheath, by pyrolysis of organic molecules over VLS-grown nanowires, and followed the melting and recrystallization of the germanium by variable temperature TEM imaging [4.130]. The melting of the nanowires was followed by the disappearance of the electronic diffraction pattern. It was found that the nanowires began melting from their ends, with the melting front advancing towards the center of the nanowire as the temperature was increased. During the cool-down part of the cycle, the recrystallization of the nanowire occurred instantaneously following significant supercooling. The authors report both the largest melting point suppression recorded thus far for germanium ($\approx 300\,°C$), and a large melting–recrystallization hysteresis of up to $\approx 300\,°C$. Similarly, carbon nanotubes have been filled with various low-temperature metals [4.131]. A nanothermometer has been demonstrated using a 10 nm liquid gallium filled-carbon nanotube, showing an expansion coefficient that is linear in temperature and identical to the bulk value [4.132].

A different behavior was observed in free-standing copper nanowires [4.133]. In this system, there is little interaction between the nanowire surface and the surroundings, and the nanowire is not confined in its diameter, as in the case of the sheathed nanowires. Thermal treatment of the free-standing nanowires leads to their fragmentation into a linear array of metal spheres. Thinner nanowires were more vulnerable than thicker nanowires to the thermal treatment, showing constrictions and segmentation at lower temperatures. Analysis of the temperature response of the nanowires indicates that the nanowire segmentation is a result of the Rayleigh instability, starting with oscillatory perturbations of the nanowire diameter, leading to long cylindrical segments,

pore diameter, with a maximum melting point depression of 50 °C. They also recorded a 6 °C difference in the melting temperature and the freezing temperature of 12.8 nm diameter indium. The melting profile of the pore-confined indium in these samples is broader in temperature than for bulk indium, as expected for the heterogeneity in the pore diameter and in the indium crystal size aspect ratio within the samples.

Sheathed nanowires provide an opportunity to study the melting and recrystallization of individual nanowires. The shell layer surrounding the nanowire provides confinement to keep the liquid phase within the inner cylindrical volume. However, the shell–nanowire surface interaction should be taken into account when

that become more separated and more spherical at higher temperatures. These observations indicate that annealing and melting are dominated by the surface diffusion of atoms on the entire surface of the nanowire (versus tip-initiated melting).

4.2.3 Transport Properties

The study of electrical transport properties of nanowires is important for nanowire characterization, electronic device applications, and the investigation of unusual transport phenomena arising from one-dimensional quantum effects. Important factors that determine the transport properties of nanowires include the wire diameter, (important for both classical and quantum size effects), material composition, surface conditions, crystal quality, and the crystallographic orientation along the wire axis for materials with anisotropic material parameters, such as the effective mass tensor, the Fermi surface, or the carrier mobility.

Electronic transport phenomena in low-dimensional systems can be roughly divided into two categories: ballistic transport and diffusive transport. Ballistic transport phenomena occur when the electrons can travel across the nanowire without any scattering. In this case, the conduction is mainly determined by the contacts between the nanowire and the external circuit, and the conductance is quantized into an integral number of universal conductance units $G_0 = 2e^2/h$ [4.134, 135]. Ballistic transport phenomena are usually observed in very short quantum wires, such as those produced using mechanically controlled break junctions (MCBJ) [4.136, 137] where the electron mean free path is much longer than the wire length and the conduction is a pure quantum phenomenon. To observe ballistic transport, the thermal energy must also obey the relation $k_B T \ll \varepsilon_j - \varepsilon_{j-1}$, where $\varepsilon_j - \varepsilon_{j-1}$ is the energy separation between subband levels j and $j-1$. On the other hand, for nanowires with lengths much larger than the carrier mean free path, the electrons (or holes) undergo numerous scattering events when they travel along the wire. In this case, the transport is in the diffusive regime, and the conduction is dominated by carrier scattering within the wires, due to phonons (lattice vibrations), boundary scattering, lattice and other structural defects, and impurity atoms.

Conductance Quantization in Metallic Nanowires

The ballistic transport of 1-D systems has been extensively studied since the discovery of quantized conductance in 1-D systems in 1988 [4.134, 135]. The

phenomena of conductance quantization occur when the diameter of the nanowire is comparable to the electron Fermi wavelength, which is on the order of 0.5 nm for most metals [4.138]. Most conductance quantization experiments up to the present were performed by bringing together and separating two metal electrodes. As the two metal electrodes are slowly separated, a nanocontact is formed before it breaks completely (see Fig. 4.21a), and conductance in integral multiple values of G_0 is observed through these nanocontacts. Figure 4.21b shows the conductance histogram built with 18 000 contact breakage curves between two gold electrodes at room temperature [4.139], with the electrode separation up to ≈ 1.8 nm. The conductance quantization behavior is found to be independent of the contact material, and has been observed in various metals, such as Au [4.139], Ag, Na, Cu [4.140], and Hg [4.141]. For semimetals such as Bi, conductance quantization has also been observed for electrode separations as long as 100 nm at 4 K because of the long Fermi wavelength (≈ 26 nm) [4.138], indicating that the conductance quantization may be due to the existence of well-defined quantum states localized at a constriction instead of resulting from the atom rearrangement as the electrodes separate. Since conductance quantization is only observed in breaking contacts, or for very narrow and very short nanowires, most nanowires of practical interest (possessing lengths of several microns) lie in the diffusive transport regime, where the carrier scattering is significant and should be considered.

I−V Characterization of Semiconducting Nanowires

The electronic transport behavior of nanowires may be categorized based on the relative magnitudes of three length scales: carrier mean free path ℓ_W, the de Broglie wavelength of electrons λ_e, and the wire diameter d_W. For wire diameters much larger than the carrier mean free path ($d_W \gg \ell_W$), the nanowires exhibit transport properties similar to bulk materials, which are independent of the wire diameter, since the scattering due to the wire boundary is negligible compared to other scattering mechanisms. For wire diameters comparable to or smaller than the carrier mean free path ($d_W \approx \ell_W$ or $d_W < \ell_W$), but still much larger than the de Broglie wavelength of the electrons ($d_W \gg \lambda_e$), the transport in nanowires is in the classical finite size regime, where the band structure of the nanowire is still similar to that of bulk, while the scattering events at the wire boundary alter their transport behavior. For wire diameters comparable to the electronic wavelength $d_W \approx \lambda_e$, the electronic density of states is altered dramatically and

quantum sub-bands are formed due to the quantum confinement effect at the wire boundary. In this regime, the transport properties are further influenced by the change in the band structure. Therefore, transport properties for nanowires in the classical finite size and quantum size regimes are highly diameter-dependent.

Researchers have investigated the transport properties of various semiconducting nanowires and have demonstrated their potential for diverse electronic devices, such as for p-n diodes [4.142, 143], field effect transistors [4.142], memory cells, and switches [4.144] (see Sect. 4.3.1). So far, the nanowires studied in this context have usually been made from conventional semiconducting materials, such as group IV and III–V compound semiconductors, via the VLS growth method (see Sect. 4.1.2), and their nanowire properties have been compared to their well-established bulk properties. Interestingly, the physical principles for describing bulk semiconductor devices also hold for devices based on these semiconducting nanowires with wire diameters of tens of nanometers. For example, Fig. 4.22 shows the current-voltage (I–V) behavior of a 4-by-1 crossed p-Si/n-GaN junction array at room temperature [4.142]. The long horizontal wire in the figure is a p-Si nanowire (10–25 nm in diameter) and the four short vertical wires are n-GaN nanowires (10–30 nm in diameter). Each of the four nanoscale cross points independently forms a p-n junction with current rectification behavior, as shown by the I–V curves in Fig. 4.22, and the junction behavior (for example the turn-on voltage) can be controlled by varying the oxide coating on these nanowires [4.142].

Huang et al. have demonstrated nanowire junction diodes with a high turn-on voltage (≈ 5 V) by increasing the oxide thickness at the junctions. The high turn-on voltage enables the use of the junction in a nanoscale FET, as shown in Fig. 4.23 [4.142] where I–V data for a p-Si nanowire are presented, for which the n-GaN nanowire with a thick oxide coating is used as a nanogate. By varying the nanogate voltage, the conductance of the p-Si nanowire can be changed by more than a factor of 10^5 (lower curve in the inset), whereas the conductance changes by only a factor of 10 when a global back-gate is used (top curve in the inset of Fig. 4.23). This behavior may be due to the thin gate dielectric between the crossed nanowires and the better control of the local carrier density through a nanogate. Based on the gate-dependent I–V data from these p-Si nanowires, it is found that the mobility of the holes in the p-Si nanowires may be higher than that for bulk p-Si, although further investigation is required for complete understanding.
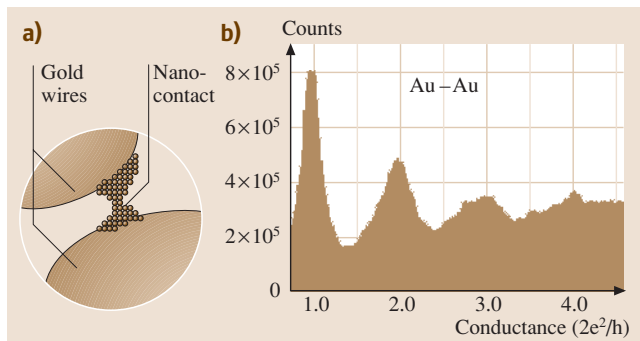

Fig. 4.21 (a) Schematic representation of the last stages of the contact breakage process [4.139]. **(b)** Histogram of conductance values built with 18 000 gold contact breakage experiments in air at room temperature, showing conductance peaks at integral values of G_0. In this experiment the gold electrodes approach and separate at 89 000 Å/s [4.139]

Because of the enhanced surface-to-volume ratios of nanowires, their transport behavior may be modified by changing their surface conditions. For example, researchers have found that by coating n-InP nanowires with a layer of redox molecules, such as cobalt phthalocyanine, the conductance of the InP
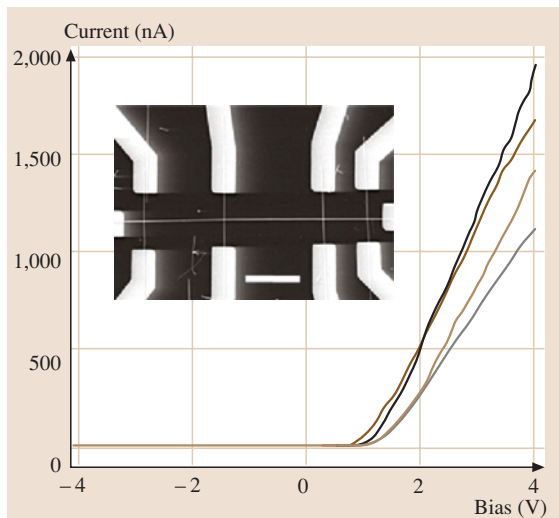

Fig. 4.22 I–V behavior for a 4(p) by 1(n) crossed p-Si/n-GaN junction array shown in the inset. The four curves represent the I–V response for each of the four junctions, showing similar current rectifying characteristics in each case. The length scale bar between the two middle junctions is 2 µm [4.142]. The p-Si and n-GaN nanowires are 10–25 nm and 10–30 nm in diameter, respectively

nanowires may change by orders of magnitude upon altering the charge state of the redox molecules to provide bistable nanoscale switches [4.144]. The resistance (or conductance) of some nanowires (such as Pd nanowires) is also very sensitive to the presence of certain gases (e.g., H_2) [4.145, 146], and this property may be utilized for sensor applications to provide improved sensitivity compared to conventional sensors based on bulk material (see Sect. 4.3.4).

Although it remains unclear how the size effect may influence the transport properties and device performance of semiconducting nanowires, many of the larger diameter semiconducting nanowires are expected to be described by classical physics, since their quantization energies $\hbar^2/(2m_e d_W^2)$ are usually smaller than the thermal energy $k_B T$. By comparing the quantization energy with the thermal energy, the critical wire diameter below which quantum confinement effects become significant is estimated to be 1 nm for Si nanowires at room temperature, which is much smaller than the sizes of many of the semiconducting nanowires that have been investigated so far. By using material systems with much smaller effective carrier masses m_e (such as bismuth), the critical diameter for which such quantum effects can be observed is increased, thereby facilitating the study of quantum confinement effects. It is for this rea-

son that the bismuth nanowire system has been studied so extensively. Furthermore, since the crystal structure and lattice constants of bismuth nanowires are the same as for 3-D crystalline bismuth, it is possible to carry out detailed model calculations to guide and to interpret transport and optical experiments on bismuth nanowires. For these reasons, bismuth can be considered a model system for studying 1-D effects in nanowires.

Temperature–Dependent Resistance Measurements

Although nanowires with electronic properties similar to their bulk counterparts are promising for constructing nanodevices based on well-established knowledge of their bulk counterparts, it is expected that quantum size effects in nanowires will likely be utilized to generate new phenomena absent in bulk materials, and thus provide enhanced performance and novel functionality for certain applications. In this context, the transport properties of bismuth (Bi) nanowires have been extensively studied, both theoretically [4.147] and experimentally [4.8, 10, 78, 148–150] because of their promise for enhanced thermoelectric performance. Transport studies of ferromagnetic nanowire arrays, such as Ni or Fe, have also received much attention because of their potential for high-density magnetic storage applications [4.151].

The very small electron effective mass components and the long carrier mean free paths in Bi facilitate the study of quantum size effects in the transport properties of nanowires. Quantum size effects are expected to become significant in bismuth nanowires with diameters smaller than 50 nm [4.147], and the fabrication of crystalline nanowires with this diameter range is relatively easy.

Figure 4.24a shows the T dependence of the resistance $R(T)$ for Bi nanowires ($7 \leq d_W < 200$ nm) synthesized by vapor deposition and pressure injection [4.8], illustrating the quantum effects in their temperature-dependent resistance. In Fig. 4.24a, the $R(T)$ behavior of Bi nanowires is dramatically different from that of bulk Bi, and is highly sensitive to the wire diameter. Interestingly, the $R(T)$ curves in Fig. 4.24a show a nonmonotonic trend for large-diameter (70 and 200 nm) nanowires, although $R(T)$ becomes monotonic with T for small-diameter (≤ 48 nm) nanowires. This dramatic change in the behavior of $R(T)$ as a function of d_W is attributed to a unique semimetal–semiconductor transition phenomena in Bi [4.78], induced by quantum size effects. Bi is a semimetal in bulk form, in which the T-point valence band overlaps with the L-point con-
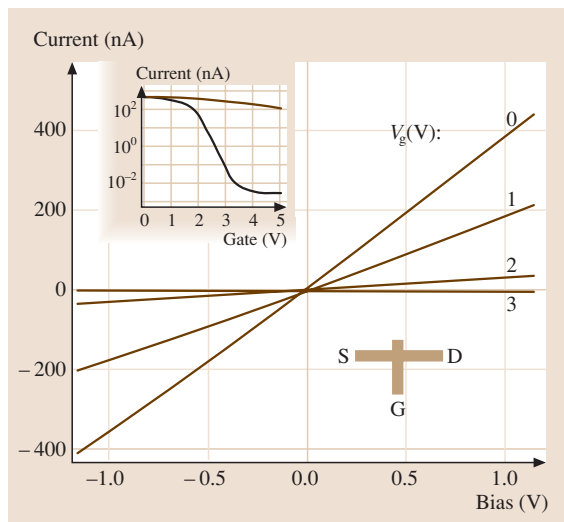

Fig. 4.23 Gate-dependent I–V characteristics of a crossed nanowire field-effect transistor (FET). The n-GaN nanowire is used as the nanogate, with the gate voltage indicated (0, 1, 2, and 3 V). The *inset* shows the current versus V_{gate} for a nanowire gate (*lower curve*) and for a global back-gate (*top curve*) when the bias voltage is set to 1 V [4.142]

duction band by 38 meV at 77 K. As the wire diameter decreases, the lowest conduction sub-band increases in energy and the highest valence sub-band decreases in energy. Model calculations predict that the band overlap should vanish in Bi nanowires (with their wire axes along the trigonal direction) at a wire diameter ≈ 50 nm [4.147].

The resistance of Bi nanowires is determined by two competing factors: the carrier density that increases with T, and the carrier mobility that decreases with T. The nonmonotonic $R(T)$ for large-diameter Bi nanowires is due to a smaller carrier concentration variation at low temperature (≤ 100 K) in semimetals, so that the electrical resistance is dominated by the mobility factor in this temperature range. Based on the semi-classical transport model and the estab-

lished band structure of Bi nanowires, the calculated $R(T)/R(300\,\text{K})$ for 36 nm and 70 nm Bi nanowires is shown by the solid curves in Fig. 4.24c to illustrate different $R(T)$ trends for semiconducting and semimetallic nanowires, respectively [4.78]. The curves in Fig. 4.24c exhibit trends consistent with experimental results. The condition for the semimetal–semiconductor transition in Bi nanowires can be experimentally determined, as shown by the measured resistance ratio $R(10\,\text{K})/R(100\,\text{K})$ of Bi nanowires as a function of wire diameter [4.152] in Fig. 4.25. The maximum in the resistance ratio $R(10\,\text{K})/R(100\,\text{K})$ at $d_W \approx 48$ nm indicates the wire diameter for the transition of Bi nanowires from a semimetallic phase to a semiconducting phase. The semimetal–semiconductor transition and the semiconducting phase in Bi nanowires are examples of new
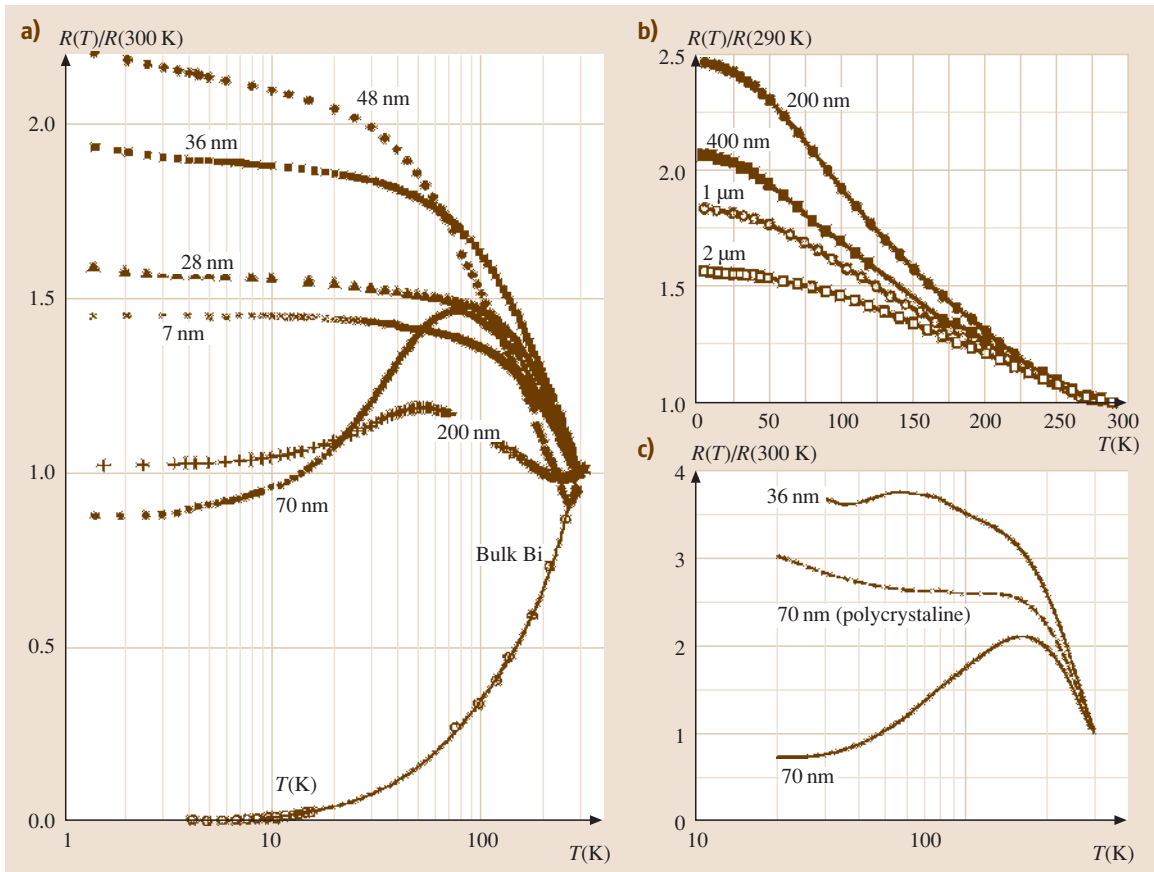
Fig. 4.24 (a) Measured temperature dependence of the resistance $R(T)$ normalized to the room temperature (300 K) resistance for bismuth nanowire arrays of various wire diameters d_W [4.8]. **(b)** $R(T)/R(290\,K)$ for bismuth wires of larger d_W and lower mobility [4.10]. **(c)** Calculated $R(T)/R(300\,\text{K})$ of 36 nm and 70 nm bismuth nanowires. The *dashed curve* refers to a 70 nm polycrystalline wire with increased boundary scattering [4.78]

transport phenomena resulting from low dimensionality that are absent in the bulk 3-D phase, and these phenomena further increase the possible benefits from the properties of nanowires for desired applications (see Sect. 4.3.2).

It should be noted that good crystal quality is essential for observing the quantum size effect in nanowires, as shown by the $R(T)$ plots in Fig. 4.24a. For example, Fig. 4.24b shows the normalized $R(T)$ measurements of Bi nanowires with larger diameters (200 nm–2 μm) prepared by electrochemical deposition [4.10], and these nanowires possess monotonic $R(T)$ behaviors, quite different from those of the corresponding nanowire diameters shown in Fig. 4.24a. The absence of the resistance maximum in Fig. 4.24b is due to the lower crystalline quality for nanowires prepared by electrochemical deposition, which tends to produce polycrystalline nanowires with a much lower carrier mobility. This monotonic $R(T)$ for semimetallic Bi nanowires with a higher defect level is also confirmed by theoretical calculations, as shown by the dashed curve in Fig. 4.24c for 70 nm wires with increased grain boundary scattering [4.154].

The theoretical model developed for Bi nanowires not only provides good agreement with experimental results, but it also plays an essential role in understanding the influence of the quantum size effect, the boundary scattering, and the crystal quality on their electrical properties. While the electronic density of states may be significantly altered due to quantum confinement effects, various scattering mechanisms related to
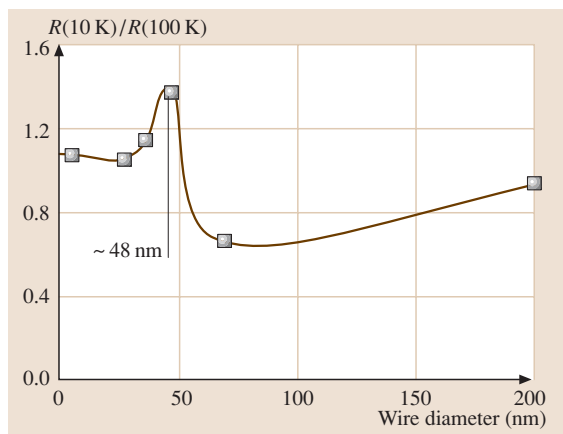

Fig. 4.26 Temperature dependence of the resistance of Zn nanowires synthesized by vapor deposition in various porous templates [4.52]. The data are given as points, the *full lines* are fits to a T^1 law for 15 nm diameter Zn nanowires in an SiO$_2$ template, denoted by Zn/SiO$_2$. Fits to a combined T^1 and $T^{-1/2}$ law were made for the smaller nanowire diameter composite samples denoted by Zn 9 nm /Al$_2$O$_3$ and Zn 4 nm/Vycor glass

Fig. 4.25 Measured resistance ratio $R(10\,\text{K})/R(100\,\text{K})$ of Bi nanowire array as a function of diameter. The peak indicates the transition from a semimetallic phase to a semiconducting phase as the wire diameter decreases [4.153]
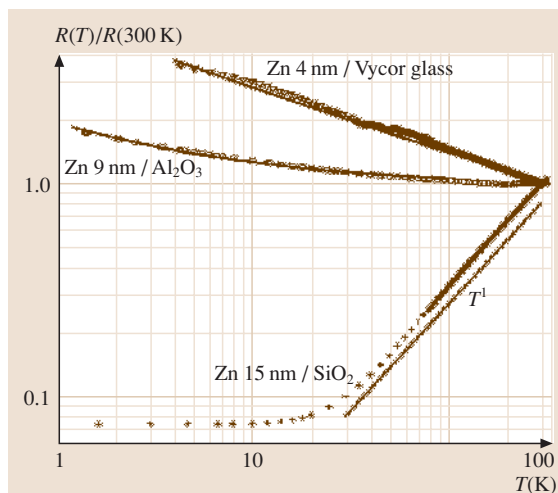
the transport properties of nanowires can be accounted for by Matthiessen's rule. Furthermore, the transport model has also been generalized to predict the transport properties of Te-doped Bi nanowires [4.78], Sb nanowires [4.155], and BiSb alloy nanowires [4.156], and good agreement between experiment and theory has also been obtained for these cases.

For nanowires with diameters comparable to the phase-breaking length, their transport properties may be further influenced by localization effects. It has been predicted that in disordered systems, the extended electronic wavefunctions become localized near defect sites, resulting in the trapping of carriers and giving rise to different transport behavior. Localization effects are also expected to be more pronounced as the dimensionality and sample size are reduced. Localization effects on the transport properties of nanowire systems have been studied on Bi nanowires [4.157] and, more recently, on Zn nanowires [4.52]. Figure 4.26 shows the measured $R(T)/R(300\,\text{K})$ of Zn nanowires fabricated by vapor deposition in porous silica or alumina [4.52]. While 15 nm Zn nanowires exhibit an $R(T)$ behavior with a T^1 dependence as expected for a metallic wire, the $R(T)$ of 9 nm and 4 nm Zn nanowires exhibits a temperature dependence of $T^{-1/2}$ at low temperatures, consistent with

1-D localization theory. Thus, due to this localization effect, the use of nanowires with very small diameters for transport applications may be limited.

Magnetoresistance

Magnetoresistance (MR) measurements provide an informative technique for characterizing nanowires, because these measurements yield a great deal of information about the electron scattering with wire boundaries, the effects of doping and annealing on scattering, and localization effects in the nanowires [4.150]. For example, at low fields the MR data show a quadratic dependence on the B field from which carrier mobility estimates can be made (see Fig. 4.27 at low B field).

Figure 4.27 shows the longitudinal magnetoresistance (B parallel to the wire axis) for 65 nm and 109 nm Bi nanowire samples (before thermal annealing) at 2 K. The MR maxima in Fig. 4.27a are due to the classical size effect, where the wire boundary scattering is reduced as the cyclotron radius becomes smaller than the wire radius in the high field limit, resulting in a decrease in the resistivity. This behavior is typical for the longitudinal MR of Bi nanowires in the diameter range of 45 nm to 200 nm [4.8, 149, 150, 158], and the peak position B_m moves to lower B field values as the wire diameter in-

creases, as shown in Fig. 4.27c [4.158], where B_m varies linearly with $1/d_W$. The condition for the occurrence of B_m is approximately given by $B_m \approx 2c\hbar k_F/ed_W$ where k_F is the wave vector at the Fermi energy. The peak position, B_m, is found to increase linearly with increasing temperature in the range of 2 to 100 K, as shown in Fig. 4.27b [4.158]. As T is increased, phonon scattering becomes increasingly important, and therefore a higher magnetic field is required to reduce the resistivity associated with boundary scattering sufficiently to change the sign of the MR. Likewise, increasing the grain boundary scattering is also expected to increase the value of B_m at a given T and wire diameter.

The presence of the peak in the longitudinal MR of nanowires requires a high crystal quality with long carrier mean free paths along the nanowire axis, so that most scattering events occur at the wire boundary instead of at a grain boundary, at impurity sites, or at defect sites within the nanowire. *Liu* et al. have investigated the MR of 400 nm Bi nanowires synthesized by electrochemical deposition [4.74], and no peak in the longitudinal MR is observed. The absence of a magnetoresistance peak may be attributed to a higher defect level in the nanowires produced electrochemically and to a large wire diameter, much longer than the carrier mean free
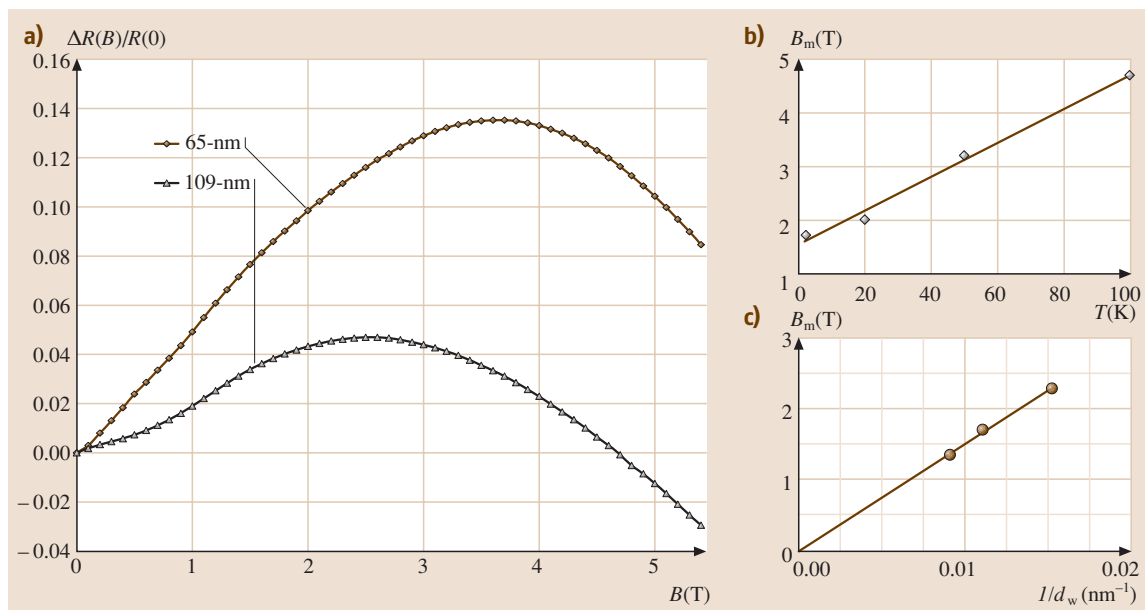
Fig. 4.27 (**a**) Longitudinal magnetoresistance, $\Delta R(B)/R(0)$, at 2 K as a function of B for Bi nanowire arrays with diameters of 65 and 109 nm before thermal annealing. (**b**) The peak position B_m as a function of temperature for the 109 nm diameter Bi nanowire array after thermal annealing. (**c**) The peak position B_m of the longitudinal MR (after thermal annealing) at 2 K as a function of $1/d_W$, the reciprocal of the nanowire diameter [4.158]

path. The negative MR observed for the Bi nanowire arrays above B_m (see Fig. 4.27) shows that wire boundary scattering is a dominant scattering process for the longitudinal magnetoresistance, thereby establishing that the mean free path is larger than the wire diameter and that a ballistic transport behavior is indeed observed in the high field regime.

In addition to the longitudinal magnetoresistance measurements, transverse magnetoresistance measurements ($\boldsymbol{B}$ perpendicular to the wire axis) have also been performed on Bi nanowire array samples [4.8, 150, 158], where a monotonically increasing B^2 dependence over the entire range $0 \le B \le 5.5\,T$ is found for all Bi nanowires studied thus far. This is as expected, since the wire boundary scattering cannot be reduced by a magnetic field perpendicular to the wire axis. The transverse magnetoresistance is also found to be always larger than the longitudinal magnetoresistance in nanowire arrays.

By applying a magnetic field to nanowires at very low temperatures ($\le 5\,K$), one can induce a transition from a 1-D confined system at low magnetic fields to a 3-D confined system as the field strength increases, as shown in Fig. 4.28 for the longitudinal MR of Bi nanowire arrays of various nanowire diameters ($28-70\,nm$) for $T < 5\,K$ [4.150]. In these curves, a subtle step-like feature is seen at low magnetic fields, which is found to depend only on the wire diameter, and is independent of temperature, the orientation of the magnetic field, and even on the nanowire material (see for example Sb nanowires [4.155]). The lack of a dependence of the magnetic field at which the step appears on temperature, field orientation, and material type indicates that the phenomenon is related to the magnetic field length, $L_H = (\hbar/eB)^{1/2}$. The characteristic length L_H is the spatial extent of the wave function of electrons in the lowest Landau level, and L_H is independent of the carrier effective masses. Setting $L_H(B_c)$ equal to the diameter d_W of the nanowire defines a critical magnetic field strength, B_c, below which the wavefunction is confined by the nanowire boundary (the 1-D regime), and above which the wavefunction is confined by the magnetic field (the 3-D regime). The physical basis for this phenomenon is associated with confinement of a single magnetic flux quantum within the nanowire cross-section [4.150]. This phenomenon, though independent of temperature, is observed for $T \le 5\,K$, since the phase breaking length has to be larger than the wire diameter. This calculated field strength, B_c, indicated in Fig. 4.28 by vertical lines for the appropriate nanowire diameters, provides a good fit to the step-like features in these MR curves.
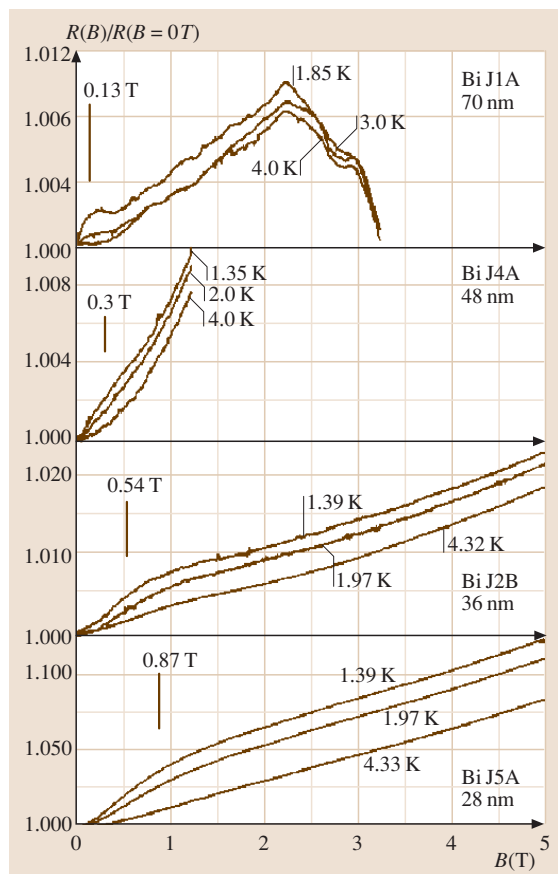

Fig. 4.28 Longitudinal magnetoresistance as a function of magnetic field for Bi nanowires of the diameters indicated. The *vertical bars* indicate the critical magnetic field B_c at which the magnetic length equals the nanowire diameter [4.150]

The Shubnikov–de Haas (SdH) quantum oscillatory effect, which results from the passage of the quantized Landau levels through the Fermi energy as the field strength varies, should, in principle, provide the most direct measurement of the Fermi energy and carrier density. For example, *Heremans* et al. have demonstrated that SdH oscillations can be observed in Bi nanowire samples with diameters down to 200 nm [4.159], and they have demonstrated that Te doping can be used to raise the Fermi energy in Bi nanowires. Such information on the Fermi energy is important because, for certain applications based on nanowires, it is necessary to place the Fermi energy near a sub-band edge where the density of states has a sharp feature. However, due to the unusual 1-D geometry of nanowires, other char-

acterization techniques that are commonly used in bulk materials to determine the Fermi energy and the carrier concentration (such as Hall measurement) cannot be applied to nanowire systems. The observation of the SdH oscillatory effect requires crystal samples of very high quality which allow carriers to execute a complete cyclotron orbit in the nanowire before they are scattered. For small nanowire diameters, large magnetic fields are required to produce cyclotron radii smaller than the wire radius. For some nanowire systems, all Landau levels may have passed through the Fermi level at such a high field strength, and in such a case, no oscillations can be observed. The localization effect may also prevent the observation of SdH oscillations for very small diameter (≤ 10 nm) nanowires. Observing SdH oscillations in highly doped samples (as may be required for certain applications) may be difficult because impurity scattering reduces the mean free path, requiring high B fields to satisfy the requirement that carriers complete a cyclotron orbit prior to scattering. Therefore, although SdH oscillations provide the most direct method of measuring the Fermi energy and carrier density of nanowire samples, this technique may, however, not work for small-diameter nanowires, nor for nanowires that are heavily doped.

Thermoelectric Properties

Nanowires are predicted to hold great promise for thermoelectric applications [4.147, 161], due to their novel band structure compared to their bulk counterparts and the expected reduction in thermal conductivity associated with enhanced boundary scattering (see below). Due to the sharp density of states at the 1-D subband edges (where the van Hove singularities occur), nanowires are expected to exhibit enhanced Seebeck coefficients compared to their bulk counterparts. Since the Seebeck coefficient measurement is intrinsically independent of the number of nanowires contributing to the signal, the measurements on nanowire arrays of uniform wire diameter are, in principle, as informative as single-wire measurements. The major challenge with measuring the Seebeck coefficients of nanowires lies in the design of tiny temperature probes to accurately determine the temperature difference across the nanowire. Figure 4.29a shows the schematic experimental set-up for the Seebeck coefficient measurement of nanowire arrays [4.160], where two thermocouples are placed on both faces of a nanowire array and a heater is attached to one face of the array to generate a temperature gradient along the nanowire axis. Ideally, the size of the thermocouples should be much smaller than the thickness of

the nanowire array template (i. e. the nanowire length) to minimize error. However, due to the thinness of most templates (≤ 50 μm) and the large size of commercially-available thermocouples (≈ 12 μm), the measured Seebeck coefficient values are usually underestimated.

The thermoelectric properties of Bi nanowire systems have been investigated extensively because of their potential as good thermoelectric materials. Figure 4.29b shows the measured Seebeck coefficients $S(T)$ as a function of temperature for nanowire arrays with diameters of 40 and 65 nm and different isoelectronic Sb alloy concentrations [4.154], and $S(T)$ results for bulk Bi are shown (solid curve) for comparison. Thermopower enhancement is observed in Fig. 4.29b as the wire diameter decreases and as the Sb content increases, which is attributed to the semimetal–semiconductor transition induced by quantum confinement and to Sb alloying effects in $Bi_{1-x}Sb_x$ nanowires. *Heremans* et al. have
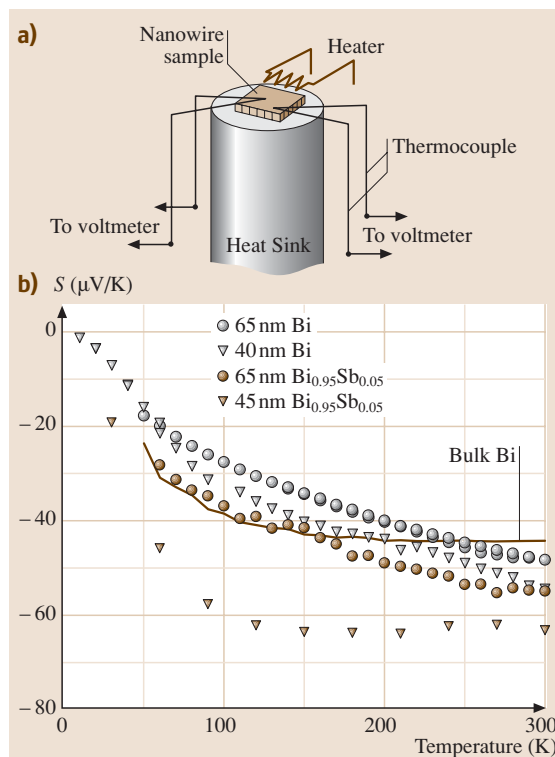

Fig. 4.29 (a) Experimental set-up for the measurement of the Seebeck coefficient in nanowire arrays [4.160]. **(b)** Measured Seebeck coefficient as a function of temperature for Bi (∘, ▽) and $Bi_{0.95}Sb_{0.05}$ (•, ▼) nanowires with different diameters. The *solid curve* denotes the Seebeck coefficient for bulk Bi [4.154]

observed a substantial increase in the thermopower of Bi nanowires as the wire diameter decreases further, as shown in Fig. 4.30a for 15 nm Bi/silica and 9 nm Bi/alumina nanocomposites [4.52]. The enhancement is due to the sharp density of states near the Fermi energy in a 1-D system. Although the samples in Fig. 4.30a also possess very high electrical resistance ($\sim G\Omega$), the results for the 9 nm Bi/alumina samples show that the Seebeck coefficient can be enhanced by almost 1000 times relative to bulk material. However, for Bi nanowires with very small diameters (≈ 4 nm), the localization effect becomes dominant, which compromises the thermopower enhancement. Therefore, for Bi nanowires, the optimal wire diameter range for the largest thermopower enhancement is found to be between 4 and 15 nm [4.52].

The effect of the nanowire diameter on the thermopower of nanowires has also been observed in Zn nanowires [4.52]. Figure 4.30b shows the Seebeck coefficient of 9 nm Zn/alumina and 4 nm Zn/Vycor glass nanocomposites, also exhibiting enhanced thermopower as the wire diameter decreases. It is found that while 9 nm Zn nanowires still exhibit metallic behavior, the thermopower of 4 nm Zn nanowires shows a different temperature dependence, which may be due to the 1-D localization effect, although further investigation is

required for definitive identification of the conduction mechanism in such small nanowires.

Quantum Wire Superlattices

The studies on superlattice nanowires, which possess a periodic modulation in their materials composition along the wire axis, have attracted much attention recently because of their promise in various applications, such as thermoelectrics (see Sect. 4.3.2) [4.90, 162], nanobarcodes (see Sect. 4.3.3) [4.110], nanolasers (see Sect. 4.3.3) [4.92], one-dimensional waveguides, and resonant tunneling diodes [4.94, 163]. Figure 4.31a shows a schematic structure of a superlattice nanowire consisting of interlaced quantum dots of two different materials, as denoted by A and B. Various techniques have been developed to synthesize superlattice nanowire structures with different interface conditions, as mentioned in Sect. 4.1.1 and Sect. 4.1.2.

In this superlattice (SL) nanowire structure, the electronic transport along the wire axis is made possible by the tunneling between adjacent quantum dots, while the uniqueness of each quantum dot and its 0D characteristic behavior is maintained by the energy difference of the conduction or valence bands between quantum dots of different materials (see Fig. 4.31b), which provides some amount of quantum confinement. Recently,
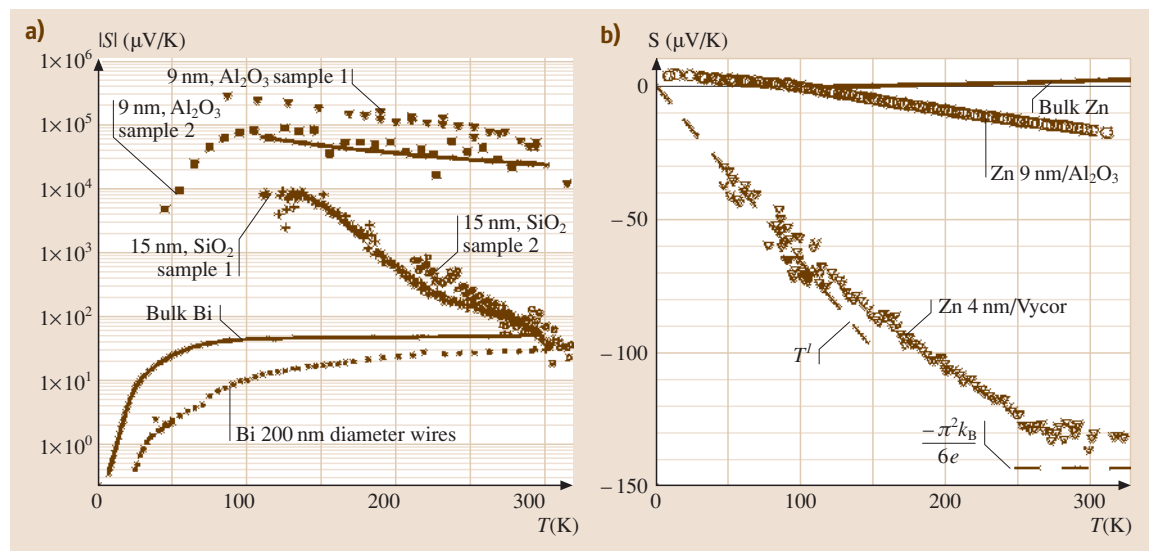
Fig. 4.30 (a) Absolute value of the Seebeck coefficient of two 15 nm Bi/silica and two 9 nm Bi/alumina nanocomposite samples, in comparison to bulk Bi and 200 nm Bi nanowires in the pores of alumina templates [4.52]. The *full line* on top part of the figure is a fit to a T^{-1} law. The Seebeck coefficient of the 9 nm Bi/alumina composite is positive; the rest are negative. **(b)** The Seebeck coefficient of 9 nm Zn/Al$_2$O$_3$ and 4 nm Zn/Vycor glass nanocomposite samples in comparison to bulk Zn [4.52]

Björk et al. have observed interesting nonlinear I–V characteristics with a negative differential resistance in one-dimensional heterogeneous structures made of InAs and InP, where InP serves as the potential barrier [4.94, 163]. The nonlinear I–V behavior is associated with the double barrier resonant tunneling process in one-dimensional structures, demonstrating that transport phenomena occur in superlattice nanowires via tunneling and the possibility of controlling the electronic band structure of the SL nanowires by carefully selecting the constituent materials. This new kind of structure is especially attractive for thermoelectric applications, because the interfaces between the nanodots can reduce the lattice thermal conductivity by blocking the phonon conduction along the wire axis, while electrical conduction may be sustained and even benefit from the unusual electronic band structures due to the periodic potential perturbation. For example, Fig. 4.32 shows the calculated dimensionless thermoelectric figure of merit $ZT = S^2 \sigma T / \kappa$ (see Sect. 4.3.2) where κ is the total thermal conductivity (including both the lattice and electronic contributions) of 10 nm-diameter PbS/PbSe superlattice nanowires as a function of the segment length. A higher thermoelectric performance than for PbSe$_{0.5}$S$_{0.5}$ alloy nanowires can be achieved for a 10 nm-diameter superlattice nanowire with segment lengths ≤ 7 nm. However, the localization effect, which may become important for very short segment lengths, may jeopardize this enhancement in the ZT of superlattice nanowires [4.153].

Thermal Conductivity of Nanowires
Experimental measurements of the temperature dependence of the thermal conductivity $\kappa(T)$ of individual
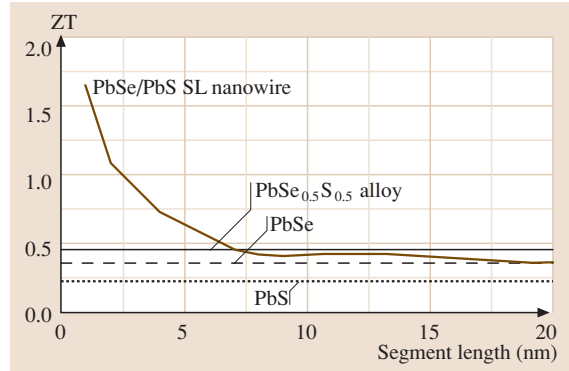
Fig. 4.32 Optimal ZT calculated as a function of segment length for 10 nm diameter PbSe/PbS nanowires at 77 K, where "optimal" refers to the placement of the Fermi level to optimize ZT. The optimal ZT for 10 nm-diameter PbSe, PbS, and PbSe$_{0.5}$S$_{0.5}$ nanowires are 0.33, 0.22, and 0.48, respectively [4.153]

suspended nanowires have been carried out on study the dependence of $\kappa(T)$ on wire diameter. In this context, measurements have been made on nanowires down to only 22 nm in diameter [4.164]. Such measurements are very challenging and are now possible due to technological development in the micro- and nano-fabrication of miniature thermal sensors, and the use of nanometer-size thermal scanning probes [4.128, 165, 166]. The experiments show that the thermal conductivity of small homogeneous nanowires may be more than one order of magnitude smaller than in the bulk, due mainly to strong boundary scattering effects [4.167]. Phonon confinement effects may eventually become important in nanowires with even smaller diameters. Measurements on mats of nanowires (see, for example, Fig. 4.12) do not generally give reliable results because the contact thermal resistance between adjacent nanowires tends to be high, which is in part due to the thin surface oxide coating which most nanowires have. This surface oxide coating may also be important for thermal conductivity measurements on individual suspended nanowires because of the relative importance of phonon scattering at the lateral walls of the nanowire.

The most extensive experimental thermal conductivity measurements have been done on Si nanowires [4.164], where $\kappa(T)$ measurements have been made on nanowires in the diameter range $22 \leq d_W \leq 115$ nm. The results show a large decrease in the peak of $\kappa(T)$, associated with Umklapp processes as d_W decreases, indicating a growing importance of boundary scattering and a corresponding decreasing im-
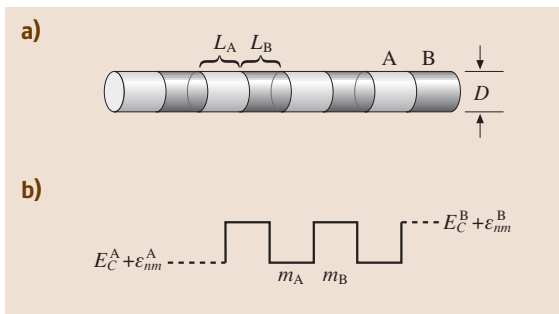
Fig. 4.31 (a) Schematic diagram of superlattice (segmented) nanowires consisting of interlaced nanodots A and B of the indicated length and wire diameter. (b) Schematic potential profile of the sub-bands in the superlattice nanowire [4.162]
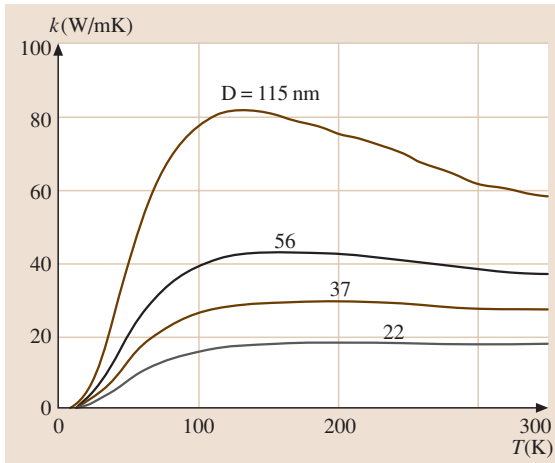
Fig. 4.33 Predicted thermal conductivities of Si nanowires of various diameters [4.169]

portance of phonon-phonon scattering. At the smallest wire diameter of 22 nm, a linear $\kappa(T)$ dependence is found experimentally, consistent with a linear T dependence of the specific heat for a 1-D system, and a temperature-independent mean free path and velocity of sound. Further insights are obtained through studies of the thermal conductivity of Si/SiGe superlattice nanowires [4.168].

Model calculations for $\kappa(T)$ based on a radiative heat transfer model have been carried out for Si nanowires [4.169]. These results show that the predicted $\kappa(T)$ behavior for Si nanowires is similar to that observed experimentally in the range of $37 \leq d_W \leq 115$ nm

regarding both the functional form of $\kappa(T)$ and the magnitude of the relative decrease in the maximum thermal conductivity κ_{max} as a function of d_W. However, the model calculations predict a substantially larger magnitude for $\kappa(T)$ (by 50% or more) than is observed experimentally. Furthermore, the model calculations (see Fig. 4.34) do not reproduce the experimentally observed linear T dependence for the 22 nm nanowires, but rather predict a 3-D behavior for both the density of states and the specific heat in 22 nm nanowires [4.169, 171, 172].

Thermal conductance measurements on GaAs nanowires below 6 K show a power law dependence, but the T dependence becomes somewhat less pronounced below ≈ 2.5 K [4.165]. This deviation from the power law temperature dependence led to a more detailed study of the quantum limit for the thermal conductance. To carry out these more detailed experiments, a mesoscopic phonon resonator and waveguide device were constructed that included four ≈ 200 nm-wide and 85 nm-thick silicon nitride nanowire-like nanoconstrictions (see Fig. 4.33a), and this was used to establish the quantized thermal conductance limit of $g_0 = \pi^2 k_B^2 T/3h$ (see Fig. 4.33b) for ballistic phonon transport [4.170, 173]. For temperatures above 0.8 K, the thermal conductance in Fig. 4.33b follows a T^3 law, but as T is further reduced, a transition to a linear T dependence is observed, consistent with a phonon mean free path of ≈ 1 μm, and a thermal conductance value approaching $16g_0$, corresponding to four massless phonon modes per channel and four channels in their phonon waveguide structure (see Fig. 4.33a). Ballistic phonon
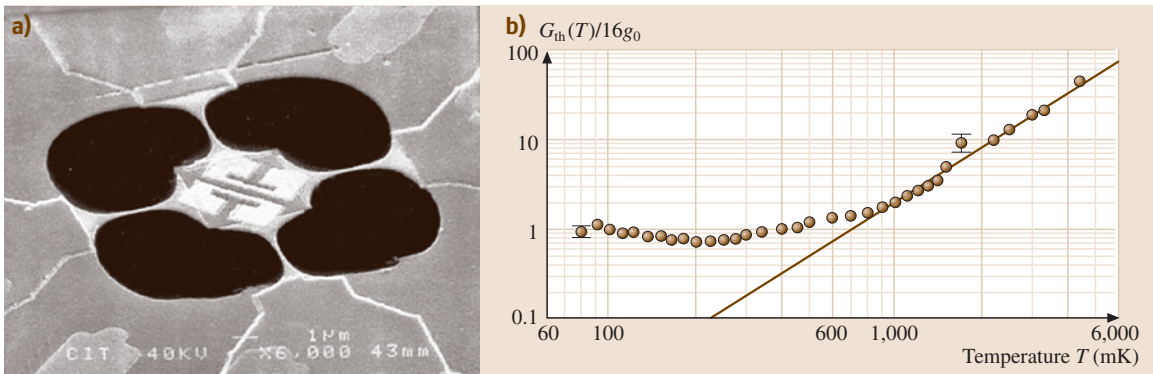
Fig. 4.34 (a) Suspended mesoscopic phonon device used to measure ballistic phonon transport. The device consists of an 4×4 μm "phonon cavity" (*center*) connected to four Si_3N_4 membranes, 60 nm thick and less than 200 nm wide. The two bright "C"-shaped objects on the phonon cavity are thin film heating and sensing Cr/Au resistors, whereas the dark regions are empty space. **(b)** Log-log plot of the temperature dependence of the thermal conductance G_0 of the structure in **(a)** normalized to $16G_0$ (see text) [4.170]

transport occurs when the thermal phonon wavelength (380 nm for the experimental structure) is somewhat greater than the width of the phonon waveguide at the waveguide constriction.

4.2.4 Optical Properties

Optical methods provide an easy and sensitive tool for measuring the electronic structures of nanowires, since optical measurements require minimal sample preparation (for example, contacts are not required) and the measurements are sensitive to quantum effects. Optical spectra of 1-D systems, such as carbon nanotubes, often show intense features at specific energies near singularities in the joint density of states that are formed under strong quantum confinement conditions. A variety of optical techniques have shown that the properties of nanowires are different to those of their bulk counterparts, and this section of the review focuses on these differences in the optical properties of nanowires.

Although optical properties have been shown to provide an extremely important tool for characterizing nanowires, the interpretation of these measurements is not always straightforward. The wavelength of light used to probe the sample is usually smaller than the wire length, but larger than the wire diameter. Hence, the probe light used in an optical measurement cannot be focused solely onto the wire, and the wire and the substrate on which the wire rests (or host material, if the wires are embedded in a template) are probed simultaneously. For measurements, such as photoluminescence (PL), if the substrate does not luminescence or absorb in the frequency range of the measurements, PL measures the luminescence of the nanowires directly and the substrate can be ignored. However, in reflection and transmission measurements, even a non-absorbing substrate can modify the measured spectra of nanowires.

In this section we discuss the determination of the dielectric function for nanowires in the context of effective medium theories. We then discuss various optical techniques with appropriate examples that sensitively differentiate nanowire properties from those also found in the parent bulk material, placing particular emphasis on electronic quantum confinement effects. Finally, phonon confinement effects are reviewed.

The Dielectric Function

In this subsection, we review the use of effective medium theory as a method to handle the optical properties of nanowires whose diameters are typically smaller than the wavelength of light, noting that observable optical properties of materials can be related to the complex dielectric function [4.174, 175]. Effective medium theories [4.176, 177] can be applied to model the nanowire and substrate as one continuous composite with a single complex dielectric function ($\epsilon_1 + i\epsilon_2$), where the real and imaginary parts of the dielectric function ϵ_1 and ϵ_2 are related to the index of refraction (n) and the absorption coefficient (K) by the relation $\epsilon_1 + i\epsilon_2 = (n + iK)^2$. Since photons at visible or infrared wavelengths "see" a dielectric function for the composite nanowire array/substrate system that is different from that of the nanowire itself, the optical transmission and reflection are different from what they would be if the light were focused only on the nanowire. One commonly observed consequence of effective medium theory is the shift in the plasma frequency in accordance with the percentage of nanowire material that is contained in the composite [4.178]. The plasma resonance occurs when $\epsilon_1(\omega)$ becomes zero, and the plasma frequency of the nanowire composite will shift to lower (higher) energies when the magnitude of the dielectric function of the host materials is larger (smaller) than that of the nanowire.

Although reflection and transmission measurements probe both the nanowire and the substrate, the optical properties of the nanowires can be determined independently. One technique for separating out the dielectric function of the nanowires from the host is to use an effective medium theory in reverse. Since the dielectric function of the host material is often known, and the dielectric function of the composite material can be measured by the standard method of using reflection and transmission measurements in combination with either the Kramer–Kronig relations or Maxwell's equations, the complex dielectric function of the nanowires can be deduced. An example where this approach has been used successfully is for the determination of the frequency dependence of the real and imaginary parts of the dielectric function $\epsilon_1(\omega)$ and $\epsilon_2(\omega)$ for a parallel array of bismuth nanowires filling the pores of an alumina template [4.179].

Characteristic Optical Properties of Nanowires

A wide range of optical techniques are available for the characterization of nanowires, to distinguish their properties from those of their parent bulk materials. Some differences in properties relate to geometric differences, such as the small diameter size and the large length-to-diameter ratio (also called the aspect ratio), while others focus on quantum confinement issues.

Probably the most basic optical technique is to measure the reflection and/or transmission of a nanowire to

determine the frequency- dependent real and imaginary parts of the dielectric function. This technique has been used, for example, to study the band gap and its temperature dependence in gallium nitride nanowires in the 10–50 nm range in comparison to bulk values [4.180]. The plasma frequency, free carrier density, and donor impurity concentration as a function of temperature were also determined from the infrared spectra, which is especially useful for nanowire research, since Hall effect measurements cannot be made on nanowires.

Another common method used to study nanowires is photoluminescence (PL) or fluorescence spectroscopy. Emission techniques probe the nanowires directly and the effect of the host material does not have to be considered. This characterization method has been used to study many properties of nanowires, such as the optical gap behavior, oxygen vacancies in ZnO nanowires [4.55], strain in Si nanowires [4.181], and quantum confinement effects in InP nanowires [4.182]. Figure 4.35 shows the photoluminescence of InP nanowires as a function of wire diameter, thereby providing direct information on the effective bandgap. As the wire diameter of an InP nanowire is decreased so that it becomes smaller than the bulk exciton diameter of 19 nm, quantum confinement effects set in, and the band gap is increased. This results in an increase in the PL peak energy. The smaller the effective mass, the larger the quantum confinement effects. When the shift in the peak energy as a function of nanowire diameter Fig. 4.35 is analyzed using an effective mass model, the reduced effective mass of the exciton is deduced to be $0.052\,m_0$, which agrees quite well with the literature value of $0.065\,m_0$ for bulk InP. Although the linewidths of the PL peak for the small-diameter nanowires (10 nm) are smaller at low temperature (7 K), the observation of strong quantum confinement and bandgap tunability effects at room temperature are significant for photonics applications of nanowires (see Sect. 4.3.3).

The resolution of photoluminescence (PL) optical imaging of a nanowire is, in general, limited by the wavelength of light. However, when a sample is placed very close to the detector, the light is not given a chance to diffract, and so samples much smaller than the wavelength of light can be resolved. This technique is known as near-field scanning optical microscopy (NSOM) and has been used to successfully image nanowires [4.183]. For example, Fig. 4.36 shows the topographical (a) and (b) NSOM PL images of a single ZnO nanowire.

Magneto-optics can be used to measure the electronic band structure of nanowires. For example, magneto-optics in conjunction with photoconductance has been proposed as a tool to determine band parameters for nanowires, such as the Fermi energy, electron effective masses, and the number of sub-bands to be considered [4.184]. Since different nanowire sub-bands have different electrical transmission properties, the electrical conductivity changes when light is used to excite electrons to higher subbands, thereby providing a method for studying the electronic structure of nanowires optically. Magneto-optics can also be used to study the magnetic properties of nanowires in relation to bulk properties [4.27, 185]. For example, the surface magneto-optical Kerr effect has been used to measure the dependence of the magnetic ordering temperature of Fe–Co alloy nanowires on the relative concentration of Fe and Co [4.185], and it was used to find that, unlike in the case of bulk Fe–Co alloys, cobalt in nanowires inhibits magnetic ordering. Nickel nanowires were found to have a strong increase in their magneto-optical activity with respect to bulk nickel. This increase is attributed to the plasmon resonance in the wires [4.186].

Nonlinear optical properties of nanowires have received particular attention since the nonlinear behavior is often enhanced compared to bulk materials and the nonlinear effects can be utilized for many applications. One such study measured the second harmonic generation (SHG) and third harmonic generation (THG) in a single nanowire using near-field optical microscopy [4.187]. ZnO nanowires were shown to have strong SHG and THG effects that are highly polarization-sensitive, and this polarization sensitivity can be explained on the basis of optical and geometrical considerations. Some components of the second harmonic polarization tensor are found to be enhanced in nanowires while others are suppressed as the wire diameter is decreased, and such effects could be of interest for device applications. The authors also showed that the second-order nonlinearities are mostly wavelength-independent for $\lambda < 400$ nm, which is in the transparent regime for ZnO, below the onset of band gap absorption, and this observation is also of interest for device applications.

Reflectivity and transmission measurements have also been used to study the effects of quantum confinement and surface effects on the low-energy indirect transition in bismuth nanowires [4.188]. *Black* et al. investigated an intense and sharp absorption peak in bismuth nanowires, which is not observed in bulk bismuth. The energy position E_p of this strong absorption peak increases with decreasing diameter. However, the rate of increase in energy with decreasing diameter $|\partial E_p / \partial d_W|$ is an order of magnitude less than that predicted for either a direct interband transition or for intersub-band
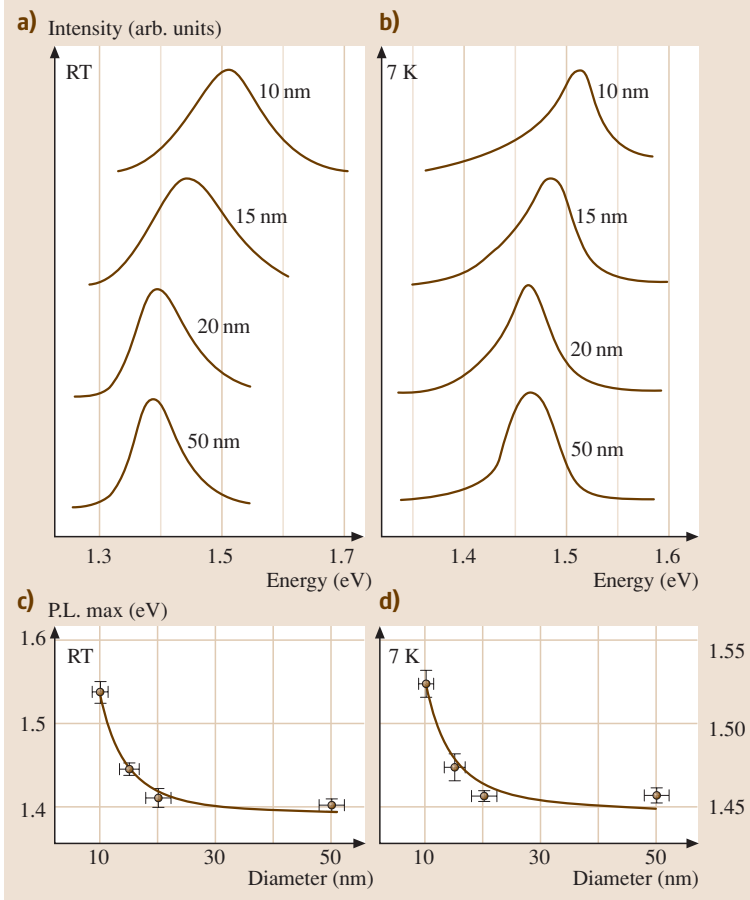
Fig. 4.35a–d Photo-luminescence of InP nanowires of varying diameters at 7 K ((**b**) and (**d**)) and room temperature ((**a**) and (**c**)) showing quantum confinement effects of the exciton for wire diameters of less than 20 nm [4.182]
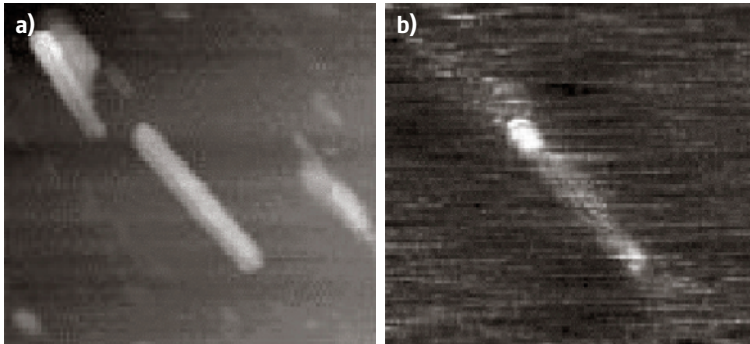
Fig. 4.36 (**a**) Topographical and (**b**) photoluminescence (PL) near-field scanning optical microscopy (NSOM) images of a single ZnO nanowire waveguide [4.183]

transitions in bismuth nanowires. On the other hand, the magnitude of $|\partial E_p / \partial d_W|$ agrees well with that predicted for an indirect L-point valence to T-point valence band transition (see Fig. 4.37). Since both the initial and final states for the indirect $L-T$ point valence band transition downshift in energy as the wire diameter d_W is decreased, the shift in the absorption peak results from a difference between the effective masses and not from the actual value of either of the masses. Hence the diameter dependence of the absorption peak energy is an order of magnitude less for a valence to valence band indirect transition than for a direct interband L-point transition.

Furthermore, the band-tracking effect for the indirect transition gives rise to a large value for the joint density of states, thus accounting for the high intensity of this feature. The enhancement in the absorption resulting from this indirect transition may arise from a gradient in the dielectric function, which is large at the bismuth–air or bismuth–alumina interfaces, or from the relaxation of momentum conservation rules in nanosystems. It should be noted that, in contrast to the surface effect for bulk samples, the whole nanowire contributes to the optical absorption due to the spatial variation in the dielectric function, since the penetration depth is larger than or comparable to the wire diameter. In addition, the intensity can be quite significant because there are abundant initial state electrons, final state holes, and appropriate phonons for making an indirect $L–T$ point valence band transition at room temperature. Interestingly, the polarization dependence of this absorption peak is such that the strong absorption is present when the electric field is perpendicular to the wire axis, but is absent when the electric field is parallel to the wire axis, contrary to a traditional polarizer, such as a carbon nanotube where the optical E field is polarized by the nanotube itself and is aligned along the carbon nanotube axis. The observed polarization dependence for bismuth nanowires is consistent with a surface-induced effect that increases the coupling between the L-point and T-point bands throughout the full volume of the nanowire. Figure 4.37 shows the experimentally observed transmission spectrum in bismuth nanowires of ≈ 45 nm diameter (a), and the simulated optical transmission from an indirect transition in bismuth nanowires of ≈ 45 nm diameter is also shown for comparison in (b). The indirect $L–T$ point valence band transition mechanism [4.189] is also consistent with observations of the effect on the optical spectra of a decrease in the nanowire diameter and of n-type doping of bismuth nanowires with Te.

Phonon Confinement Effects

Phonons in nanowires are spatially confined by the nanowire cross-sectional area, crystalline boundaries and surface disorder. These finite size effects give rise to phonon confinement, causing an uncertainty in the phonon wavevector which typically gives rise to a frequency shift and lineshape broadening. Since zone center phonons tend to correspond to maxima in the
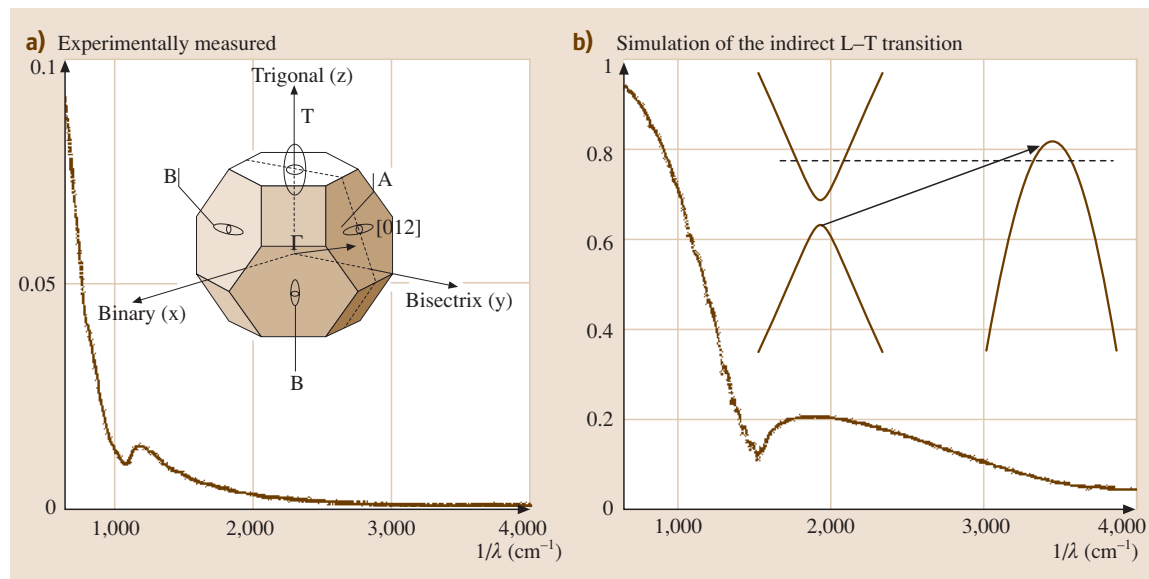
Fig. 4.37 (a) The measured optical transmission spectra as a function of wavenumber ($1/\lambda$) of a ≈ 45 nm-diameter bismuth nanowire array. **(b)** The simulated optical transmission spectrum resulting from an indirect transition of an L point electron to a T point valence sub-band state. The *insert* in **(a)** shows the bismuth Brillouin zone, and the locations of the T-point hole and the three L-point electron pockets, including the nondegenerate A, and the doubly-degenerate B pockets. The *insert* in **(b)** shows the indirect L to T point electronic transition induced by a photon with an energy equal to the energy difference between the initial and final states minus the phonon energy (about $100\,\mathrm{cm}^{-1}$) needed to satisfy conservation of energy in a Stokes process [4.189]

phonon dispersion curves, the inclusion of contributions from a broader range of phonon wave vectors results in both a downshift in frequency and an asymmetric broadening of the Raman line, which develops a low frequency tail. These phonon confinement effects have been theoretically predicted [4.190, 191] and experimentally observed in GaN [4.192], as shown in Fig. 4.38 for GaN nanowires with diameters in the range 10–50 nm. The application of these theoretical models indicates that broadening effects should be noticeable as the wire diameter in GaN nanowires decreases to ≈ 20 nm. When the wire diameter decreases further to ≈ 10 nm, the frequency downshift and asymmetric Raman line broadening effects should become observable in the Raman spectra for the GaN nanowires but are not found in the corresponding spectra for bulk GaN.

The experimental spectra in Fig. 4.38 show the four $A_1 + E_1 + 2E_2$ modes expected from symmetry considerations for bulk GaN crystals. Two types of quantum confinement effects are observed. The first type is the observation of the downshift and the asymmetric broadening effects discussed above. Observations of such downshifts and asymmetric broadening have also been recently reported in 7 nm diameter Si nanowires [4.193]. A second type of confinement effect found in Fig. 4.38 for GaN nanowires is the appearance of additional Raman features not found in the corresponding bulk spectra and associated with combination modes, and a zone boundary mode. Resonant enhancement effects
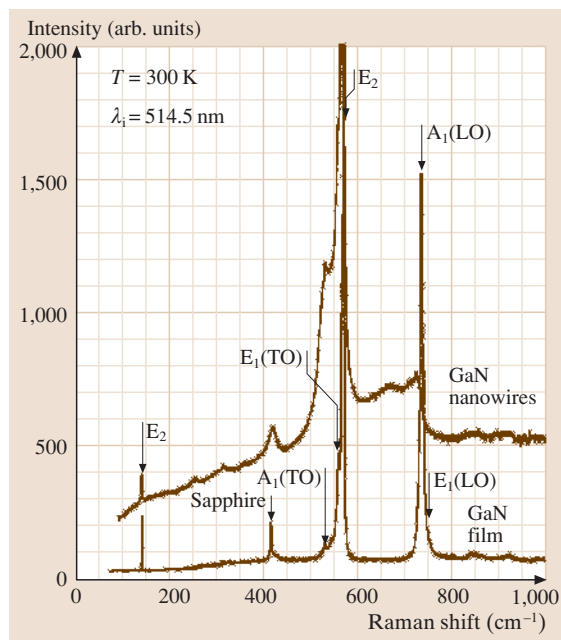

Fig. 4.38 Room-temperature Raman scattering spectra of GaN nanowires and of a 5 μm thick GaN epilayer film with green (514.5 nm) laser excitation. The Raman scattering response was obtained by dividing the measured spectra by the Bose–Einstein thermal factor [4.192]

were also observed for the $A_1(LO)$ phonon at $728\,\mathrm{cm}^{-1}$ (see Fig. 4.38) at higher laser excitation energies [4.192].

4.3 Applications

In the preceding sections we have reviewed many of the central characteristics that make nanowires in some cases similar to and in some cases very different from their parent materials. We have also shown that some properties are diameter-dependent, and these properties are therefore tunable during synthesis. Thus, it is of great interest to find applications that could benefit in unprecedented ways from both the unique and tunable properties of nanowires and the small sizes of these nanostructures, especially in the miniaturization of conventional devices. As the synthetic methods for the production of nanowires are maturing (Sect. 4.1) and nanowires can be made in reproducible and cost-effective ways, it is only a matter of time before applications will be seriously explored. This is a timely development, as the semiconductor industry will soon be reaching what seems

to be its limit in feature size reduction, and approaching a classical-to-quantum size transition. At the same time, the field of biotechnology is expanding through the availability of tremendous genome information and innovative screening assays. Since nanowires are similar in size to the shrinking electronic components and to cellular biomolecules, it is only natural for nanowires to be good candidates for applications in these fields. Commercialization of nanowire devices, however, will require reliable mass production, effective assembly techniques and quality control methods.

In this section, applications of nanowires to electronics (Sect. 4.3.1), thermoelectrics (Sect. 4.3.2), optics (Sect. 4.3.3), chemical and biochemical sensing (Sect. 4.3.4), and magnetic media (Sect. 4.3.5) are discussed.

4.3.1 Electrical Applications

The microelectronics industry continues to face technological (in lithography for example) and economic challenges as the device feature size is decreased, especially below 100 nm. The self-assembly of nanowires might present a way to construct unconventional devices that do not rely on improvements in photolithography and, therefore, do not necessarily imply increasing fabrication costs. Devices made from nanowires have several advantages over those made by photolithography. A variety of approaches have been devised to organize nanowires via self-assembly (see Sect. 4.1.4), thus eliminating the need for the expensive lithographic techniques normally required to produce devices the size of typical nanowires that are discussed in this review. In addition, unlike traditional silicon processing, different semiconductors can be used simultaneously in nanowire devices to produce diverse functionalities. Not only can wires of different materials be combined, but a single wire can be made of different materials. For example, junctions of GaAs and GaP show rectifying behavior [4.92], thus demonstrating that good electronic interfaces between two different semiconductors can be achieved in the synthesis of multicomponent nanowires. Transistors made from nanowires could also hold advantages due to their unique morphology. For example, in bulk field effect transistors (FETs), the depletion layer formed below the source and drain region results in a source–drain capacitance which limits the operation speed. However, in nanowires, the conductor is surrounded by an oxide and thus the depletion layer cannot be formed. Thus, depending on the device design, the source–drain capacitance in nanowires could be greatly minimized and possibly eliminated.

Device functionalities common in conventional semiconductor technologies, such as p-n junction diodes [4.142], field-effect transistors [4.144], logic gates [4.142], and light-emitting diodes [4.92, 194], have been recently demonstrated in nanowires, showing their promise as building blocks that could be used to construct complex integrated circuits by employing the "bottom-up" paradigm. Several approaches have been investigated to form nanowire diodes (see Sect. 4.2.2). For example, Schottky diodes can be formed by contacting a GaN nanowire with Al electrodes [4.143]. Furthermore, p-n junction diodes can be formed at the crossing of two nanowires, such as the crossing of n- and p-type InP nanowires doped by Te and Zn, respectively [4.194], or Si nanowires doped by phosphorus (n-type) and boron (p-type) [4.195]. In addition to the

crossing of two distinctive nanowires, heterogeneous junctions have also been constructed inside a single wire, either along the wire axis in the form of a nanowire superlattice [4.92], or perpendicular to the wire axis by forming a core–shell structure of silicon and germanium [4.111]. These various nanowire junctions not only possess the current rectifying properties (see Fig. 4.22) expected of bulk semiconductor devices, but they also exhibit electroluminescence (EL) that may be interesting for optoelectronic applications, as shown in Fig. 4.39 for the electroluminescence of a crossed junction of n- and p-type InP nanowires [4.194] (see Sect. 4.3.3).

In addition to the two-terminal nanowire devices, such as the p-n junctions described above, it is found that the conductance of a semiconductor nanowire can be significantly modified by applying voltage at a third gate terminal, implying the utilization of nanowires in field effect transistors (FETs). This gate terminal can either be the substrate [4.30, 196–199], a separate metal contact located close to the nanowire [4.200], or another nanowire with a thick oxide coating in the crossed nanowire junction configuration [4.142]. The operating principles of these nanowire-based FETs are discussed in Sect. 4.2.2. Various logic devices performing basic logic functions have been demonstrated using nanowire junctions [4.142], as shown in Fig. 4.40 for the OR and AND logic gates constructed from 2-by-1 and 1-by-3 nanowire p-n junctions, respectively. By functionalizing nanowires with redox-active molecules to store charge, nanowire FETs were demonstrated with two-level [4.144] and with eight-level [4.201] memory effects, which may be used for nonvolatile memory or as switches. In another advance, In_2O_3 nanowire FETs with high-k dielectric material were demonstrated, and substantially enhanced performance was obtained due to the highly efficient coupling of the gate [4.202]. A vertical FET with a surrounding gate geometry has also been demonstrated, which has the potential for high-density nanoscale memory and logic devices [4.203].

Nanowires have also been proposed for applications associated with electron field emission [4.204], such as flat panel displays, because of their small diameter and large curvature at the nanowire tip, which may reduce the threshold voltage for electron emission [4.205]. In this regard, the demonstration of very high field emission currents from the sharp tip ($\approx 10\,nm$ radius) of a Si cone [4.204], from carbon nanotubes [4.206], from Si nanowires inside a carbon nanotube [4.207], and from Co nanowires [4.208], has stimulated interest in this potential area of application for nanowires.

The concept of constructing electronic devices based on nanowires has already been demonstrated, and the next step for electronic applications would be to devise a feasible method for integration and mass production. We expect that, in order to maintain the growing rate of device density and functionality in the existing electronic industry, new kinds of complementary electronic devices will emerge from this "bottom-up" scheme for nanowire electronics, different from what has been produced by the traditional "top-down" approach pursued by conventional electronics.

4.3.2 Thermoelectric Applications

One proposed application for nanowires is for thermoelectric cooling and for the conversion between thermal and electrical energy [4.171, 209]. The efficiency of a thermoelectric device is measured in terms of a dimensionless figure of merit ZT, where Z is defined as

$$Z = \frac{\sigma S^2}{\kappa}, \qquad (4.2)$$

where σ is the electrical conductivity, S is the Seebeck coefficient, κ is the thermal conductivity, and T is the temperature. In order to achieve a high ZT and therefore efficient thermoelectric performance, a high electrical conductivity, a hugh Seebeck coefficient and
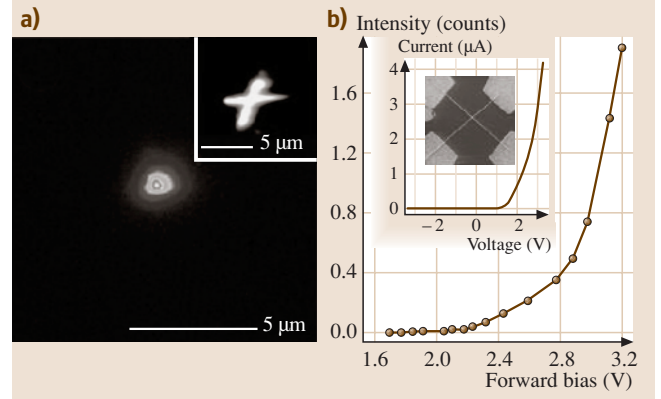

Fig. 4.39a,b Optoelectrical characterization of a crossed nanowire junction formed between 65 nm n-type and 68 nm p-type InP nanowires. (**a**) Electroluminescence (EL) image of the light emitted from a forward-biased nanowire p-n junction at 2.5 V. *Inset*, photoluminescence (PL) image of the junction. (**b**) EL intensity as a function of operation voltage. *Inset*, the SEM image and the I–V characteristics of the junction [4.194]. The scale bar in the inset is 5 μm

a low thermal conductivity are required. In 3-D systems, the electronic contribution to κ is proportional to σ in accordance with the Wiedemann–Franz law, and normally materials with high S have a low σ. Hence an increase in the electrical conductivity (for example by
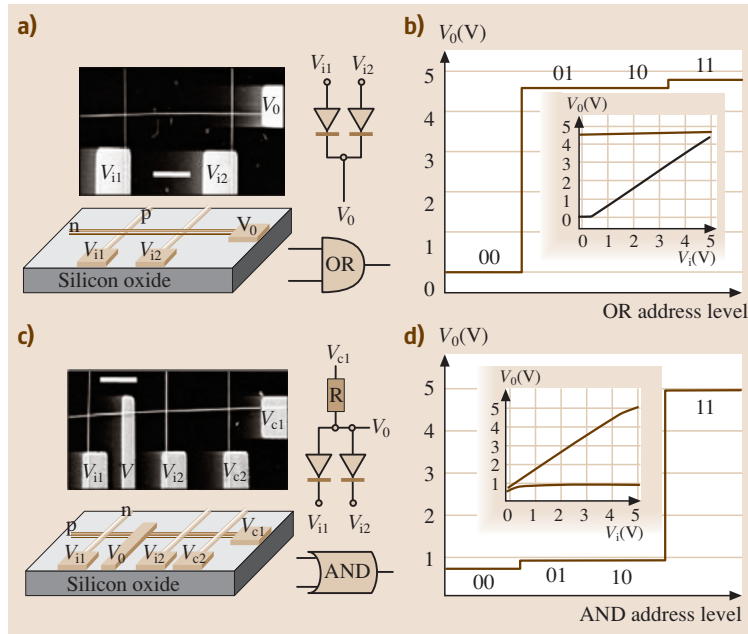
Fig. 4.40a–d Nanowire logic gates: (**a**) Schematic of logic OR gate constructed from a 2(p-Si) by 1(n-GaN) crossed nanowire junction. The *inset* shows the SEM image (bar: 1 μm) of an assembled OR gate and the symbolic electronic circuit. (**b**) The output voltage of the circuit in (**a**) versus the four possible logic address level inputs: (0,0); (0,1); (1,0); (1,1), where logic 0 input is 0 V and logic 1 is 5 V (same for below). (**c**) Schematic of logic AND gate constructed from a 1(p-Si) by 3(n-GaN) crossed nanowire junction. The *inset* shows the SEM image (bar: 1 μm) of an assembled AND gate and the symbolic electronic circuit. (**d**) The output voltage of the circuit in (c) versus the four possible logic address level inputs [4.142]

electron donor doping) results in an adverse variation in both the Seebeck coefficient (decreasing) and the thermal conductivity (increasing). These two trade-offs set the upper limit for increasing ZT in bulk materials, with the maximum ZT remaining ≈ 1 at room temperature for the 1960–1995 time frame.

The high electronic density of states in quantum-confined structures is proposed as a promising possibility to bypass the Seebeck/electrical conductivity trade-off and to control each thermoelectric-related variable independently, thereby allowing for increased electrical conductivity, relatively low thermal conductivity, and a large Seebeck coefficient simultaneously [4.211]. For example, Figs. 4.29 and 4.30a in Sect. 4.2.3 show an enhanced in S for bismuth and bismuth-antimony nanowires as the wire diameter decreases. In addition to alleviating the undesired connections between σ, S and the electronic contribution to the thermal conductivity, nanowires also have the advantage that the phonon contribution to the thermal conductivity is greatly reduced because of boundary scattering (see Sect. 4.2), thereby achieving a high ZT. Figure 4.41a shows the theoretical values for ZT versus sample size for both bismuth thin films (2-D) and nanowires (1-D) in the quantum-confined regime, exhibiting a rapidly increasing ZT as the quantum size effect becomes more and more important [4.211]. In addition, the quantum size effect in nanowires can be combined with other parameters to tailor the band structure and electronic transport behav-

ior (for instance, Sb alloying in Bi) to further optimize ZT. For example, Fig. 4.41b shows the predicted ZT for p-type $Bi_{1-x}Sb_x$ alloy nanowires as a function of wire diameter and Sb content x [4.210]. The occurrence of a local ZT maxima in the vicinity of $x \approx 0.13$ and $d_W \approx 45$ nm is due to the coalescence of ten valence bands in the nanowire and the resulting unusual high density of states for holes, which is a phenomenon absent in bulk $Bi_{1-x}Sb_x$ alloys. For nanowires with very small diameters, it is speculated that localization effects will eventually limit the enhancement of ZT. However, in bismuth nanowires, localization effects are not significant for wires with diameters larger than 9 nm [4.52]. In addition to 1-D nanowires, ZT values as high as ≈ 2 have also been experimentally demonstrated in macroscopic samples containing PbSe quantum dots (0D) [4.212] and stacked 2-D films [4.167].

Although the application of nanowires to thermoelectrics appears promising, these materials are still in the research phase of the development cycle and are far from being commercialized. One challenge for thermoelectric devices based on nanowires lies in finding a suitable host material that will not reduce ZT too much due to the unwanted heat conduction through the host material. Therefore, the host material should have a low thermal conductivity and occupy a volume percentage in the composite material that is as low as possible, while still providing the quantum confinement and the support for the nanowires.
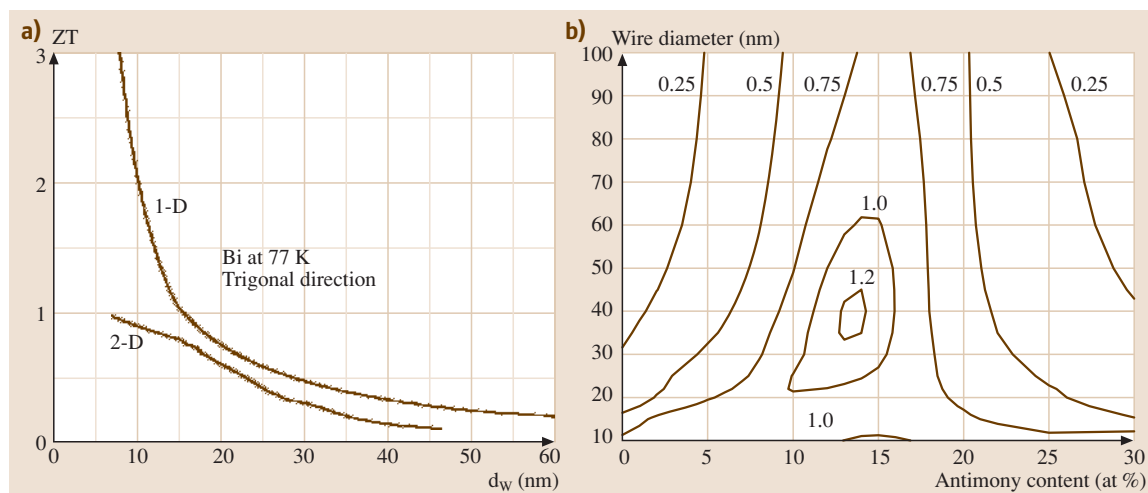
Fig. 4.41 **(a)** Calculated ZT of 1-D (nanowire) and 2-D (quantum well) bismuth systems at 77 K as a function of d_W, denoting the wire diameter or film thickness. The thermoelectric performance (ZT) is expected to improve greatly when the wire diameter is small enough for the nanowire to become a one-dimensional system. **(b)** Contour plot of optimal ZT values for p-type $Bi_{1-x}Sb_x$ nanowires versus wire diameter and antimony concentration calculated at 77 K [4.210]

4.3.3 Optical Applications

Nanowires also hold promise for optical applications. One-dimensional systems exhibit a singularity in their joint density of states, allowing quantum effects in nanowires to be optically observable, sometimes even at room temperature. Since the density of states of a nanowire in the quantum limit (small wire diameter) is highly localized in energy, the available states quickly fill up with electrons as the intensity of the incident light is increased. This filling up of the sub-bands, as well as other effects that are unique to low-dimensional materials, lead to strong optical non-linearities in quantum wires. Quantum wires may thus yield optical switches with a lower switching energy and increased switching speed compared to currently available optical switches.

Light emission from nanowires can be achieved by photoluminescence (PL) or electroluminescence (EL), distinguished by whether the electronic excitation is achieved by optical illumination or by electrical stimulation across a p-n junction, respectively. PL is often used for optical property characterization, as described in Sect. 4.2.4, but from an applications point of view, EL is a more convenient excitation method. Light-emitting diodes (LEDs) have been achieved in junctions between a p-type and an n-type nanowire (Fig. 4.39) [4.194] and in superlattice nanowires with p-type and n-type segments [4.92]. The light emission was localized to the junction area, and was polarized in the superlattice nanowire. An electrically driven laser was fabricated from CdS nanowires. The wires were assembled by evaporating a metal contact onto an n-type CdS nanowire which resided on a p^+ silicon wafer. The cleaved ends of the wire formed the laser cavity, so that in forward bias, light characteristic of lasing was observed at the end of the wire [4.213]. LEDs have also been achieved with core–shell structured nanowires made of n-GaN/InGaN/p-GaN [4.214].

Light emission from quantum wire p-n junctions is especially interesting for laser applications, because quantum wires can form lasers with lower excitation thresholds than their bulk counterparts and they also exhibit decreased sensitivity of performance to temperature [4.215]. Furthermore, the emission wavelength can be tuned for a given material composition by simply altering the geometry of the wire.

Lasing action has been reported in ZnO nanowires with wire diameters that are much smaller than the wavelength of the light emitted ($\lambda = 385$ nm) [4.122] (see Fig. 4.42). Since the edges and lateral surfaces of

ZnO nanowires are faceted (see Sect. 4.2.1), they form optical cavities that sustain desired cavity modes. Compared to conventional semiconductor lasers, the exciton laser action employed in zinc oxide nanowire lasers exhibits a lower lasing threshold (≈ 40 kW/cm^2) than their 3-D counterparts (≈ 300 kW/cm^2). In order to utilize exciton confinement effects in the lasing action, the exciton binding energy (≈ 60 meV in ZnO) must be greater than the thermal energy (≈ 26 meV at 300 K). Decreasing the wire diameter increases the excitation binding energy and lowers the threshold for lasing. PL NSOM imaging confirmed the waveguiding properties of the anisotropic and the well-faceted structure of ZnO nanowires, limiting the emission to the tips of the ZnO nanowires [4.183]. Time-resolved studies have illuminated the dynamics of the emission process [4.216].
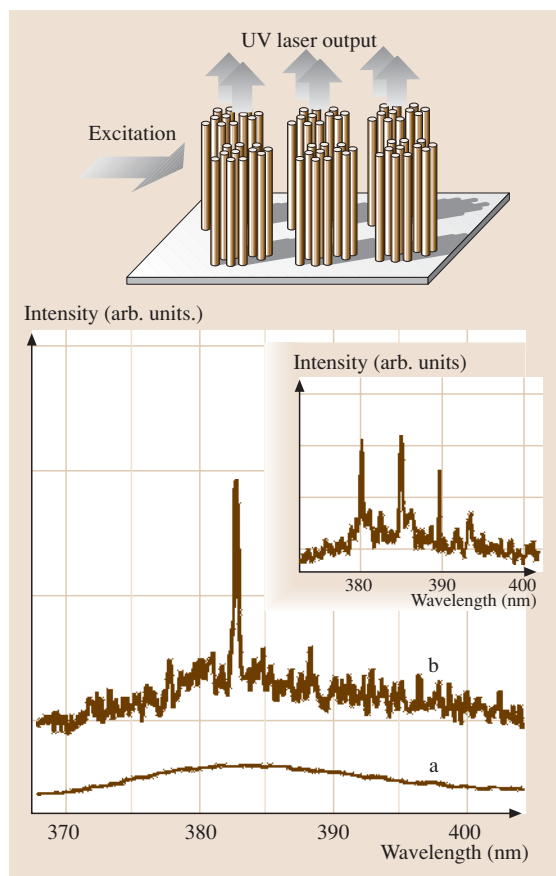

Fig. 4.42 A schematic of lasing in ZnO nanowires and the PL spectra of ZnO nanowires at two excitation intensities. One PL spectrum is taken below the lasing threshold, and the other above it [4.122]

Lasing was also observed in ZnS nanowires in anodic aluminium oxide templates [4.217] and in GaN nanowires [4.218]. Unlike ZnO, GaN has a small exciton binding energy, only ≈ 25 meV. Furthermore, since the wire radii used in this study (15–75 nm) [4.218] are larger than the Bohr radius of excitons in GaN (11 nm), the exciton binding energy is not expected to increase in these GaN wires and quantum confinement effects such as those shown in Fig. 4.35 for InP are not expected. However, some tunability of the center of the spectral intensity was achieved by increasing the intensity of the pump power, causing a redshift in the laser emission, which is explained as a bandgap renormalization as a result of the formation of an electron–hole plasma. Heating effects were excluded as the source of the spectral shift. GaN quantum wire UV lasers with a low threshold for lasing action have been achieved using a self-organized GaN(core)/AlGaN(shell) structure [4.219].

Nanowires have also been demonstrated to have good waveguiding properties. Quantitative studies of cadmium sulfide (CdS) nanowire structures show that light propagation takes place with only moderate losses through sharp and even acute angle bends. In addition, active devices made with nanowires have shown that efficient injection into and modulation of light through nanowire waveguides can be achieved [4.220]. By linking ZnO nanowire light sources to SnO_2 waveguides, the possibility of optical integrated circuitry is introduced [4.221].

Nanowire photodetectors were also proposed. ZnO nanowires were found to display a strong photocurrent response to UV light irradiation [4.222]. The conductivity of the nanowire increased by four orders of magnitude compared to the dark state. The response of the nanowire was reversible, and selective to photon energies above the bandgap, suggesting that ZnO nanowires could be a good candidate for optoelectronic switches.

Nanowires have been also proposed for another type of optical switching. Light with its electric field normal to the wire axis excites a transverse free carrier resonance inside the wire, while light with its electric field parallel to the wire axis excites a longitudinal free carrier resonance inside the wire. Since nanowires are highly anisotropic, these two resonances occur at two different wavelengths and thus result in absorption peaks at two different energies. Gold nanowires dispersed in an aqueous solution align along the electric field when a DC voltage is applied. The energy of the absorption peak can be toggled between the transverse and longitudinal resonance energies by changing the alignment of the nanowires under polarized light illumination us-

ing an electric field [4.223, 224]. Thus, electro-optical modulation is achieved.

Nanowires may also be used as barcode tags for optical read-out. Nanowires containing gold, silver, nickel, palladium, and platinum were fabricated [4.110] by electrochemical filling of porous anodic alumina, so that each nanowire consisted of segments of various metal constituents. Thus many types of nanowires can be made from a handful of materials, and identified by the order of the metal segments along their main axis, and the length of each segment. Barcode read-out is possible by reflectance optical microscopy. The segment length is limited by the Rayleigh diffraction limit, and not by synthesis limitations, and thus can be as small as 145 nm. Figure 4.43a shows an optical image of many Au-Ag-Au-Ag barcoded wires, where the silver segments show higher reflectivity. Figure 4.43b is a backscattering mode FE-SEM image of a single nanowire, highlighting the composition and segment length variations along the nanowire.

Both the large surface area and the high conductivity along the length of a nanowire are favorable for its use in inorganic–organic solar cells [4.225], which offer promise from a manufacturing and cost-effectiveness standpoint. In a hybrid nanocrystal–organic solar cell, the incident light forms bound electron–hole pairs (excitons) in both the inorganic nanocrystal and in the surrounding organic medium. These excitons diffuse to the inorganic–organic interface and disassociate to form an electron and a hole. Since conjugated polymers usually have poor electron mobilities, the inorganic phase is chosen to have a higher electron affinity than the organic phase so that the organic phase carries the holes and the semiconductor carries the electrons. The separated electrons and holes drift to the external electrodes through the inorganic and organic materials, respectively. However, only those excitons formed within an exciton diffusion length from an interface can disassociate before recombining, and therefore the distance between the dissociation sites limits the efficiency of a solar cell. A solar cell prepared from a composite of CdSe nanorods inside poly(3-ethylthiophene) [4.225] yielded monochromatic power efficiencies of 6.9% and power conversion efficiencies of 1.7% under A.M. 1.5 illumination (equal to solar irradiance through 1.5 times the air mass of the Earth at direct normal incidence). The nanorods provide a large surface area with good chemical bonding to the polymer for efficient charge transfer and exciton dissociation. Furthermore, they provide a good conduction path for the electrons to reach the electrode. Their enhanced absorption coefficient and
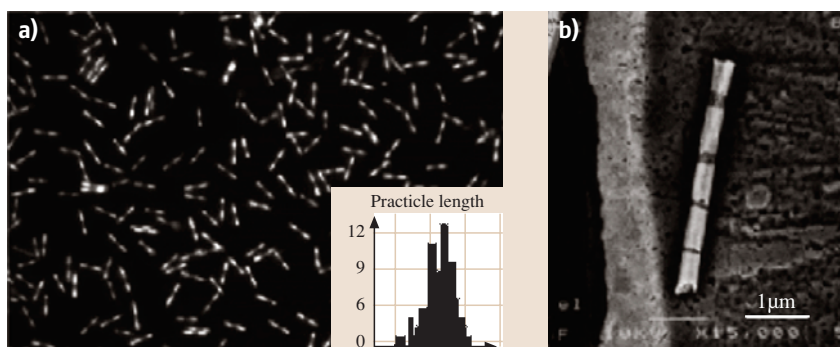
Fig. 4.43 **(a)** An optical image of many short bar-coded Au-Ag-Au-Au wires and **(b)** an FE-SEM image of an Au/Ag barcoded wire with multiple strips of varying length. The *insert* in **(a)** shows a histogram of the particle lengths for 106 particles in this image [4.110]

their tunable bandgap are also characteristics that can be used to enhance the energy conversion efficiency of solar cells.

4.3.4 Chemical and Biochemical Sensing Devices

Sensors for chemical and biochemical substances with nanowires as the sensing probe are a very attractive application area. Nanowire sensors will potentially be smaller, more sensitive, demand less power, and react faster than their macroscopic counterparts. Arrays of nanowire sensors could, in principle, achieve nanometer-scale spatial resolution and therefore provide accurate real-time information regarding not only the concentration of a specific analyte but also its spatial distribution. Such arrays could be very useful, for example, for dynamic studies on the effects of chemical gradients on biological cells. The operation of sensors made with nanowires, nanotubes, or nanocontacts is based mostly on the reversible change in the conductance of the nanostructure upon absorption of the agent to be detected, but other detection methods, such as mechanical and optical detection, are conceptually plausible. The increased sensitivity and faster response time of nanowires are a result of the large surface-to-volume ratio and the small cross-section available for conduction channels. In the bulk, on the other hand, the abundance of charges can effectively shield external fields, and the abundance of material can afford many alternative conduction channels. Therefore, a stronger chemical stimulus and longer response time are necessary to observe changes in the physical properties of a 3-D sensor in comparison to a nanowire.

It is often necessary to modify the surface of the nanowires to achieve a strong interaction with the analytes that need to be detected. Surface modifications utilize the self-assembly, chemisorption or chemical reactivity of selected organic molecules and polymers towards metal and oxide surfaces. Examples include: thiols on gold, isocyanides on platinum, and siloxanes on silica. These surface coatings regulate the binding and chemical reactivity of other molecules towards the nanowire in a predictable manner [4.226].

Cui et al. placed silicon nanowires made by the VLS method (Sect. 4.1.2) between two metal electrodes and modified the silicon oxide coating of the wire through the addition of molecules that are sensitive to the analyte to be detected [4.227]. For example, a pH sensor was made by covalently linking an amine-containing silane to the surface of the nanowire. Variations in the pH of the solution into which the nanowire was immersed caused protonation and deprotonation of the $-NH_2$ and the $-SiOH$ groups on the surface of the nanowire. The variation in surface charge density regulates the conductance of the nanowire; due to the p-type characteristics of a silicon wire, the conductance increases with the addition of negative surface charge. The combined acid and base behavior of the surface groups results in an approximately linear dependence of the conductance on pH in the pH range 2 to 9, thus leading to a direct readout pH meter. This same type of approach was used for the detection of the binding of biomolecules, such as streptavidin using biotin-modified nanowires (see Fig. 4.44). This nanowire-based device has high sensitivity and could detect streptavidin binding down to a concentration of 10 pM (10^{-12} mole). Subsequent results demonstrated the capabilities of these functionalized Si nanowire sensors as DNA sensors down to the femtomolar range [4.228]. The chemical detection devices were made in a field effect transistor geometry, so that the back-gate potential could be used to regulate the conductance in conjugation with the chemical detection and to provide a real-time direct read-out [4.227]. The extension of this device to detect multiple analytes using multiple nanowires, each sensitized to a differ-
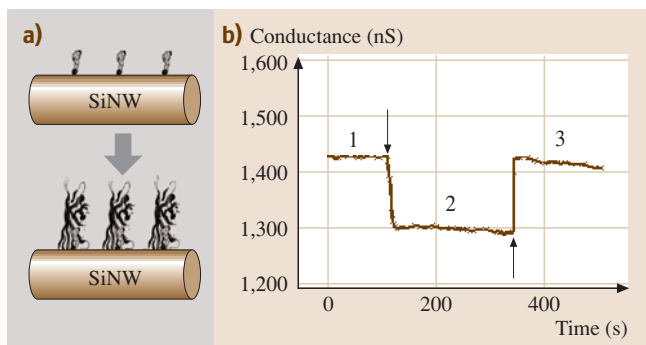
Fig. 4.44 (a) Streptavidin molecules bind to a silicon nanowire functionalized with biotin. The binding of streptavidin to biotin causes the nanowire to change its resistance. **(b)** The conductance of a biotin-modified silicon nanowire exposed to streptavidin in a buffer solution (regions 1 and 3) and with the introduction of a solution of antibiotin monoclonal antibody (region 2) [4.227]

ent analyte, could provide for fast, sensitive, and in situ screening procedures.

A similar approach was used by *Favier* et al., who made a nanosensor for the detection of hydrogen from of an array of palladium nanowires between two metal contacts [4.44]. They demonstrated that nanogaps were present in their nanowire structure, and upon absorption of H_2 and formation of Pd hydride, the nanogap structure would close and improve the electrical contact, thereby increasing the conductance of the nanowire array. The response time of these sensors was 75 msec, and they could operate in the range 0.5–5% H_2 before saturation occurred.

4.3.5 Magnetic Applications

It has been demonstrated that arrays of single-domain magnetic nanowires can be prepared with controlled nanowire diameter and length, aligned along a com-

mon direction and arranged in a close-packed ordered array (see Sect. 4.1), and that the magnetic properties (coercivity, remanence and dipolar magnetic interwire interaction) can be controlled to achieve a variety of magnetic applications [4.40, 79].

The most interesting of these applications is for magnetic storage, where the large nanowire aspect ratio (length/diameter) is advantageous for preventing the onset of the "superparamagnetic" limit at which the magnetization direction in the magnetic grains can be reversed by the thermal energy $k_B T$, thereby resulting in loss of recorded data in the magnetic recording medium. The magnetic energy in a grain can be increased by increasing either the volume or the anisotropy of the grain. If the volume is increased, the particle size increases, so the resolution is decreased. For spherical magnetized grains, the superparamagnetic limit at room temperature is reached at 70 Gbit/in^2. In nanowires, the anisotropy is very large and yet the wire diameters are small, so that the magnetostatic switching energy can easily be above the thermal energy while the spatial resolution is large. For magnetic data storage applications, a large aspect ratio is needed for the nanowires in order to maintain a high coercivity, and a sufficient separation between nanowires is needed to suppress interwire magnetic dipolar coupling. Thus nanowires can form stable and highly dense magnetic memory arrays with packing densities in excess of 10^{11} wires/cm^2.

The onset of superparamagnetism can be prevented in the single-domain magnetic nanowire arrays that have already been fabricated using either porous alumina templates to make Ni nanowires with 35 nm diameters [4.40] or diblock copolymer templates [4.79] to make Co nanowires, with mean diameters of 14 nm and 100% filling of the template pores (see 4.1.1). The ordered magnetic nanowire arrays that have already been demonstrated offer the exciting promise of systems permitting 10^{12} bits/in^2 data storage.

4.4 Concluding Remarks

In this chapter, we reviewed the synthesis, characterization and physical properties of nanowires, placing particular emphasis on nanowire properties that differ from those of the bulk counterparts and potential applications that might result from the special structures and properties of nanowires.

We have shown that the newly emerging field of nanowire research has developed very rapidly over the past few years, driven by the development of a vari-

ety of complementary nanowire synthesis methods and effective tools for measuring nanowire structure and properties (see Sects. 4.1 and 4.2). At present, much of the progress is at the demonstration-of-concept level, with many gaps in knowledge remaining to be elucidated, theoretical models to be developed, and new nanowire systems to be explored. Having demonstrated that many of the most interesting discoveries to date relate to nanowire properties not present in their bulk

material counterparts, we can expect future research emphasis to be increasingly focused on smaller diameter nanowires, where new unexplored physical phenomena related to quantum confinement effects are more likely to be found. We can also expect the development of applications to follow, some coming sooner and others later. Many promising applications are now at the early demonstration stage (see Sect. 4.3), but are moving ahead rapidly because of their promise of new functionality, not previously available, in the fields of electronics, optoelectronics, biotechnology, magnetics, and energy conversion and generation, among others. Many exciting challenges remain in advancing both the nanoscience and the nanotechnological promise already demonstrated by the nanowire research described in this review.

References

4.1 R. P. Feynman: There's plenty of room at the bottom, Eng. Sci. (Caltech, February 1960) 22

4.2 Y. Mao, S. S. Wong: General, room-temperature method for the synthesis of isolated as well as arrays of single-crystalline ABO_4-type nanorods, J. Am. Chem. Soc. **126**, 15245–15252 (2004)

4.3 E. Braun, Y. Eichen, U. Sivan, G. Ben-Yoseph: DNA-templated assembly and electrode attachment of a conducting silver wire, Nature **391**, 775–778 (1998)

4.4 G. Sauer, G. Brehm, S. Schneider, K. Nielsch, R. B. Wehrspohn, J. Choi, H. Hofmeister, U. Gösele: Highly ordered monocrystalline silver nanowire arrays, J. Appl. Phys. **91**, 3243–3247 (2002)

4.5 G. L. Hornyak, C. J. Patrissi, C. M. Martin: Fabrication, characterization and optical properties of gold nanoparticle/porous alumina composites: the non-scattering Maxwell-Garnett limit, J. Phys. Chem. B **101**, 1548–1555 (1997)

4.6 X. Y. Zhang, L. D. Zhang, Y. Lei, L. X. Zhao, Y. Q. Mao: Fabrication and characterization of highly ordered Au nanowire arrays, J. Mater. Chem. **11**, 1732–1734 (2001)

4.7 Y.-T. Cheng, A. M. Weiner, C. A. Wong, M. P. Balogh, M. J. Lukitsch: Stress-induced growth of bismuth nanowires, Appl. Phys. Lett. **81**, 3248–3250 (2002)

4.8 J. Heremans, C. M. Thrush, Y.-M. Lin, S. Cronin, Z. Zhang, M. S. Dresselhaus, J. F. Mansfield: Bismuth nanowire arrays: synthesis, galvanomagnetic properties, Phys. Rev. B **61**, 2921–2930 (2000)

4.9 L. Piraux, S. Dubois, J. L. Duvail, A. Radulescu, S. Demoustier-Champagne, E. Ferain, R. Legras: Fabrication and properties of organic, metal nanocylinders in nanoporous membranes, J. Mater. Res. **14**, 3042–3050 (1999)

4.10 K. Hong, F. Y. Yang, K. Liu, D. H. Reich, P. C. Searson, C. L. Chien, F. F. Balakirev, G. S. Boebinger: Giant positive magnetoresistance of Bi nanowire arrays in high magnetic fields, J. Appl. Phys. **85**, 6184–6186 (1999)

4.11 A. J. Yin, J. Li, W. Jian, A. J. Bennett, J. M. Xu: Fabrication of highly ordered metallic nanowire arrays by electrodeposition, Appl. Phys. Lett. **79**, 1039–1041 (2001)

4.12 Z. Zhang, J. Y. Ying, M. S. Dresselhaus: Bismuth quantum-wire arrays fabricated by a vacuum melting and pressure injection process, J. Mater. Res. **13**, 1745–1748 (1998)

4.13 Z. Zhang, D. Gekhtman, M. S. Dresselhaus, J. Y. Ying: Processing and characterization of single-crystalline ultrafine bismuth nanowires, Chem. Mater. **11**, 1659–1665 (1999)

4.14 T. E. Huber, M. J. Graf, P. Constant: Processing and characterization of high-conductance bismuth wire array composites, J. Mater. Res. **15**, 1816–1821 (2000)

4.15 L. Li, G. Li, Y. Zhang, Y. Yang, L. Zhang: Pulsed electrodeposition of large-area, ordered $Bi_{1-x}Sb_x$ nanowire arrays from aqueous solutions, J. Phys. Chem. B **108**, 19380–19383 (2004)

4.16 M. S. Sander, A. L. Prieto, R. Gronsky, T. Sands, A. M. Stacy: Fabrication of high-density, high aspect ratio, large-area bismuth telluride nanowire arrays by electrodeposition into porous anodic alumina templates, Adv. Mater. **14**, 665–667 (2002)

4.17 M. Chen, Y. Xie, J. Lu, Y. J. Xiong, S. Y. Zhang, Y. T. Qian, X. M. Liu: Synthesis of rod-, twinrod-, and tetrapod-shaped CdS nanocrystals using a highly oriented solvothermal recrystallization technique, J. Mater. Chem. **12**, 748–753 (2002)

4.18 D. Xu, Y. Xu, D. Chen, G. Guo, L. Gui, Y. Tang: Preparation of CdS single-crystal nanowires by electrochemically induced deposition, Adv. Mater. **12**, 520–522 (2000)

4.19 D. Routkevitch, T. Bigioni, M. Moskovits, J. M. Xu: Electrochemical fabrication of CdS nanowire arrays in porous anodic aluminum oxide templates, J. Phys. Chem. **100**, 14037–14047 (1996)

4.20 L. Manna, E. C. Scher, A. P. Alivisatos: Synthesis of soluble and processable rod-, arrow-, teardrop-, and tetrapod-shaped CdSe nanocrystals, J. Am. Chem. Soc. **122**, 12700–12706 (2000)

4.21 D. Routkevitch, A. A. Tager, J. Haruyama, D. Al-Mawlawi, M. Moskovits, J. M. Xu: Nonlithographic nano-wire arrays: fabrication, physics, and device applications, IEEE Trans. Electron. Dev. **43**, 1646–1658 (1996)

4.22 D. S. Xu, D. P. Chen, Y. J. Xu, X. S. Shi, G. L. Guo, L. L. Gui, Y. Q. Tang: Preparation of II–VI group semi-

conductor nanowire arrays by dc electrochemical deposition in porous aluminum oxide templates, Pure Appl. Chem. **72**, 127–135 (2000)

4.23   R. Adelung, F. Ernst, A. Scott, M. Tabib-Azar, L. Kipp, M. Skibowski, S. Hollensteiner, E. Spiecker, W. Jäger, S. Gunst, A. Klein, W. Jägermann, V. Zaporojtchenko, F. Faupel: Self-assembled nanowire networks by deposition of copper onto layered-crystal surfaces, Adv. Mater. **14**, 1056–1061 (2002)

4.24   T. Gao, G. W. Meng, J. Zhang, Y. W. Wang, C. H. Liang, J. C. Fan, L. D. Zhang: Template synthesis of single-crystal Cu nanowire arrays by electrodeposition, Appl. Phys. A **73**, 251–254 (2001)

4.25   D. Al-Mawlawi, N. Coombs, M. Moskovits: Magnetic-properties of Fe deposited into anodic aluminum-oxide pores as a function of particle-size, J. Appl. Phys. **70**, 4421–4425 (1991)

4.26   F. Li, R. M. Metzger: Activation volume of α-Fe particles in alumite films, J. Appl. Phys. **81**, 3806–3808 (1997)

4.27   A. Sugawara, T. Coyle, G. G. Hembree, M. R. Scheinfein: Self-organized Fe nanowire arrays prepared by shadow deposition on NaCl(110) templates, Appl. Phys. Lett. **70**, 1043–1045 (1997)

4.28   G. S. Cheng, L. D. Zhang, Y. Zhu, G. T. Fei, L. Li, C. M. Mo, Y. Q. Mao: Large-scale synthesis of single crystalline gallium nitride nanowires, Appl. Phys. Lett. **75**, 2455–2457 (1999)

4.29   G. S. Cheng, L. D. Zhang, S. H. Chen, Y. Li, L. Li, X. G. Zhu, Y. Zhu, G. T. Fei, Y. Q. Mao: Ordered nanostructure of single-crystalline GaN nanowires in a honeycomb structure of anodic alumina, J. Mater. Res. **15**, 347–350 (2000)

4.30   Y. Huang, X. Duan, Y. Cui, C. M. Lieber: Gallium nitride nanowire nanodevices, Nano Lett. **2**, 101–104 (2002)

4.31   X. Duan, C. M. Lieber: Laser-assisted catalytic growth of single crystal GaN nanowires, J. Am. Chem. Soc. **122**, 188–189 (2000)

4.32   A. D. Berry, R. J. Tonucci, M. Fatemi: Fabrication of GaAs, InAs wires in nanochannel glass, Appl. Phys. Lett. **69**, 2846–2848 (1996)

4.33   J. R. Heath, F. K. LeGoues: A liquid solution synthesis of single-crystal germanium quantum wires, Chem. Phys. Lett. **208**, 263–268 (1993)

4.34   Y. Wu, P. Yang: Germanium nanowire growth via simple vapor transport, Chem. Mater. **12**, 605–607 (2000)

4.35   Y. F. Zhang, Y. H. Tang, N. Wang, C. S. Lee, I. Bello, S. T. Lee: Germanium nanowires sheathed with an oxide layer, Phys. Rev. B **61**, 4518–4521 (2000)

4.36   S. J. May, J.-G. Zheng, B. W. Wessels, L. J. Lauhon: Dendritic nanowire growth mediated by a self-assembled catalyst, Adv. Mater. **17**, 598–602 (2005)

4.37   S. Han, C. Li, Z. Liu, B. Lei, D. Zhang, W. Jin, X. Liu, T. Tang, C. Zhou: Transition metal oxide core-shell

nanowires: Generic synthesis and transport studies, Nano Lett. **4**, 1241–1246 (2004)

4.38   M. P. Zach, K. H. Ng, R. M. Penner: Molybdenum nanowires by electrodeposition, Science **290**, 2120–2123 (2000)

4.39   L. Sun, P. C. Searson, L. Chien: Electrochemical deposition of nickel nanowire arrays in single-crystal mica films, Appl. Phys. Lett. **74**, 2803–2805 (1999)

4.40   K. Nielsch, R. Wehrspohn, S. Fischer, H. Kronmuller, J. Barthel, J. Kirschner, U. Gosele: Magnetic properties of 100 nm nickel nanowire arrays obtained from ordered porous alumina templates, MRS Symp. Proc. **636**, D1.9 1–6 (2001)

4.41   Y. Wang, X. Jiang, T. Herricks, Y. Xia: Single crystalline nanowires of lead: large-scale synthesis, mechanistic studies, and transport measurements, J. Phys. Chem. B **108**, 8631–8640 (2004)

4.42   E. Lifshitz, M. Bashouti, V. Kloper, A. Kigel, M. S. Eisen, S. Berger: Synthesis and characterization of PbSe quantum wires, multipods, quantum rods, cubes, Nano Lett. **3**, 857–862 (2003)

4.43   W. Lu, P. Gao, W. B. Jian, Z. L. Wang, J. Fang: Perfect orientation ordered in-situ one-dimensional self-assembly of Mn-doped PbSe nanocrystals, J. Am. Chem. Soc. **126**, 14816–14821 (2004)

4.44   F. Favier, E. C. Walter, M. P. Zach, T. Benter, R. M. Penner: Hydrogen sensors and switches from electrodeposited palladium mesowire arrays, Science **293**, 2227–2231 (2001)

4.45   B. Gates, B. Mayers, B. Cattle, Y. Xia: Synthesis, characterization of uniform nanowires of trigonal selenium, Adv. Funct. Mater. **12**, 219–227 (2002)

4.46   C. A. Huber, T. E. Huber, M. Sadoqi, J. A. Lubin, S. Manalis, C. B. Prater: Nanowire array composites, Science **263**, 800–802 (1994)

4.47   Y. Cui, L. J. Lauhon, M. S. Gudiksen, J. Wang, C. M. Lieber: Diameter-controlled synthesis of single crystal silicon nanowires, Appl. Phys. Lett. **78**, 2214–2216 (2001)

4.48   A. M. Morales, C. M. Lieber: A laser ablation method for the synthesis of crystalline semiconductor nanowires, Science **279**, 208–211 (1998)

4.49   N. Wang, Y. F. Zhang, Y. H. Tang, C. S. Lee, S. T. Lee: SiO_2-enhanced synthesis of Si nanowires by laser ablation, Appl. Phys. Lett. **73**, 3902–3904 (1998)

4.50   M. K. Sunkara, S. Sharma, R. Miranda, G. Lian, E. C. Dickey: Bulk synthesis of silicon nanowires using a low-temperature vapor-liquid-solid method, Appl. Phys. Lett. **79**, 1546–1548 (2001)

4.51   S. Vaddiraju, H. Chandrasekaran, M. K. Sunkara: Vapor phase synthesis of tungsten nanowires, J. Am. Chem. Soc. **125**, 10792–10793 (2003)

4.52   J. P. Heremans, C. M. Thrush, D. T. Morelli, M.-C. Wu: Thermoelectric power of bismuth nanocomposites, Phys. Rev. Lett. **88**, 216801(1–4) (2002)

4.53   Y. Li, G. S. Cheng, L. D. Zhang: Fabrication of highly ordered ZnO nanowire arrays in anodic alu-

mina membranes, J. Mater. Res. **15**, 2305–2308 (2000)

4.54 P. Yang, H. Yan, S. Mao, R. Russo, J. Johnson, R. Saykally, N. Morris, J. Pham, R. He, H.-J. Choi: Controlled growth of ZnO nanowires and their optical properties, Adv. Funct. Mater. **12**, 323–331 (2002)

4.55 M. J Zheng, L. D. Zhang, G. H. Li, W. Z. Shen: Fabrication and optical properties of large-scale uniform zinc oxide nanowire arrays by one-step electrochemical deposition technique, Chem. Phys. Lett. **363**, 123–128 (2002)

4.56 M. S. Dresselhaus, Y.-M. Lin, O. Rabin, A. Jorio, A. G. Souza Filho, M. A. Pimenta, R. Saito, G. G. Samsonidze, G. Dresselhaus: Nanowires and nanotubes, Mater. Sci. Eng. **C 23**, 129–140 (2003) (also in: *Current Trends in Nanotechnologies: From Materials to Systems (Europ. Mater. Res. Soc. Symp. Proc. 140)*, ed. by W. Jantsch, H. Grimmeiss and G. Marietta (Elsevier, Amsterdam 2002)

4.57 R. Saito, G. Dresselhaus, M. S. Dresselhaus: *Physical Properties of Carbon Nanotubes* (Imperial College Press, London 1998)

4.58 M. S. Dresselhaus, G. Dresselhaus, P. Avouris: Carbon nanotubes: synthesis, structure, properties and applications, Springer Ser. Top. Appl. Phys. **80**, 1–447 (2001)

4.59 R. C. Haddon: Special issue on carbon nanotubes, Acc. Chem. Res. **35**, 997–1113 (2002)

4.60 Y.-M. Lin, X. Sun, S. Cronin, Z. Zhang, J. Y. Ying, M. S. Dresselhaus: Fabrication, transport properties of Te-doped bismuth nanowire arrays. In: *Molecular Electronics: MRS Symposium Proceedings*, Vol. 582, ed. by S. T. Pantelides, M. A. Reed, J. Murday, A. Aviran (Materials Research Society Press, Pittsburgh 2000) Chap. H10.3, pp. 1–6

4.61 C. R. Martin: Nanomaterials: A membrane-based synthetic approach, Science **266**, 1961–1966 (1994)

4.62 G. A. Ozin: Nanochemistry: synthesis in diminishing dimensions, Adv. Mater. **4**, 612–649 (1992)

4.63 R. J. Tonucci, B. L. Justus, A. J. Campillo, C. E. Ford: Nanochannel array glass, Science **258**, 783–785 (1992)

4.64 J. Y. Ying: Nanoporous systems and templates, Sci. Spec. **18**, 56–63 (1999)

4.65 J. W. Diggle, T. C. Downie, C. W. Goulding: Anodic oxide films on aluminum, Chem. Rev. **69**, 365–405 (1969)

4.66 J. P. O'Sullivan, G. C. Wood: The morphology and mechanism of formation of porous anodic films on aluminum, Proc. R. Soc. Lond. **A 317**, 511–543 (1970)

4.67 A. P. Li, F. Müller, A. Birner, K. Neilsch, U. Gösele: Hexagonal pore arrays with a 50–420 nm interpore distance formed by self-organization in anodic alumina, J. Appl. Phys. **84**, 6023–6026 (1998)

4.68 J. P. Sullivan, G. C. Wood: The morphology, mechanism of formation of porous anodic films on aluminum, Proc. R. Soc. Lond. **A 317**, 511–543 (1970)

4.69 O. Jessensky, F. Müller, U. Gössele: Self-organized formation of hexagonal pore arrays in anodic alumina, Appl. Phys. Lett. **72**, 1173–1175 (1998)

4.70 F. Li, L. Zhang, R. M. Metzger: On the growth of highly ordered pores in anodized aluminum oxide, Chem. Mater. **10**, 2470–2480 (1998)

4.71 H. Masuda, M. Satoh: Fabrication of gold nanodot array using anodic porous alumina as an evaporation mask, Jpn. J. Appl. Phys. **35**, L126–L129 (1996)

4.72 E. Ferain, R. Legras: Track-etched membrane – dynamics of pore formation, Nucl. Instrum. Meth. B **84**, 331–336 (1993)

4.73 A. Blondel, J. P. Meier, B. Doudin, J.-P. Ansermet: Giant magnetoresistance of nanowires of multilayers, Appl. Phys. Lett. **65**, 3019–3021 (1994)

4.74 K. Liu, C. L. Chien, P. C. Searson, Y. Z. Kui: Structural and magneto-transport properties of electrodeposited bismuth nanowires, Appl. Phys. Lett. **73**, 1436–1438 (1998)

4.75 C. A. Huber, T. E. Huber: A novel microstructure: semiconductor-impregnated porous Vycor glass, J. Appl. Phys. **64**, 6588–6590 (1988)

4.76 J. S. Beck, J. C. Vartuli, W. J. Roth, M. E. Leonowicz, C. T. Kresge, K. D. Schmitt, C. T.-W. Chu, D. H. Olson, E. W. Sheppard, S. B. McCullen, J. B. Higgins, J. L. Schlenker: A new family of mesoporous molecular sieves prepared with liquid crystal templates, J. Am. Chem. Soc. **114**, 10834–10843 (1992)

4.77 C.-G. Wu, T. Bein: Conducting polyaniline filaments in a mesoporous channel host, Science **264**, 1757–1759 (1994)

4.78 Y.-M. Lin, S. B. Cronin, J. Y. Ying, M. S. Dresselhaus, J. P. Heremans: Transport properties of Bi nanowire arrays, Appl. Phys. Lett. **76**, 3944–3946 (2000)

4.79 T. Thurn-Albrecht, J. Schotter, G. A. Kästle, N. Emley, T. Shibauchi, L. Krusin-Elbaum, K. Guarini, C. T. Black, M. T. Tuominen, T. P. Russell: Ultrahigh-density nanowire arrays grown in self-assembled diblock copolymer templates, Science **290**, 2126–2129 (2000)

4.80 A. W. Adamson: *Physical Chemistry of Surfaces* (Wiley, New York 1982) p. 338

4.81 R. Ferré, K. Ounadjela, J. M. George, L. Piraux, S. Dubois: Magnetization processes in nickel and cobalt electrodeposited nanowires, Phys. Rev. B **56**, 14066–14075 (1997)

4.82 H. Zeng, M. Zheng, R. Skomski, D. J. Sellmyer, Y. Liu, L. Menon, S. Bandyopadhyay: Magnetic properties of self-assembled Co nanowires of varying length and diameter, J. Appl. Phys **87**, 4718–4720 (2000)

4.83 Y. Peng, H. L. Zhang, S.-L. Pan, H.-L. Li: Magnetic properties and magnetization reversal of α-Fe nanowires deposited in alumina film, J. Appl. Phys. **87**, 7405–7408 (2000)

4.84 L. Piraux, J. M. George, J. F. Despres, C. Leroy, E. Ferain, R. Legras, K. Ounadjela, A. Fert: Giant magnetoresistance in magnetic multilay-

ered nanowires, Appl. Phys. Lett. **65**, 2484–2486 (1994)

4.85 S. Bhattacharrya, S.K. Saha, D. Chakravorty: Nanowire formation in a polymeric film, Appl. Phys. Lett. **76**, 3896–3898 (2000)

4.86 G. Yi, W. Schwarzacher: Single crystal superconductor nanowires by electrodeposition, Appl. Phys. Lett. **74**, 1746–1748 (1999)

4.87 D. Al-Mawlawi, C.Z. Liu, M. Moskovits: Nanowires formed in anodic oxide nanotemplates, J. Mater. Res. **9**, 1014–1018 (1994)

4.88 R.S. Wagner, W.C. Ellis: Vapor–liquid–solid mechanism of single crystal growth, Appl. Phys. Lett. **4**, 89–90 (1964)

4.89 Y. Wu, P. Yang: Direct observation of vapor–liquid–solid nanowire growth, J. Am. Chem. Soc. **123**, 3165–3166 (2001)

4.90 Y. Wu, R. Fan, P. Yang: Block-by-block growth of single-crystalline Si/SiGe superlattice nanowires, Nano Lett. **2**, 83–86 (2002)

4.91 S. Sharma, M.K. Sunkara, R. Miranda, G. Lian, E.C. Dickey: A novel low temperature synthesis method for semiconductor nanowires. In: *Synthesis, Functional Properties and Applications of Nanostructures: Mat. Res. Soc. Symp. Proc., San Francisco, Spring 2001*, Vol. 676, ed. by H.W. Hahn, D.L. Feldheim, C.P. Kubiak, R. Tannenbaum, R.W. Siegel (Materials Research Society Press, Pittsburgh 2001) p. Y1.6

4.92 M.S. Gudiksen, L.J. Lauhon, J. Wang, D.C. Smith, C.M. Lieber: Growth of nanowire superlattice structures for nanoscale photonics and electronics, Nature **415**, 617–620 (2002)

4.93 Y. Wu, J. Xiang, C. Yang, W. Lu, C.M. Lieber: Single-crystal metallic nanowires and metal/semiconductor nanowire heterostructures, Nature **430**, 61–65 (2004)

4.94 M.T. Björk, B.J. Ohlsson, T. Sass, A.I. Persson, C. Thelander, M.H. Magnusson, K. Deppert, L.R. Wallenberg, L. Samuelson: One-dimensional steeplechase for electrons realized, Nano Lett. **2**, 87–89 (2002)

4.95 N. Wang, Y.H. Tang, Y.F. Zhang, C.S. Lee, S.T. Lee: Nucleation and growth of Si nanowires from silicon oxide, Phys. Rev. B **58**, R16024–R16026 (1998)

4.96 Y.F. Zhang, Y.H. Tang, N. Wang, C.S. Lee, I. Bello, S.T. Lee: One-dimensional growth mechanism of crystalline silicon nanowires, J. Cryst. Growth **197**, 136–140 (1999)

4.97 S.T. Lee, Y.F. Zhang, N. Wang, Y.H. Tang, I. Bello, C.S. Lee, Y.W. Chung: Semiconductor nanowires from oxides, J. Mater. Res. **14**, 4503–4507 (1999)

4.98 D.D.D. Ma, C.S. Lee, Y. Lifshitz, S.T. Lee: Periodic array of intramolecular junctions of silicon nanowires, Appl. Phys. Lett. **81**, 3233–3235 (2002)

4.99 D. Whang, S. Jin, C.M. Lieber: Large-scale hierarchical organization of nanowires for functional nanosystems, Jpn. J. Appl. Phys. **43**, 4465–4470 (2004)

4.100 B. Gates, Y. Yin, Y. Xia: A solution-phase approach to the synthesis of uniform nanowires of crystalline selenium with lateral dimensions in the range of 10–30 nm, J. Am. Chem. Soc. **122**, 12582–12583 (2000)

4.101 B. Mayers, B. Gates, Y. Yin, Y. Xia: Large-scale synthesis of monodisperse nanorods of Se/Te alloys through a homogeneous nucleation and solution growth process, Adv. Mater. **13**, 1380–1384 (2001)

4.102 B. Gates, Y. Wu, Y. Yin, P. Yang, Y. Xia: Single-crystalline nanowires of Ag_2Se can be synthesized by templating against nanowires of trigonal Se, J. Am. Chem. Soc. **123**, 11500–11501 (2001)

4.103 B. Gates, B. Mayers, Y. Wu, Y. Sun, B. Cattle, P. Yang, Y. Xia: Synthesis and characterization of crystalline Ag_2Se nanowires through a template-engaged reaction at room temperature, Adv. Funct. Mater. **12**, 679–686 (2002)

4.104 H. Yu, P.C. Gibbons, W.E. Buhro: Bismuth, tellurium and bismuth telluride nanowires, J. Mater. Chem. **14**, 595–602 (2004)

4.105 M.P. Zach, K. Inazu, K.H. Ng, J.C. Hemminger, R.M. Penner: Synthesis of molybdenum nanowires with millimeter-scale lengths using electrochemical step edge decoration, Chem. Mater. **14**, 3206–3216 (2002)

4.106 X. Peng, J. Wickham, A.P. Alivisatos: Kinetics of II–VI, III–V colloidal semiconductor nanocrystal growth: 'Focusing' of size distributions, J. Am. Chem. Soc. **120**, 5343–5344 (1998)

4.107 N.A. Melosh, A. Boukai, F. Diana, B. Gerardot, A. Badolto, P.M. Petroff, J.R. Heath: Ultrahigh-density nanowire lattices and circuits, Science **300**, 112–115 (2003)

4.108 J.Y. Lao, J.G. Wen, Z.F. Ren: Hierarchical ZnO nanostructures, Nano. Lett. **2**, 1287–1291 (2002)

4.109 J.Y. Lao, J.Y. Huang, D.Z. Wang, Z.F. Ren: ZnO nanobridges and nanonails, Nano Lett. **3**, 235–238 (2003)

4.110 S.R. Nicewarner-Peña, R.G. Freeman, B.D. Reiss, L. He, D.J. Peña, I.D. Walton, R. Cromer, C.D. Keating, M.J. Natan: Submicrometer metallic barcodes, Science **294**, 137–141 (2001)

4.111 L.J. Lauhon, M.S. Gudiksen, D. Wang, C.M. Lieber: Epitaxial core-shell and core-multishell nanowire heterostructures, Nature **420**, 57–61 (2002)

4.112 Z.L. Wang, Z.R. Dai, R.P. Gao, Z.G. Bai, J.L. Gole: Side-by-side silicon carbide-silica biaxial nanowires: Synthesis, structure and mechanical properties, Appl. Phys. Lett. **77**, 3349–3351 (2000)

4.113 P. Yang, F. Kim: Langmuir-Blodgett assembly of one-dimensional nanostructures, ChemPhysChem **3**, 503–506 (2002)

4.114 B. Messer, J.H. Song, P. Yang: Microchannel networks for nanowire patterning, J. Am. Chem. Soc. **122**, 10232–10233 (2000)

4.115 P. A. Smith, C. D. Nordquist, T. N. Jackson, T. S. Mayer, B. R. Martin, J. Mbindyo, T. E. Mallouk: Electric-field assisted assembly and alignment of metallic nanowires, Appl. Phys. Lett. **77**, 1399–1401 (2000)

4.116 S. Jin, D. M. Whang, M. C. McAlpine, R. S. Friedman, Y. Wu, C. M. Lieber: Scalable interconnection and integration of nanowire devices without registration, Nano Lett. **4**, 915–919 (2004)

4.117 T. Kuykendall, P. J. Pauzauskie, Y. F. Zhang, J. Goldberger, D. Sirbuly, J. Denlinger, P. D. Yang: Crystallographic alignment of high-density gallium nitride nanowire arrays, Nature Mater. **3**, 524–528 (2004)

4.118 H. Masuda, H. Yamada, M. Satoh, H. Asoh, M. Nakao, T. Tamamura: Highly ordered nanochannel-array architecture in anodic alumina, Appl. Phys. Lett. **71**, 2770–2772 (1997)

4.119 O. Rabin, P. R. Herz, S. B. Cronin, Y.-M. Lin, A. I. Akinwande, M. S. Dresselhaus: Nanofabrication using self-assembled alumina templates. In: *Nonlithographic and Lithographic Methods for Nanofabrication: MRS Symposium Proceedings, Boston, November 2000*, Vol. 636, ed. by J. A. Rogers, A. Karim, L. Merhari, D. Norris, Y. Xia (Materials Research Society Press, Pittsburgh 2001) pp. D4.7(1–6)

4.120 O. Rabin, P. R. Herz, Y.-M. Lin, A. I. Akinwande, S. B. Cronin, M. S. Dresselhaus: Formation of thick porous anodic alumina films and nanowire arrays on silicon wafers and glass., Adv. Funct. Mater. **13**, 631–638 (2003)

4.121 O. Rabin, P. R. Herz, Y.-M. Lin, S. B. Cronin, A. I. Akinwande, M. S. Dresselhaus: Arrays of nanowires on silicon wafers. In: *21st Int. Conf. Thermoelectrics: Proc. ICT '02 Long Beach, CA* (IEEE Inc., Piscataway, NJ 2002) pp. 276–279

4.122 M. H. Huang, S. Mao, H. Feick, H. Yan, Y. Wu, H. Kind, E. Weber, R. Russo, P. Yang: Room-temperature ultraviolet nanowire nanolasers, Science **292**, 1897–1899 (2001)

4.123 Y. H. Tang, Y. F. Zhang, N. Wang, C. S. Lee, X. D. Han, I. Bello, S. T. Lee: Morphology of Si nanowires synthesized by high-temperature laser ablation, J. Appl. Phys. **85**, 7981–7983 (1999)

4.124 Y. Ding, Z. L. Wang: Structure analysis of nanowires and nanobelts by transmission electron microscopy, J. Phys. Chem. B **108**, 12280–12291 (2004)

4.125 S. B. Cronin, Y.-M. Lin, O. Rabin, M. R. Black, G. Dresselhaus, M. S. Dresselhaus, P. L. Gai: Bismuth nanowires for potential applications in nanoscale electronics technology, Microsc. Microanal. **8**, 58–63 (2002)

4.126 M. S. Sander, R. Gronsky, Y.-M. Lin, M. S. Dresselhaus: Plasmon excitation modes in nanowire arrays, J. Appl. Phys. **89**, 2733–2736 (2001)

4.127 L. Venkataraman, C. M. Lieber: Molybdenum selenide molecular wires as one-dimensional conductors, Phys. Rev. Lett. **83**, 5334–5337 (1999)

4.128 A. Majumdar: Scanning thermal microscopy, Annu. Rev. Mater. Sci. **29**, 505–585 (1999)

4.129 K. M. Unruh, T. E. Huber, C. A. Huber: Melting and freezing behavior of indium metal in porous glasses, Phys. Rev. B **48**, 9021–9027 (1993)

4.130 Y. Y. Wu, P. D. Yang: Melting and welding semiconductor nanowires in nanotubes, Adv. Mater. **13**, 520–523 (2001)

4.131 P. M. Ajayan, S. Iijima: Capillarity-induced filling of carbon nanotubes, Nature **361**, 333–334 (1993)

4.132 Y. Gao, Y. Bando: Carbon nanothermometer containing gallium, Nature **415**, 599 (2002)

4.133 M. E. T. Morales, A. G. Balogh, T. W. Cornelius, R. Neumann, C. Trautmann: Fragmentation of nanowires driven by Rayleigh instability, Appl. Phys. Lett. **84**, 5337–5339 (2004)

4.134 D. A. Wharam, T. J. Thornton, R. Newbury, M. Pepper, H. Ahmed, J. E. F. Frost, D. G. Hasko, D. C. Peacock, D. A. Ritchie, G. A. C. Jones: One-dimensional transport and the quantization of the ballistic resistance, J. Phys. C **21**, L209–L214 (1988)

4.135 B. J. van Wees, H. van Houten, C. W. J. Beenakker, J. G. Williamson, L. P. Kouvenhoven, D. van der Marel, C. T. Foxon: Quantized conductance of point contacts in a two-dimensional electron gas, Phys. Rev. Lett. **60**, 848–850 (1988)

4.136 C. J. Muller, J. M. van Ruitenbeek, L. J. deJongh: Conductance and supercurrent discontinuities in atomic-scale metallic constrictions of variable width, Phys. Rev. Lett. **69**, 140–143 (1992)

4.137 C. J. Muller, J. M. Krans, T. N. Todorov, M. A. Reed: Quantization effects in the conductance of metallic contacts at room temperature, Phys. Rev. B **53**, 1022–1025 (1996)

4.138 J. L. Costa-Krämer, N. Garcia, H. Olin: Conductance quantization in bismuth nanowires at 4 K, Phys. Rev. Lett. **78**, 4990–4993 (1997)

4.139 J. L. Costa-Krämer, N. Garcia, H. Olin: Conductance quantization histograms of gold nanowires at 4 K, Phys. Rev. B **55**, 12910–12913 (1997)

4.140 C. Z. Li, H. X. He, A. Bogozi, J. S. Bunch, N. J. Tao: Molecular detection based on conductance quantization of nanowires, Appl. Phys. Lett. **76**, 1333–1335 (2000)

4.141 J. L. Costa-Krämer, N. Garcia, P. Garcia-Mochales, P. A. Serena, M. I. Marques, A. Correia: Conductance quantization in nanowires formed between micro and macroscopic metallic electrodes, Phys. Rev. B **55**, 5416–5424 (1997)

4.142 Y. Huang, X. Duan, Y. Cui, L. J. Lauhon, K.-H. Kim, C. M. Lieber: Logic gates and computation from assembled nanowire building blocks, Science **294**, 1313–1317 (2001)

4.143 J.-R. Kim, H. Oh, H. M. So, J.-J. Kim, J. Kim, C. J. Lee, S. C. Lyu: Schottky diodes based on a single GaN nanowire, Nanotechnology **13**, 701–704 (2002)

4.144 X. Duan, Y. Huang, C. M. Lieber: Nonvolatile memory and programmable logic from molecule-gated nanowires, Nano Lett. **2**, 487–490 (2002)

4.145 E.C. Walter, R.M. Penner, H. Liu, K.H. Ng, M.P. Zach, F. Favier: Sensors from electrodeposited metal nanowires, Surf. Inter. Anal. **34**, 409–412 (2002)

4.146 E.C. Walter, K.H. Ng, M.P. Zach, R.M. Penner, F. Favier: Electronic devices from electrodeposited metal nanowires, Microelectron. Eng. **61-62**, 555–561 (2002)

4.147 Y.-M. Lin, X. Sun, M.S. Dresselhaus: Theoretical investigation of thermoelectric transport properties of cylindrical Bi nanowires, Phys. Rev. B **62**, 4610–4623 (2000)

4.148 K. Liu, C.L. Chien, P.C. Searson: Finite-size effects in bismuth nanowires, Phys. Rev. B **58**, R14681–R14684 (1998)

4.149 Z. Zhang, X. Sun, M.S. Dresselhaus, J.Y. Ying, J. Heremans: Magnetotransport investigations of ultrafine single-crystalline bismuth nanowire arrays, Appl. Phys. Lett. **73**, 1589–1591 (1998)

4.150 J. Heremans, C.M. Thrush, Z. Zhang, X. Sun, M.S. Dresselhaus, J.Y. Ying, D.T. Morelli: Magnetoresistance of bismuth nanowire arrays: A possible transition from one-dimensional to three-dimensional localization, Phys. Rev. B **58**, R10091–R10095 (1998)

4.151 L. Sun, P.C. Searson, C.L. Chien: Finite-size effects in nickel nanowire arrays, Phys. Rev. B **61**, R6463–R6466 (2000)

4.152 Y.-M. Lin, S.B. Cronin, O. Rabin, J.Y. Ying, M.S. Dresselhaus: Transport properties and observation of semimetal-semiconductor transition in Bi-based nanowires. In: *Quantum Confined Semiconductor Nanostructures: MRS Symposium Proceedings, Boston, December 2002*, Vol. 737-C, ed. by J.M. Buriak, D.D.M. Wayner, F. Priolo, B. White, V. Klimov, L. Tsybeskov (Materials Research Society Press, Pittsburgh 2003) p. F3.14

4.153 Y.-M. Lin, M.S. Dresselhaus: Transport properties of superlattice nanowires and their potential for thermoelectric applications. In: *Quantum Confined Semiconductor Nanostructures: MRS Symposium Proceedings, Boston, December 2002*, Vol. 737-C, ed. by J.M. Buriak, D.D.M. Wayner, F. Priolo, B. White, V. Klimov, L. Tsybeskov (Materials Research Society Press, Pittsburgh 2003) p. F8.18

4.154 Y.-M. Lin, O. Rabin, S.B. Cronin, J.Y. Ying, M.S. Dresselhaus: Semimetal-semiconductor transition in $Bi_{1-x}Sb_x$ alloy nanowires and their thermoelectric properties, Appl. Phys. Lett. **81**, 2403–2405 (2002)

4.155 J. Heremans, C.M. Thrush, Y.-M. Lin, S.B. Cronin, M.S. Dresselhaus: Transport properties of antimony nanowires, Phys. Rev. B **63**, 085406(1–8) (2001)

4.156 Y.-M. Lin, S.B. Cronin, O. Rabin, J.Y. Ying, M.S. Dresselhaus: Transport properties of $Bi_{1-x}Sb_x$ alloy nanowires synthesized by pressure injection, Appl. Phys. Lett. **79**, 677–679 (2001)

4.157 D.E. Beutler, N. Giordano: Localization and electron–electron interaction effects in thin Bi wires and films, Phys. Rev. B **38**, 8–19 (1988)

4.158 Z. Zhang, X. Sun, M.S. Dresselhaus, J.Y. Ying, J. Heremans: Electronic transport properties of single crystal bismuth nanowire arrays, Phys. Rev. B **61**, 4850–4861 (2000)

4.159 J. Heremans, C.M. Thrush: Thermoelectric power of bismuth nanowires, Phys. Rev. B **59**, 12579–12583 (1999)

4.160 Y.-M. Lin, S.B. Cronin, O. Rabin, J. Heremans, M.S. Dresselhaus, J.Y. Ying: Transport properties of Bi-related nanowire systems. In: *Anisotropic Nanoparticles: Synthesis, Characterization and Applications: MRS Symposium Proceedings, Boston, December 2000*, Vol. 635, ed. by S. Stranick, P.C. Searson, L.A. Lyon, C. Keating (Materials Research Society Press, Pittsburgh 2001) pp. C4301–C4306

4.161 L.D. Hicks, M.S. Dresselhaus: Thermoelectric figure of merit of a one-dimensional conductor, Phys. Rev. B **47**, 16631–16634 (1993)

4.162 Y.-M. Lin, M.S. Dresselhaus: Thermoelectric properties of superlattice nanowires, Phys. Rev. B **68**, 075304 (2003)

4.163 M.T. Björk, B.J. Ohlsson, C. Thelander, A.I. Persson, K. Deppert, L.R. Wallenberg, L. Samuelson: Nanowire resonant tunneling diodes, Appl. Phys. Lett. **81**, 4458–4460 (2002)

4.164 D. Li, Y. Wu, P. Kim, L. Shi, P. Yang, A. Majumdar: Thermal conductivity of individual silicon nanowires, Appl Phys. Lett. **83**, 2934–2936 (2003)

4.165 T.S. Tighe, J.M. Worlock, M.L. Roukes: Direct thermal conductance measurements on suspended monocrystalline nanostructures, Appl. Phys. Lett. **70**, 2687–2689 (1997)

4.166 S.T. Huxtable, A.R. Abramson, C.-L. Tien, A. Majumdar, C. LaBounty, X. Fan, G. Zeng, J.E. Bowers, A. Shakouri, E.T. Croke: Thermal conductivity of Si/SiGe and SiGe/SiGe superlattices, Appl. Phys. Lett. **80**, 1737–1739 (2002)

4.167 R. Venkatasubramanian, E. Siivola, T. Colpitts, B. O'Quinn: Thin-film thermoelectric devices with high room-temperature figures of merit, Nature **413**, 597–602 (2001)

4.168 D. Li, Y. Wu, R. Fan, P. Yang, A. Majumdar: Thermal conductivity of Si/SiGe superlattice nanowires, Appl. Phys. Lett. **83**, 3186–3188 (2003)

4.169 C. Dames, G. Chen: Modeling the thermal conductivity of a SiGe segmented nanowire. In: *21st Int. Conf. Thermoelectrics: Proc. ICT '02, Long Beach, CA* (IEEE, Piscataway, NJ 2002) pp. 317–320

4.170 K. Schwab, J.L. Arlett, J.M. Worlock, M.L. Roukes: Thermal conductance through discrete quantum channels, Physica **E 9**, 60–68 (2001)

4.171 G. Chen, M.S. Dresselhaus, G. Dresselhaus, J.-P. Fleurial, T. Caillat: Recent developments in

thermoelectric materials, Int. Mater. Rev. **48**, 45–66 (2003)

4.172 C. Dames, G. Chen: Theoretical phonon thermal conductivity of Si-Ge superlattice nanowires, J. Appl. Phys. **95**, 682–693 (2004)

4.173 K. Schwab, E. A. Henriksen, J. M. Worlock, M. L. Roukes: Measurement of the quantum of thermal conductance, Nature **404**, 974–977 (2000)

4.174 M. Cardona: *Light Scattering in Solids* (Springer, Berlin Heidelberg 1982)

4.175 P. Y. Yu, M. Cardona: *Fundamentals of Semiconductors* (Springer, Berlin Heidelberg 1995) Chap. 7

4.176 J. C. M. Garnett: Colours in metal glasses, in metallic films, and in metallic solutions, Philos. Trans. Roy. Soc. London A **205**, 237–288 (1906)

4.177 D. E. Aspnes: Optical properties of thin films, Thin Solid Films **89**, 249–262 (1982)

4.178 U. Kreibig, L. Genzel: Optical absorption of small metallic particles, Surf. Sci. **156**, 678–700 (1985)

4.179 M. R. Black, Y.-M. Lin, S. B. Cronin, O. Rabin, M. S. Dresselhaus: Infrared absorption in bismuth nanowires resulting from quantum confinement, Phys. Rev. B **65**, 195417(1–9) (2002)

4.180 M. W. Lee, H. Z. Twu, C.-C. Chen, C. H. Chen: Optical characterization of wurtzite gallium nitride nanowires, Appl. Phys. Lett. **79**, 3693–3695 (2001)

4.181 D. M. Lyons, K. M. Ryan, M. A. Morris, J. D. Holmes: Tailoring the optical properties of silicon nanowire arrays through strain, Nano Lett. **2**, 811–816 (2002)

4.182 M. S. Gudiksen, J. Wang, C. M. Lieber: Size-depent photoluminescence from single indium phosphide nanowires, J. Phys. Chem. B **106**, 4036–4039 (2002)

4.183 J. C. Johnson, H. Yan, R. D. Schaller, L. H. Haber, R. J. Saykally, P. Yang: Single nanowire lasers, J. Phys. Chem. B **105**, 11387–11390 (2001)

4.184 S. Blom, L. Y. Gorelik, M. Jonson, R. I. Shekhter, A. G. Scherbakov, E. N. Bogachek, U. Landman: Magneto-optics of electronic transport in nanowires, Phys. Rev. B **58**, 16305–16314 (1998)

4.185 J. P. Pierce, E. W. Plummer, J. Shen: Ferromagnetism in cobalt-iron alloy nanowire arrays on w(110), Appl. Phys. Lett. **81**, 1890–1892 (2002)

4.186 S. Melle, J. L. Menendez, G. Armelles, D. Navas, M. Vazquez, K. Nielsch, R. B. Wehrsphon, U. Gosele: Magneto-optical properties of nickel nanowire arrays, Appl. Phys. Lett. **83**, 4547–4549 (2003)

4.187 J. C. Johnson, H. Yan, R. D. Schaller, P. B. Petersen, P. Yang, R. J. Saykally: Near-field imaging of nonlinear optical mixing in single zinc oxide nanowires, Nano Lett. **2**, 279–283 (2002)

4.188 M. R. Black, P. L. Hagelstein, S. B. Cronin, Y.-M. Lin, M. S. Dresselhaus: Optical absorption from an indirect transition in bismuth nanowires, Phys. Rev. B **68**, 235417 (2003)

4.189 M. R. Black, Y.-M. Lin, S. B. Cronin, M. S. Dresselhaus: Using optical measurements to improve electronic models of bismuth nanowires. In: *21st Int.*

Conf. Thermoelectrics: Proc. ICT '02, Long Beach, CA, Vol. ISSN 1094-2734, ed. by T. Caillat, J. Snyder (IEEE, Piscataway, NJ 2002) pp. 253–256

4.190 H. Richter, Z. P. Wang, L. Ley: The one phonon Raman-spectrum in microcrystalline silicon, Solid State Commun. **39**, 625–629 (1981)

4.191 I. H. Campbell, P. M. Fauchet: The effects of microcrystal size and shape on the one phonon Raman-spectra of crystalline semiconductors, Solid State Commun. **58**, 739–741 (1986)

4.192 H.-L. Liu, C.-C. Chen, C.-T. Chia, C.-C. Yeh, C.-H. Chen, M.-Y. Yu, S. Keller, S. P. DenBaars: Infrared and Raman-scattering studies in single-crystalline GaN nanowires, Chem. Phys. Lett. **345**, 245–251 (2001)

4.193 R. Gupta, Q. Xiong, C. K. Adu, U. J. Kim, P. C. Eklund: Laser-induced Fano resonance scattering in silicon nanowires, Nano Lett. **3**, 627–631 (2003)

4.194 X. Duan, Y. Huang, Y. Cui, J. Wang, C. M. Lieber: Indium phosphide nanowires as building blocks for nanoscale electronic and optoelectronic devices, Nature **409**, 66–69 (2001)

4.195 Y. Cui, C. M. Lieber: Functional nanoscale electronic devices assembled using silicon nanowire building blocks, Science **291**, 851–853 (2001)

4.196 Y. Cui, X. Duan, J. Hu, C. M. Lieber: Doping and electrical transport in silicon nanowires, J. Phys. Chem. B **104**, 101–104 (2000)

4.197 G. F. Zheng, W. Lu, S. Jin, C. M. Lieber: Synthesis and fabrication of high-performance n-type silicon nanowire transistors, Adv. Mater. **16**, 1890–1891 (2004)

4.198 J. Goldberger, D. J. Sirbuly, M. Law, P. Yang: ZnO nanowire transistors, J. Phys. Chem B **109**, 9–14 (2005)

4.199 D. H. Kang, J. H. Ko, E. Bae, J. Hyun, W. J. Park, B. K. Kim, J. J. Kim, C. J. Lee: Ambient air effects on electrical characteristics of gap nanowire transistors, J. Appl. Phys. **96**, 7574–7577 (2004)

4.200 S.-W. Chung, J.-Y. Yu, J. R. Heath: Silicon nanowire devices, Appl. Phys. Lett. **76**, 2068–2070 (2000)

4.201 C. Li, W. Fan, B. Lei, D. Zhang, S. Han, T. Tang, X. Liu, Z. Liu, S. Asano, M. Meyyappan, J. Han, C. Zhou: Multilevel memory based on molecular devices, Appl. Phys. Lett. **84**, 1949–1951 (2004)

4.202 B. Lei, C. Li, D. Q. Zhang, Q. F. Zhou, K. Shung, C. W. Zhou: Nanowire transistors with ferroelectric gate dielectrics: enhanced performance and memory effects, Appl. Phy. Lett. **84**, 4553–4555 (2004)

4.203 H. T. Ng, J. Han, T. Yamada, P. Nguyen, Y. P. Chen, M. Meyyappan: Single crystal nanowire vertical surround-gate field-effect transistor, Nano Lett. **4**, 1247–1252 (2004)

4.204 M. Ding, H. Kim, A. I. Akinwande: Observation of valence band electron emission from n-type silicon field emitter arrays, Appl. Phys. Lett. **75**, 823–825 (1999)

Part A | 4

4.205 F. C. K. Au, K. W. Wong, Y. H. Tang, Y. F. Zhang, I. Bello, S. T. Lee: Electron field emission from silicon nanowires, Appl. Phys. Lett. **75**, 1700–1702 (1999)

4.206 P. M. Ajayan, O. Z. Zhou: Applications of carbon nanotubes. In: *Carbon Nanotubes: Synthesis, Structure, Properties and Applications*, Vol. 80, ed. by M. S. Dresselhaus, G. Dresselhaus, P. Avouris (Springer, Berlin Heidelberg 2001) pp. 391–425 Springer Ser. Top. Appl. Phys.

4.207 M. Lu, M. K. Li, Z. J. Zhang, H. L. Li: Synthesis of carbon nanotubes/si nanowires core-sheath structure arrays and their field emission properties, Appl. Surf. Sci. **218**, 196–202 (2003)

4.208 L. Vila, P. Vincent, L. Dauginet-DePra, G. Pirio, E. Minoux, L. Gangloff, S. Demoustier-Champagne, N. Sarazin, E. Ferain, R. Legras, L. Piraux, P. Legagneux: Growth and field-emission properties of vertically aligned cobalt nanowire arrays, Nano Lett. **4**, 521–524 (2004)

4.209 G. Dresselhaus, M. S. Dresselhaus, Z. Zhang, X. Sun, J. Ying, G. Chen: Modeling thermoelectric behavior in Bi nano-wires. In: *Seventeenth International Conference on Thermoelectrics: Proceedings, ICT'98; Nagoya, Japan*, ed. by K. Koumoto (IEEE, Piscataway 1998) pp. 43–46

4.210 O. Rabin, Y.-M. Lin, M. S. Dresselhaus: Anomalously high thermoelectric figure of merit in $Bi_{1-x}Sb_x$ nanowires by carrier pocket alignment, Appl. Phys. Lett. **79**, 81–83 (2001)

4.211 L. D. Hicks, M. S. Dresselhaus: The effect of quantum well structures on the thermoelectric figure of merit, Phys. Rev. B **47**, 12727–12731 (1993)

4.212 T. C. Harman, P. J. Taylor, M. P. Walsh, B. E. LaForge: Quantum dot superlattice thermoelectric materials and devices, Science **297**, 2229–2232 (2002)

4.213 X. Duan, Y. Huang, R. Agarwal, C. M. Lieber: Single-nanowire electrically driven lasers, Nature **421**, 241 (2003)

4.214 F. Qian, Y. Li, S. Gradecak, D. L. Wang, C. J. Barrelet, C. M. Lieber: Gallium nitride-based nanowire radial heterostructures for nanophotonics, Nano Lett. **4**, 1975–1979 (2004)

4.215 V. Dneprovskii, E. Zhukov, V. Karavanskii, V. Poborchii, I. Salamatini: Nonlinear optical properties of semiconductor quantum wires, Superlattice. Microst. **23(6)**, 1217–1221 (1998)

4.216 J. C. Johnson, K. P. Knutsen, H. Yan, M. Law, Y. Zhang, P. Yang, R. J. Saykally: Ultrafast carrier dynamics in single ZnO nanowire and nanoribbon lasers, Nano Lett. **4**, 197–204 (2004)

4.217 J. X. Ding, J. A. Zapien, W. W. Chen, Y. Lifshitz, S. T. Lee, X. M. Meng: Lasing in ZnS nanowires grown on anodic aluminum oxide templates, App. Phys. Lett. **85**, 2361 (2004)

4.218 J. C. Johnson, H.-J. Choi, K. P. Knutsen, R. D. Schaller, P. Yang, R. J. Saykally: Single gallium nitride nanowire lasers, Nature Mater. **1**, 106–110 (2002)

4.219 H. J. Choi, J. C. Johnson, R. He, S. K. Lee, F. Kim, P. Pauzauskie, J. Goldberger, R. J. Saykally, P. Yang: Self-organized GaN quantum wire uv lasers, J. Phys. Chem. B **107**, 8721–8725 (2003)

4.220 C. J. Barrelet, A. B. Greytak, C. M. Lieber: Nanowire photonic circuit elements, Nano Lett. **4**, 1981–1985 (2004)

4.221 M. Law, D. J. Sirbuly, J. C. Johnson, J. Goldberger, R. J. Saykally, P. Yang: Ultralong nanoribbon waveguides for sub-wavelength photonics integration, Science **305**, 1269–1273 (2004)

4.222 H. Kind, H. Yan, B. Messer, M. Law, P. Yang: Nanowire ultraviolet photodetectors and optical switches, Adv. Mater. **14**, 158–160 (2002)

4.223 B. M. I. van der Zande, M. R. Böhmer, L. G. J. Fokkink, C. Schöneberger: Colloidal dispersions of gold rods: synthesis and optical properties, Langmuir **16**, 451–458 (2000)

4.224 B. M. I. van der Zande, G. J. M. Koper, H. N. W. Lekkerkerker: Alignment of rod-shaped gold particles by electric fields, J. Phys. Chem. B **103**, 5754–5760 (1999)

4.225 W. U. Huynh, J. J. Dittmer, A. P. Alivisatos: Hybrid nanorod-polymer solar cells, Science **295**, 2425–2427 (2002)

4.226 L. A. Bauer, N. S. Birenbaum, G. J. Meyer: Biological applications of high aspect ratio nanoparticles, J. Mater. Chem. **14**, 517–526 (2004)

4.227 Y. Cui, Q. Wei, H. Park, C. Lieber: Nanowire nanosensors for highly sensitive and selective detection of biological and chemical species, Science **293**, 1289–1292 (2001)

4.228 J. Hahm, C. Lieber: Direct ultra-sensitive electrical detection of DNA and DNA sequence variations using nanowire nanosensors, Nano Lett. **4**, 51–54 (2004)